## Journal of the Magnetics Society of Japan

Electronic Journal URL: https://www.jstage.jst.go.jp/browse/msjmag

## Vol.49 No.6 2025

# **Journal**

### Physics of Magnetism, Utilization of High Magnetic Fields

Synthesis Conditions and Magnetic Properties for Li-Based QS-Type Hexaferrite

T. Yoshijima, H. Mitamura, M. Tokunaga, K. Kakizaki, K. Kamishima ····88

### Thin Films, Fine Particles, Multilayers, Superlattices

Pt Thickness Dependence of Superconductivity in Fe/Pt-Inserted Nb/V/Ta Superconducting Superlattices

F. Tokoro, H. Narita, R. Kawarazaki, R. Iijima, R. Hisatomi, S. Karube, Y. Shiota, and T. Ono ...94

### Measurement Technique, High-frequency Devices, Magnetic Imaging

Noise Reduction and Dynamic Range Enhancement of Pulse-Driven GMI Sensors via Optimized Anti-Aliasing Filtering

S. Idachi, and T. Uchiyama ...97

## **Power Magnetics**

Design and Analysis of Outer-Rotor PM Motor with Segmented Rotor-Shape for Utilizing Reluctance Torque

S. Sakurai, Y. Yoshida, and K. Tajima ···104

Optimization of Magnet Angles for Three-Dimensional Position Control with Three Permanent Magnets

H. Sakuma, S. Sawada, and T. Azuma ···110

## **Biomagnetism / Medical Applications**

Estimating Magnetometer Position and Orientation at Extended Distance from the Calibration Coil Array in a Magnetically Shielded Room

T. Fukui, T. Shibuya, and Y. Adachi …115

### **Erratum**

Erratum: Domain Wall Displacement Modulation GMR Sensors with Closed-Loop Current-Field Feedback [J. Magn. Soc. Jpn., 48, 2, 34-39]

K. Komuro, D. Oshima, T. Kato ···E7







### TPM-2-08s25

HcJの3σ//Ave.0.2% を実現 渦電流補正方法 毛確立済

試料測定磁界

最大試料直径 10 mm

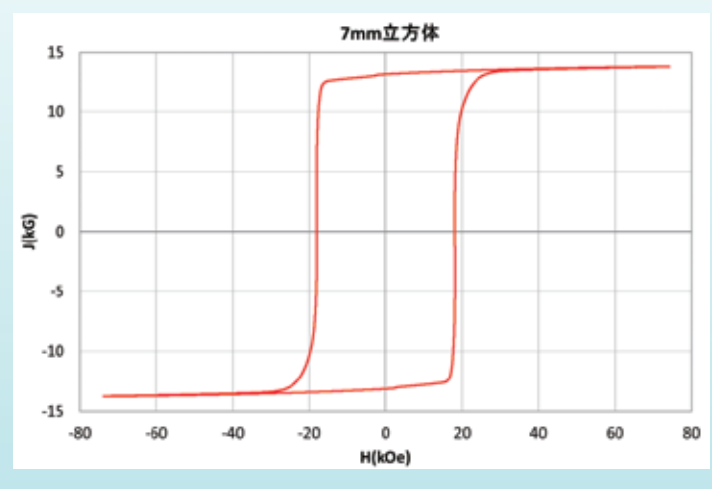
パルス励磁型磁気特性測定装置

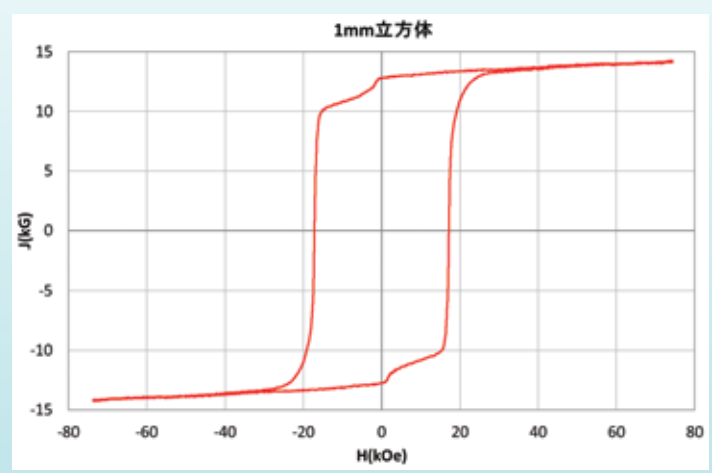
永久磁石および磁性体粉末を固形化した高磁化試料のヒス テリシス曲線の自動測定および描画、SPD (Singuler Point Detection) 測定が可能です。(RT~+200℃)

※1 電気学会資料 MAG-18-088 参照

※2 電気学会資料 MAG-07-011 参照

### NdFeB(sintered) 測定例





1mm 立方体測定用検出コイルはオプション品です

東英工業では他に振動試料型磁力計(VSM)、直流自記磁束計(JIS C2501 準拠)を始め、 各種磁気測定装置を取り揃えております。ぜひお問い合わせ下さい

# Journal of the Magnetics Society of Japan Vol. 49, No. 6

Electronic Journal URL: https://www.jstage.jst.go.jp/browse/msjmag

### **CONTENTS**

Synthesis Conditions and Magnetic Properties for Li-Based QS-Type Hexaferrite	88
Thin Films, Fine Particles, Multilayers, Superlattices Pt Thickness Dependence of Superconductivity in Fe/Pt-Inserted Nb/V/Ta Superconducting Superlattices	
F. Tokoro, H. Narita, R. Kawarazaki, R. Iijima, R. Hisatomi, S. Karube, Y. Shiota, and T. Ono	94
Measurement Technique, High-frequency Devices, Magnetic Imaging  Noise Reduction and Dynamic Range Enhancement of Pulse-Driven GMI Sensors via Optimized  Anti-Aliasing Filtering	97
Power Magnetics  Design and Analysis of Outer-Rotor PM Motor with Segmented Rotor-Shape for Utilizing Reluctance Torque	104
Optimization of Magnet Angles for Three-Dimensional Position Control with Three Permanent Magnets H. Sakuma, S. Sawada, and T. Azuma	110
Biomagnetism / Medical Applications Estimating Magnetometer Position and Orientation at Extended Distance from the Calibration Coil Array in a Magnetically Shielded Room T. Fukui, T. Shibuya, and Y. Adachi	115
Erratum  Erratum: Domain Wall Displacement Modulation GMR Sensors with Closed-Loop Current-Field Feedback [ J. Magn. Soc. Jpn., 48, 2, 34-39 ]  K. Komuro, D. Oshima, T. Kato	E7

### Board of Directors of The Magnetics Society of Japan

President:	T. Ono
Vice Presidents:	C. Mitsumata, H. Saito
Directors, General Affairs:	T. Yamada, Y. Takahash
Directors, Treasurer:	S. Murakami, T. Ochiai
Directors, Planning:	Y. Okada, T. Nagahama
Directors, Editorial:	T. Taniyama, S. Okamot
Directors, Public Relations:	R. Umetsu, M. Kotsugi
Directors, International Affairs:	Y. Nozaki, M.Oogane
Specially Appointed Director, Societies &	& Academic Collaborations:
	A. Saito
Specially Appointed Director, 50th Anniv	versary Project Management:
	M. Mizuguchi
Specially Appointed Director, Contents	Control & Management:
	Y. Kamihara
Auditors:	A. Kikitsu, H. Yuasa

J. Magn. Soc. Jpn., 49, 88-93 (2025)

<Paper>

# Synthesis conditions and magnetic properties for Li-based QS-type hexaferrite

T. Yoshijima, H. Mitamura\*, M. Tokunaga\*, K. Kakizaki, K. Kamishima Graduate School of Science and Engineering, Saitama Univ., 255 Shimo-okubo, Saitama 338-8570, Japan \*Institute for Solid State Physics, Univ. of Tokyo, Kashiwaoha 5-1-5, Kashiwa 277-8581, Japan

Single-phase samples of  $\text{Ba}_2\text{Sn}_{2+x}\text{Li}_{0.5+0.5x}\text{Fe}_{10.5\cdot1.5x}\text{O}_{22}$  were successfully synthesized at sintering temperatures between 1100 and 1250°C within the compositional range of  $-0.2 \le x \le 0.4$ . Substitution of Li<sup>+</sup> and Sn<sup>4+</sup> for Fe<sup>3+</sup> with increasing x led to an expansion of the lattice constants. Higher sintering temperatures promoted the formation of a secondary phase,  $\text{Ba}_{2}\text{Fe}_{4}\text{O}_{11}$ , shifting the single-phase region toward lower x values. Increasing x decreased the Néel temperature, indicating weakened Fe-O-Fe superexchange interactions. Magnetic measurements at 4.2 K showed a saturation magnetization of 16  $\mu_B/f$ .u. at x=0. A ferrimagnetic model, combined with the saturation magnetization, was used to estimate Li<sup>+</sup>-site occupancy. The results suggest that, with increasing x, Li<sup>+</sup> occupancy at tetrahedral sites within the spinel block increases, while occupancy at octahedral sites decreases, maintaining local charge balance with the increased  $\text{Sn}^{4+}$  content at the Q-S block boundary. This redistribution of Li<sup>+</sup> likely plays a key role in determining the material's magnetic properties.

**Keywords:** QS-type hexaferrite, Ba<sub>2</sub>Sn<sub>2+x</sub>Me<sub>1+x</sub>Fe<sub>10-2x</sub>O<sub>22</sub>, phase diagram, pulsed high magnetic fields

#### 1. Introduction

Hexaferrites have garnered significant interest in materials science due to their complex layered structures and diverse magnetic properties  $^{1)\cdot 3)}$ . These iron oxides typically contain alkaline earth metal ions, such as  $\mathrm{Ba^{2+}}$  and  $\mathrm{Sr^{2+}}$ . The crystal structure of hexaferrites consists of the regular stacking of structural blocks, and this arrangement contributes to magnetic anisotropy  $^{4)}$ . Typically, the magnetic moments align along the c-axis of the hexagonal crystal structure, perpendicular to the layers. However, in certain types, such as the Y-type hexaferrite  $\mathrm{Ba_2}Me_2\mathrm{Fe_{12}O_{22}}$  (where Me denotes a divalent metal ion), the magnetic moments align within the hexagonal plane  $^{3)\cdot 4)}$ 

M-type hexaferrites, expressed by AFe<sub>12</sub>O<sub>19</sub> (where A refers to divalent alkaline earth ions, such as Ba<sup>2+</sup> and Sr<sup>2+</sup>) are widely used as hard magnetic materials due to their high coercivity and saturation magnetization <sup>1)</sup>. Conversely, the Y-type hexaferrite displays soft magnetic properties, as the magnetic moments are free to rotate within the hexagonal plane, making them suitable for high-frequency RF applications <sup>5)-9)</sup>.

Among hexaferrites with a layered structure similar to the Y-type, the QS-type hexaferrite, represented by Ba<sub>2</sub>Sn<sub>2</sub>MeFe<sub>10</sub>O<sub>22</sub>, has been well-established <sup>10)-13)</sup>. This material has a magnetic structure characterized by a c-axis that is twice the length of the crystallographic c-axis, with spins aligned in an antiparallel configuration, resulting in antiferromagnetic behavior <sup>12)</sup>. QS-type hexaferrites exhibit unusual magnetic behavior, with a large magnetization response compared to typical antiferromagnets. Additionally,

Corresponding author: K. Kamishima (e-mail: kamisima@mail.saitama-u.ac.jp).

Harasawa *et al.* proposed a high-field magnetic structure model for this material <sup>14)</sup>.

Previous studies have reported Li+ substitution in various hexaferrites. Partial substitution of Li+0.5Fe3+0.5 for divalent cations has been achieved in W-type and Z-type hexaferrites <sup>15)-16)</sup>. Complete substitution of Li<sup>+</sup>0.5Fe<sup>3+</sup>0.5 for divalent cations has been reported in 18H-type hexaferrites containing Ti<sup>4+</sup> 17). In contrast, full substitution of Li+0.5Fe3+0.5 in Y-type hexaferrites has not been successful 18). In QS-type hexaferrites, Ba<sub>2</sub>Sn<sub>2</sub>MeFe<sub>10</sub>O<sub>22</sub>, which have a structure similar to Y-type hexaferrites, the presence of tetravalent Sn<sup>4+</sup> may compensate for the charge imbalance introduced by monovalent Li<sup>+</sup>, potentially enabling synthesis with the nominal composition  $Me^{2+} = \text{Li}_{0.5}^{+}\text{Fe}^{3+}_{0.5}$ . In addition, our investigation implemented a composite substitution in which trivalent  $Fe^{3+}$  ions were replaced by a mixture of monovalent Li+ and tetravalent Sn4+ ions, represented by the pseudo-trivalent species Li<sup>+</sup>1/3Sn<sup>4+</sup>2/3. Such a substitution, where a trivalent ion is substituted by a tetravalent-low-valent ion pair, is a possible approach in hexaferrite chemistry for modulating magnetic anisotropy; magnetic properties of M-type hexaferrite can be tuned by substituting Fe3+ with divalent-tetravalent ion pairs (e.g., Co<sup>2+</sup>-Ti<sup>2+</sup>, Zn<sup>2+</sup>-Ti<sup>4+</sup>,  $Mn^{2+}$ - $Ti^{4+}$ )  $^{19-25)}$ , sometimes even converting it from a hard to a soft magnet. They may also increase spontaneous magnetization by introducing non-magnetic ions into minority-spin sublattices. Accordingly, this work applied Li+ substitution to not only demonstrate its feasibility but also to investigate emergent magnetic characteristics hexaferrites. Based on these findings, this study explores whether Li+ substitution can be successfully applied to QS-type hexaferrites, aiming to uncover potential new material properties.

#### 2. Experimental procedure

Samples were synthesized via a solid-state reaction route with BaCO<sub>3</sub>, SnO<sub>2</sub>, Li<sub>2</sub>CO<sub>3</sub>, and α-Fe<sub>2</sub>O<sub>3</sub> starting materials. The powders were mixed at a molar ratio of Ba: Sn: Li: Fe = 2: 2 + x: 0.5 + 0.5x: 10.5 - 1.5x. The compositional parameter x was chosen to be in the range of  $-0.8 \le x \le 1.0$ , which corresponds to the region where the single-phase of QS-type hexaferrite is expected to form based on our preliminary experiments. The powders were mixed in a polyethylene pot with ethanol and zirconia beads, which was rotated by a ball milling apparatus (AZ-ONE, ANZ-61S) for 24 hours. The resulting powder was dried, pressed into disks at 1 t/cm<sup>2</sup>, and heated at 1000, 1100, 1150, 1200, 1250, and 1300°C for 5 hours. After sintering, the disk surface was ground with a polishing stone to remove the Li-deficient layer caused by the vaporization of Li oxide.

Powder X-ray diffraction experiments were conducted at room temperature with Cu-Ka radiation with a diffractometer (Bruker D8 ADVANCE ECO). Magnetization was measured up to 15 kOe with a vibrating sample magnetometer (Tamakawa TM-VSM2130HGC), up to 70 kOe with a SQUID magnetometer (Quantum Design, MPMS-XL), and up to 600 kOe generated by a pulsed magnet with a duration of 36 ms in ISSP by the use of an induction method.

#### 3. Result and discussion

Figure 1 shows the X-ray diffraction (XRD) patterns of  $Ba_2Sn_{2+x}Li_{0.5+0.5x}Fe_{10.5\cdot1.5x}O_{22}$  (-0.8  $\leq x \leq$  1.0) samples sintered at 1200°C. A single-phase structure was obtained in the range -0.1  $\leq x \leq$  0.4. For  $x \geq$  0.5, the

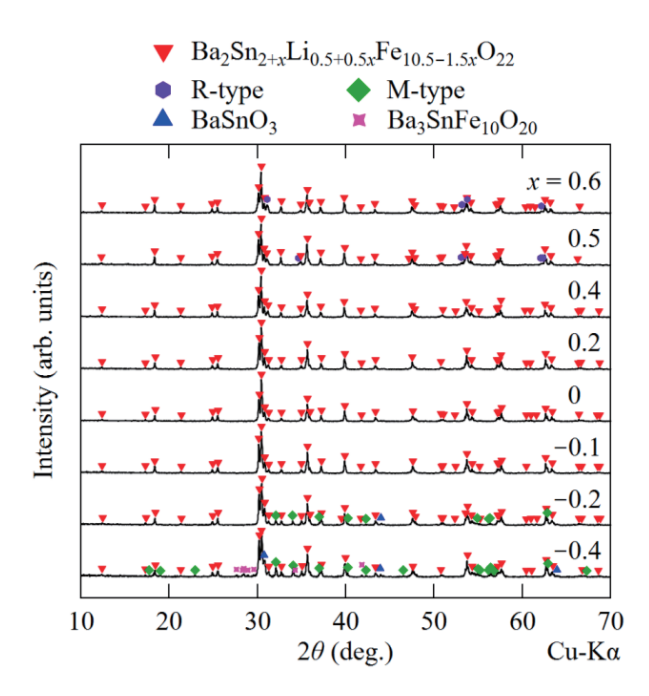
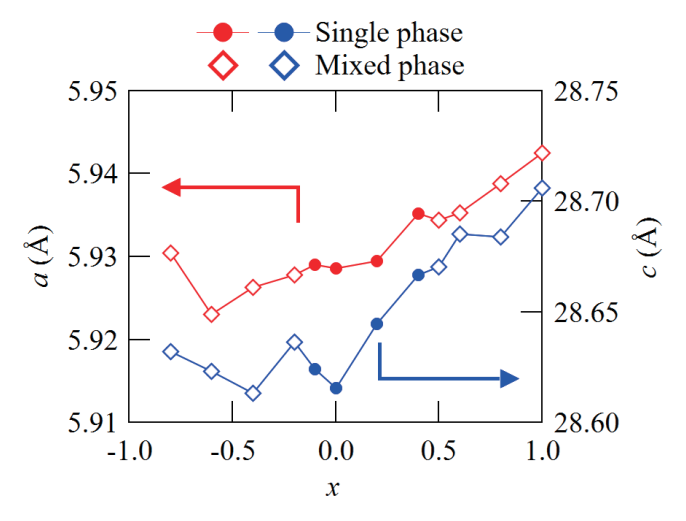


**Fig. 1** X-ray diffraction patterns of Ba<sub>2</sub>Sn<sub>2+x</sub>Li<sub>0.5+0.5x</sub>Fe<sub>10.5-1.5x</sub>O<sub>22</sub> series (-0.4  $\leq x \leq$  0.6) sintered at 1200°C.

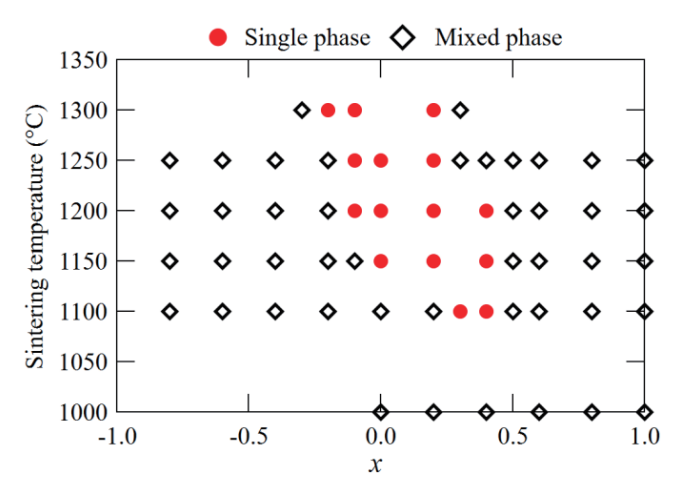
R-type phase appeared as a secondary phase. The R-type secondary phase can undergo substitutions, which may be a factor in suppressing the formation of other secondary phases. For  $x \le -0.2$ , M-type and BaSnO<sub>3</sub> phases were detected, with an additional Ba<sub>3</sub>SnFe<sub>10</sub>O<sub>20</sub> phase forming at  $x \le -0.4$ .

Figure 2 illustrates the x-dependence of the lattice constants for  $Ba_2Sn_{2+x}Li_{0.5+0.5x}Fe_{10.5\cdot1.5x}O_{22}$  samples sintered at  $1200^{\circ}C$ . Open markers represent samples containing secondary phases. In the range  $x \geq \cdot 0.1$ , the lattice constants increased with increasing x, which is attributed to  $Fe^{3+} \rightarrow (Li^+_{1/3}Sn^{4+}_{2/3})$  substitution, as the ionic radii of  $Li^+$  and  $Sn^{4+}$  are larger than that of  $Fe^{3+}$ . In contrast, for  $x \leq \cdot 0.1$ , no clear trend in lattice constants was observed, which is likely due to the negligible occurrence of  $(Li^+_{1/3}Sn^{4+}_{2/3}) \rightarrow Fe^{3+}$  substitution in this composition range.

Figure 3 presents the phase diagram of Ba<sub>2</sub>Sn<sub>2+x</sub>Li<sub>0.5+0.5x</sub>Fe<sub>10.5-1.5x</sub>O<sub>22</sub>, which was constructed based on X-ray diffraction analyses of samples sintered



**Fig. 2** x-dependence of lattice constants for  $Ba_2Sn_{2+x}Li_{0.5+0.5x}Fe_{10.5\cdot1.5x}O_{22}$  series (-0.8  $\leq x \leq$  1.0) sintered at 1200°C.



at temperatures ranging from 1000 to 1300°C, with x varying from -0.8 to 1.0. A single-phase region was observed at sintering temperatures of 1100°C or higher, with a compositional range of -0.2  $\leq x \leq$  0.4. As the sintering temperature increased, the single-phase region shifted toward more negative x values. This behavior possibly resulted from  ${\rm Fe^{3+}}{\rightarrow}({\rm Li^+}_{1/3}{\rm Sn^4}^{+}_{2/3})$  substitution in the secondary phase  ${\rm BaSn_2Fe_4O_{11}}$ , leading to additional experiments to investigate this possibility.

Figure 4 shows the X-ray diffraction patterns of  $BaSn_{2+x}Li_{0.5x}Fe_{4\cdot 1.5x}O_{11}$  ( $0 \le x \le 1.0$ ) samples sintered at  $1200^{\circ}C$ , and Fig. 5 presents their x-dependence in lattice constants. In the range of  $0 \le x \le 0.3$ , single-phase samples were obtained, and an increase in

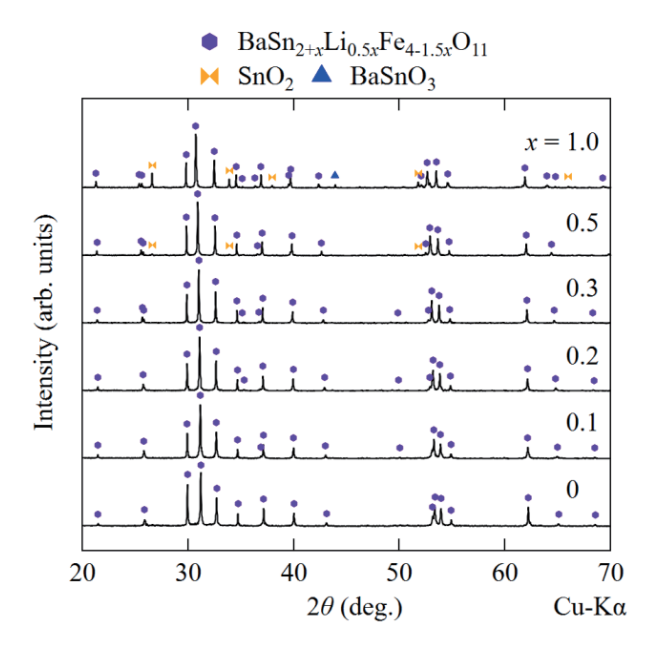


**Fig. 4** X-ray diffraction patterns of BaSn<sub>2+x</sub>Li<sub>0.5x</sub>Fe<sub>4·1.5x</sub>O<sub>11</sub> series  $(0 \le x \le 1.0)$  sintered at 1200°C.

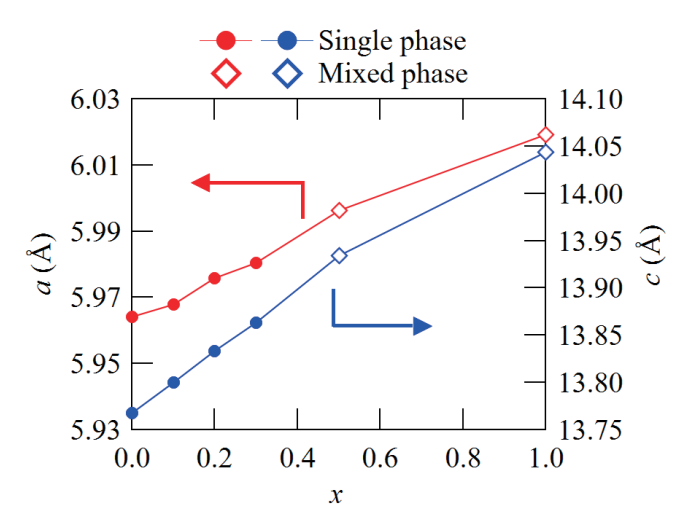


**Fig. 5** *x*-dependence of lattice constants for  $BaSn_{2+x}Li_{0.5x}Fe_{4\cdot 1.5x}O_{11}$  series  $(0 \le x \le 1.0)$  sintered at 1200°C.

lattice constants with increasing x was observed. These results confirm that  $Fe^{3+} \rightarrow (Li^+_{1/3}Sn^{4+}_{2/3})$  substitution occurs in  $BaSn_2Fe_4O_{11}$ . This observation directly explains the shift in the QS-type single-phase region shown in Fig. 3, where higher sintering temperatures facilitate the incorporation of substituted ions into the secondary  $BaSn_2Fe_4O_{11}$ -like R-type phase, thereby expanding the single-phase region to compositions with

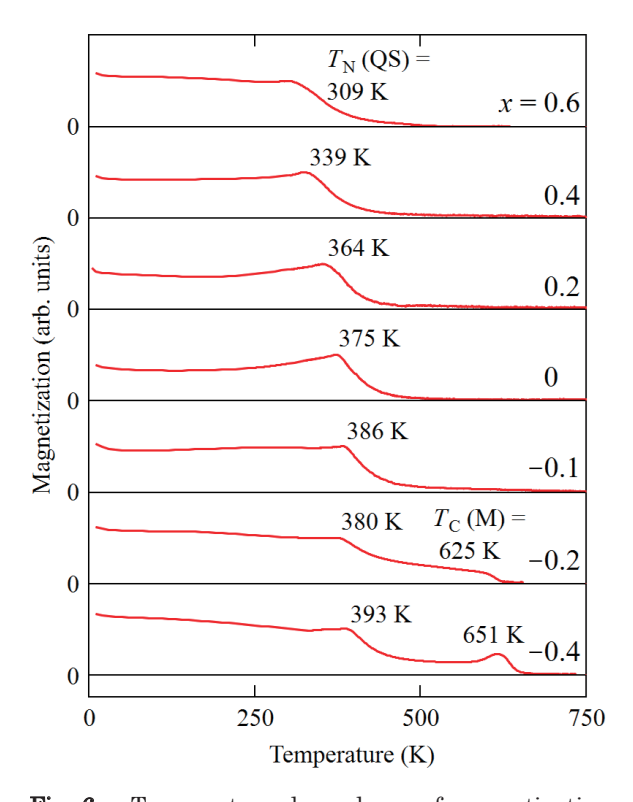


**Fig. 6** Temperature dependence of magnetization of Ba<sub>2</sub>Sn<sub>2+x</sub>Li<sub>0.5+0.5x</sub>Fe<sub>10.5-1.5x</sub>O<sub>22</sub> series (-0.4  $\leq$   $x \leq$  0.6) sintered at  $T_{\rm s} = 1200$ °C, measured under magnetic field of 1 kOe.

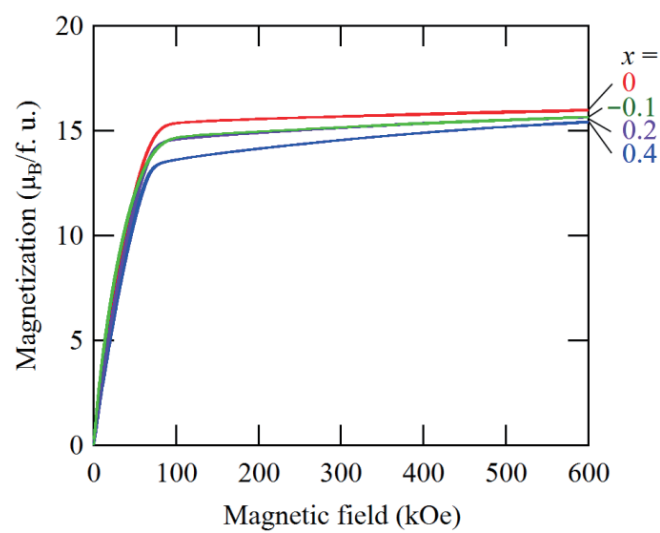


**Fig. 7** Magnetization curves of  $Ba_2Sn_{2+x}Li_{0.5+0.5x}Fe_{10.5+1.5x}O_{22}$  series (-0.1  $\leq x \leq$  0.4) measured at T=4.2 K up to H=600 kOe.

a greater amount of secondary phase. Therefore, this substitution in the secondary phase  $BaSn_2Fe_4O_{11}$  is considered to influence the shift in the single-phase region of  $Ba_2Sn_{2+x}Li_{0.5+0.5x}Fe_{10.5\cdot1.5x}O_{22}$ .

Figure 6 shows the temperature dependence of magnetization for  $\mathrm{Ba_2Sn_{2+x}Li_{0.5+0.5x}Fe_{10.5+1.5x}O_{22}}$  sintered at 1200°C under a magnetic field of H=1 kOe. The cusp-like behavior observed in the temperature dependence of magnetization is a characteristic feature of an antiferromagnetic transition. Since the magnetic field of 1 kOe is within the linear response region of the magnetization curve, the M-T plot essentially reflects

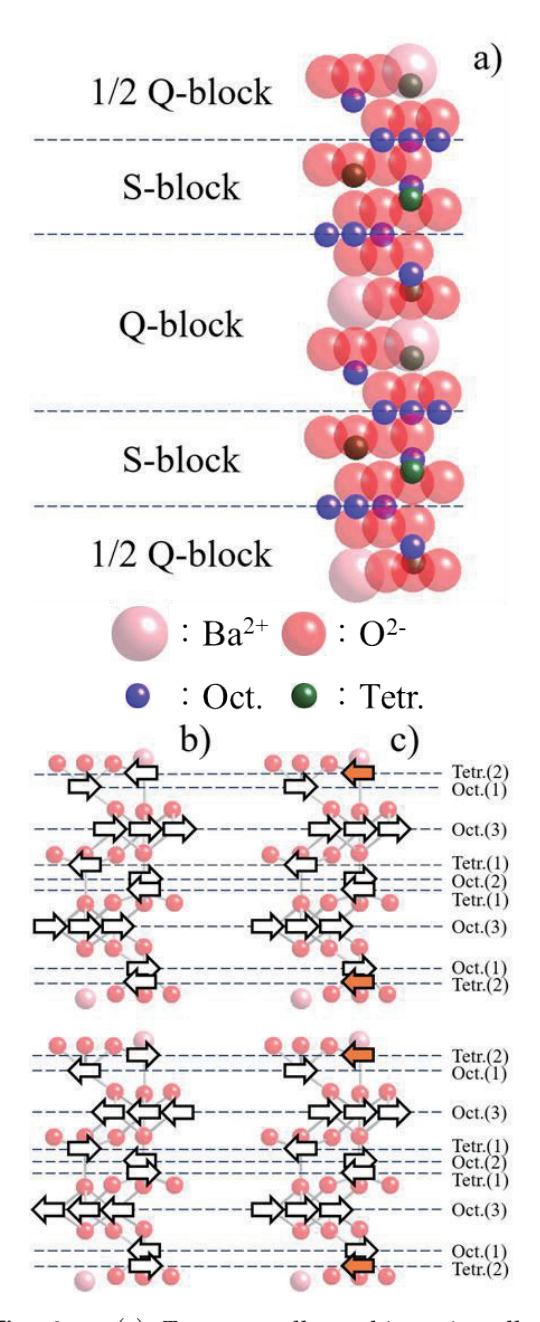


**Fig. 8** (a) Two crystallographic unit cells of Ba<sub>2</sub>Sn<sub>2</sub>MeFe<sub>10</sub>O<sub>22</sub>, (b) low-field antiferromagnetic structure of Ba<sub>2</sub>Sn<sub>2</sub>MeFe<sub>10</sub>O<sub>22</sub> <sup>12)</sup>, (c) high-field ferrimagnetic structure <sup>14)</sup>.

dependence of the the temperature magnetic susceptibility, making it a valid means to determine the Néel temperature. In the range  $x \ge -0.1$ , the Néel temperature of QS-type hexaferrite decreased with increasing x. This behavior is attributed to the weakening of superexchange interactions throughout the crystal due to the Fe<sup>3+</sup> $\rightarrow$ (Li<sup>+</sup><sub>1/3</sub>Sn<sup>4+</sup><sub>2/3</sub>) substitution. In contrast, for  $x \leq -0.2$ , a Curie temperature, likely originating from a secondary phase of M-type hexaferrite, was observed, aligning with the XRD patterns of  $Ba_2Sn_{2+x}Li_{0.5+0.5x}Fe_{10.5\cdot1.5x}O_{22}$  shown in Fig. 1. For the sample with x = -0.4, the magnetization exhibits a slight increase at approximately 620 K. This behavior is identified as the Hopkinson effect, which occurs as a result of the rapid decrease in magnetocrystalline anisotropy near the Curie temperature of the secondary M-type hexaferrite phase. These Curie temperatures are lower than that of a typical M-type BaFe<sub>12</sub>O<sub>19</sub> (725 K) 3). The relatively low Curie temperatures of this M-type hexaferrite appear to result from the partial substitution of Fe ions with Sn and Li, which consequently weakens the superexchange interactions.

Figure 7 shows the magnetization curves of  $Ba_2Sn_{2+x}Li_{0.5+0.5x}Fe_{10.5+1.5x}O_{22}$  measured at T=4.2 K up to H=600 kOe. A magnetization plateau appears above  $H\approx 100$  kOe, with a slope larger than typically expected

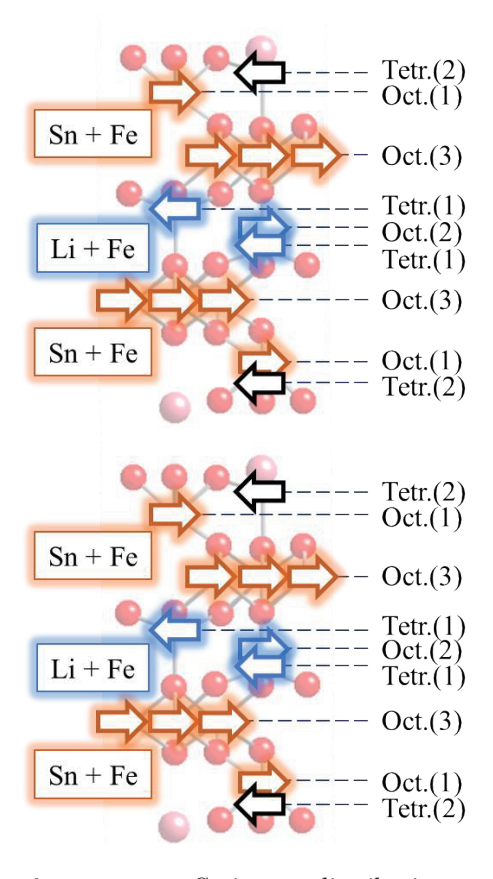


**Fig. 9** Cation distribution in  $Ba_2Sn_{2+x}Li_{0.5+0.5x}Fe_{10.5-1.5x}O_{22}$  under an applied magnetic field of 600 kOe based on charge compensation.

for a simple antiferromagnetic susceptibility. For example, the magnetization of MnO, a typical antiferromagnetic material, reaches 7.9 emu/g at 4.2 K under an applied magnetic field of 100 kOe  $^{26}$ . In contrast, the sample with a composition of x=0 exhibits a magnetization of 59 emu/g under the same conditions, indicating the emergence of a magnetization more than seven times greater. This suggests the presence of a ferrimagnetic spin configuration, in which the spins are likely canted under the applied magnetic field.

To interpret the field dependence of the magnetization, we assume that the spin structure approaches a collinear ferrimagnetic arrangement at high magnetic fields  $^{25)}$ . Accordingly, we treat the magnetization at 600 kOe as an approximate saturation magnetization  $M_{\rm s}$ , as this value provides a practical estimate within the accessible field range, although M continues to increase slightly above 100 kOe. The sample with x=0 exhibited the highest  $M_{\rm s}$  of 16  $\mu_{\rm B}$ /f.u., which increased in the range  $-0.1 \le x \le 0$  and decreased for x>0. This non-monotonic behavior was analyzed by the use of a ferrimagnetic model  $^{14)}$ .

Figure 8 shows (a) the crystal structure of the QS-type hexaferrite, (b) the antiferromagnetic structure proposed by Cadée *et al.* <sup>12)</sup>, and (c) a high-field ferrimagnetic structure <sup>14)</sup>. This material exhibits antiferromagnetic behavior, with the spins at each metal site oriented within the hexagonal plane, as shown in Fig. 8 (b). However, this antiferromagnetic arrangement failed to explain the magnetization plateau observed at high magnetic fields in the Zn-based QS-type hexaferrite <sup>14)</sup>. This plateau was instead explained by Harasawa *et al.* <sup>14)</sup>, who suggested that magnetic moment inversion near barium ions induced a ferrimagnetic configuration. The present study also considers the emergence of this ferrimagnetic state under high magnetic fields, as shown in Fig. 8 (c).

The site occupancy of Fe $^{3+}$  ions in right-pointing and left-pointing positions was determined based on the saturation magnetization  $M_{\rm s}$  by using the following relation:

(Right-pointing Fe<sup>3+</sup> – Left-pointing Fe<sup>3+</sup>) × 5  $\mu$ B = Ms Here, Ref. 12) reported that Sn<sup>4+</sup> ions preferred octahedral sites in the Q block. Ref. 12) and charge compensation requirements also suggest that the Tetr. (2) sites in the QS-type hexaferrite structure are preferentially occupied by Fe3+ ions. Consequently, we assume that our substituted ions (Li+ and Sn4+) primarily occupy other available sites, namely Tetr. (1) and Oct. (2), within the S block. This assumption is further supported by our experimental data; while the saturation magnetization shows a noticeable increase in the range from x = -0.1 to x = 0, the saturation field remains largely unchanged. This suggests that the non-magnetic Li+ ions are not substituting into the Tetr. (2) sites, as such a substitution would likely cause a more significant change in the saturation field. Based on this, we considered that Li+ ions are most likely to

**Table 1** Estimated ionic configuration of Ba<sub>2</sub>Sn<sub>2+x</sub>Li<sub>0.5+0.5x</sub>Fe<sub>10.5-1.5x</sub>O<sub>22</sub> (-0.1  $\leq x \leq$  0.4) sintered at  $T_s$  = 1200°C

X	$M_{ m s}$	Li+@Tetr. (1)	Li+@Oct. (2)
	(μ <sub>B</sub> /f.u.)		
-0.1	15.7	0.245	0.205
0	16	0.35	0.15
0.2	15.7	0.47	0.13
0.4	15.5	0.60	0.1

occupy either the Tetr. (1) or Oct. (2) site. Figure 9 shows the possible magnetic structure of  $Ba_2Sn_{2+x}Li_{0.5+0.5x}Fe_{10.5-1.5x}O_{22}$ , reflecting above-mentioned assumptions about the occupation tendencies of Sn<sup>4+</sup> and Li<sup>+</sup>. The assumptions led to the estimation of the occupancies of Li+ in tetrahedral and octahedral sites. Table 1 summarizes the estimated site occupancies of Li<sup>+</sup>. As x increased, the occupancy of the Tetr. (1) site by Li<sup>+</sup> increased, while that of the Oct. (2) site decreased. This change is attributed to the increased substitution of Sn<sup>4+</sup>, which results in higher occupancy of Sn<sup>4+</sup> at the Oct. (3) site, thus encouraging Li<sup>+</sup> ions to occupy the adjacent Tetr. (1) site to maintain local charge balance. These changes in the site occupancy of Li<sup>+</sup> are likely to influence the x-dependence of magnetization, as shown in Fig. 7.

#### 4. Conclusion

This study clarified the conditions for single-phase formation in the  $Ba_2Sn_{2+x}Me_{1+x}Fe_{10-2x}O_{22}$  ( $Me^{2+}$ Li<sup>+</sup>0.5Fe<sup>3+</sup>0.5) system, in which Fe<sup>3+</sup> is partially substituted by a combination of  $\mathrm{Li}^+{}_{1/3}$  and  $\mathrm{Sn}^{4+}{}_{2/3}.$ Single-phase samples were successfully synthesized within the compositional range of  $-0.2 \le x \le 0.4$  at sintering temperatures of  $T_{\rm s} \geq 1100$  °C. Within this range, the lattice constants exhibited an overall increase with increasing x, with minor deviations observed at compositions close to regions where secondary phases were present. This trend is attributed to the substitution of the smaller Fe<sup>3+</sup> ions by the larger Li<sup>+</sup> and Sn<sup>4+</sup> ions. In addition, the single-phase region was found to shift toward lower x values as the sintering temperature increased, likely due to the enhanced incorporation of Li and Sn into the secondary phase  $BaSn_2Fe_4O_{11}$  at elevated temperatures.

Magnetic measurements revealed a progressive decrease in the Néel temperature with increasing x, suggesting a weakening of superexchange interactions due to the Fe<sup>3+</sup> $\rightarrow$ (Li<sup>+</sup>1/3Sn<sup>4+</sup>2/3) substitution.

The saturation magnetization reached a maximum value of  $16 \mu_B/f$ .u. at x = 0. Analysis of its compositional dependence at 4.2 K suggested that Li<sup>+</sup> occupancy increases at the Tetr. (1) site and decreases at the Oct. (2) site with increasing x.

#### References

- 1) M. Sugimoto: J. Am. Ceram. Soc., 82, 269 (1999).
- 2) U. Ozgur, Y. Alivov, and H. Morkoc: J. Mater. Sci.: Mater. Electron., 20, 789 (2009).
- 3) R. C. Pullar: Prog. Mater. Sci., 57, 1191 (2012).
- C. Delacotte, G. F. S. Whitehead, M. J. Pitcher. C. M. Robertson, P. M. Sharp, M. S. Dyer, J. Alaria, J. B. Claridge, G. R. Darling, D. R. Allan, G. Winter, and M. J. Rosseinsky: *IUCrJ*, 5, 681 (2018).
- Y. Bai, J. Zhou, Z. Gui, Z. Yue, and L. Li: *J. Magn. Magn. Mater.*, **264**, 44 (2003).
- C. A. Stergiou and G. Litsardakis: J. Magn. Magn. Mater., 405, 54 (2016).
- J. -H. You and S. -I. Yoo: J. Magn. Magn. Mater., 471, 255 (2019).
- J. -H You, S. Choi, S. -Y. Park, and S. I. Yoo: J. Magn. Magn. Mater., 491, 165640 (2019).
- K. Zhai, N. Su, J. Sun, J. Cheng, Z. Liu. and Y. Sun: J. Mater. Chem. C, 7, 4173 (2019).
- M. C. Cadée and D. J. W. Ijdo: J. Solid State Chem., 36, 314 (1981).
- M. C. Cadée and D. J. W. Ijdo: J. Solid State Chem., 40, 290 (1981).
- M. C. Cadée, H. J. M. de Groot, L. J. de Jongh and D. J. W. Ijdo: J. Magn. Magn. Mater., 62, 367 (1986).
- F. Sandiumenge, S. Gali, R. Rodriguez-Clemente, X. Batlle, and X. Obradors: J. Solid State Chem., 92, 213 (1991).
- H. Harasawa, H. Mitamura, M. Tokunaga, K. Kakizaki, and K. Kamishima: J. Magn. Soc. Jpn., 48, 88 (2024).

- S. Ram, and J.C. Joubert: J. Magn. Magn. Mater., 99, 133 (1991).
- J. Nakane, K. Kamishima, K. Kakizaki, and N. Hiratsuka:
   J. Jpn. Soc. Powder Powder Metallurgy, 54, 4, 232 (2006).
- 17) H. Takahashi, K. Kakizaki, and K. Kamishima: *The 44th annual conf. Magn. Jpn.*, 15aD-4, 115, (2020).
- 18) K. Kamishima, H. Takahashi, K. Kakizaki, I. Yanase, and T. Fujihara: *J. Cryst. Growth*, **593**, 126755 (2022).
- A. M. Alsmadi, I. Bsoul, S. H. Mahmood, G. Alnawashi and K. Prokes: *J. Appl. Phys.*, **114**, 243910 (2013).
- Y. Guan, Y. Lin, L. Zou, Q. Miao, M. Zeng, Z. Liu, X. Gao and J. Liu: AIP Adv., 3, 122115 (2013).
- J. Li, H. Zhang, Y. Liu, Q. Li, G. Ma and H. Yang: J. Mater. Electron, 26, 1060 (2015).
- Z. Yang, C. S. Wang, X. H. Li and H. X. Zeng: *Mater. Sci. Eng.*, **B90**, 142 (2002).
- 23) S. Sugimoto, K. Okayama, S. Kondo, H. Ota, M. Kimura, Y. Yoshida, H. Nakamura, D. Book, T. Kagotani and M. Homma: *Mater. Trans. JIM*, 39, 1080 (1998).
- 24) Y. S. Hong, C. M. Ho, H. Y. Hsu and C. T. Liu: J. Magn. Magn. Mater., 279, 401-410 (2004).
- K. Kamishima, A. Yonezawa, K. Kakizaki, A. Miyake, H. Mitamura, and M. Tokunaga: *J. Magn. Magn. Mater.*, 538, 168251 (2021).
- D. Bloch, J. L. Feron, R. Georges, I. S. Jacobs: J. Appl. Phys. 38, 1474, (1967).

Received Jul. 09, 2025; Revised Aug. 19, 2025; Accepted Sep. 03, 2025

J. Magn. Soc. Jpn., 49, 94-96 (2025)

<Letter>

# Pt Thickness Dependence of Superconductivity in Fe/Pt-Inserted Nb/V/Ta Superconducting Superlattices

F. Tokoro<sup>1</sup>, H. Narita<sup>1,\*</sup>, R. Kawarazaki<sup>1,\*\*</sup>, R. Iijima<sup>1</sup>, R. Hisatomi<sup>1,2</sup>,

S. Karube<sup>1,2</sup>, Y. Shiota<sup>1,2</sup>, and T. Ono<sup>1,2</sup>

<sup>1</sup>Institute for Chemical Research, Kyoto University, Gokasho, Uji, Kyoto 611-0011, Japan

<sup>2</sup> Center for Spintronics Research Network, Kyoto University, Gokasho, Uji, Kyoto 611-0011, Japan

\*Current address: Department of Materials Physics, Nagoya University, Furo-cho, Chikusa-ku, Nagoya 464-8603, Japan

\*\*Current address: Laboratory for Nanoelectronics and Spintronics, Research Institute of Electrical Communication,

Tohoku University, 2-1-1 Katahira, Aoba-ku, Sendai 980-8577, Japan

The superconducting diode effect (SDE), in which a superconducting current flows in one direction and an ohmic current flows in the opposite direction, is expected to be applied to low-power electronic devices. Among the materials exhibiting a remarkable superconducting diode effect are Nb/V/Ta superconducting superlattices. In particular, Fe/Pt-inserted Nb/V/Ta superlattices exhibit a large zero-field SDE, suggesting that the strong spin-orbit coupling of Pt plays a significant role in its emergence. In this study, we investigated the Pt thickness dependence of superconductivity in Fe/Pt-inserted Nb/V/Ta superlattices. We found that the superconducting transition temperature, critical current density, and non-reciprocal critical current density increased with increasing Pt film thickness and saturated at about 3 nm.

Keywords: superconducting diode effect, inversion symmetry breaking, superlattices, non-reciprocity, exchange-field

#### 1. Introduction

Non-reciprocal charge transport [1] is essential for basic electronic devices such as diodes and transistors. Such transport phenomena have also been observed in polar superconductors [2-4], 2D superconductors [5], and superconducting bilayers and multilayers Recently, the superconducting diode effect (SDE), in which the superconducting current flows in only one direction, was reported in polar Nb/V/Ta superlattices under an external magnetic field [2-4], and theoretical models have been proposed to explain its mechanism [9-Additionally, non-reciprocal responses observed in Josephson junction devices, and the Josephson diode effect (JDE) was demonstrated [13-19]. Both SDEs and JDEs are generic for superconductors under the simultaneous breaking of both time-reversal and space-inversion symmetries. Earlier experiments used an external magnetic field to break time-reversal symmetry. However, recent studies have achieved zerofield SDE and JDE by utilizing the magnetization of ferromagnetic materials. [14, 20, 21].

In particular, Fe/Pt-inserted Nb/V/Ta superlattices show a much larger zero-field superconducting diode effect than Co-inserted ones [20,21]. This result indicates that the strong spin-orbit coupling of Pt plays a significant role in the emergence of this effect.

In this study, we investigated the Pt thickness ( $t_{Pt}$ ) dependence of superconductivity in Fe/Pt-inserted Nb/V/Ta superlattices and found that the superconducting transition temperature, critical current

density, and non-reciprocal critical current density increase with increasing  $t_{\rm Pt}$  and saturate at about 3 nm. This behavior is attributed to the suppression of exchange interactions from the Fe layers within the Pt layers.

#### 2. Experimental results

#### 2.1 Device fabrication

The  $[[Nb(2 \text{ nm})/V(2 \text{ nm})/Ta(2 \text{ nm})]_3/Nb(2 \text{ nm})/V(1 \text{ nm})$  /Pt( $t_{\text{Pt}}$  nm)/Fe(1.2 nm)/Pt(2 nm)/V(1 nm)/Ta(2 nm)]\_{10} was deposited on a MgO (100) substrate by magnetron sputtering, as shown in Figure 1(a). Pt was deposited on four MgO substrates with a thickness gradient by gradually opening shutter during deposition of the films. Subsequently, 3 nm of SiO<sub>2</sub> was deposited as a cap layer. The substrates were heated at 600 °C for 30 min before deposition in a sputtering chamber to remove

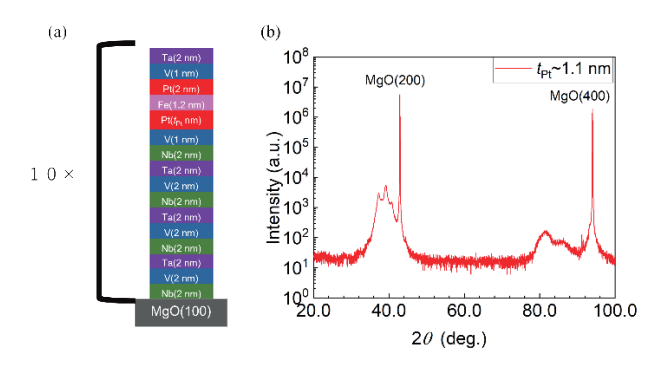


Fig. 1 (a) Schematics of superlattice structure (b) X-ray  $2\theta/\theta$  diffraction measurements at  $t_{\rm Pt} \sim 1.1$  nm.

 $Corresponding \ author: T. Ono \ (e-mail:ono@scl.kyoto-u.ac.jp).$ 

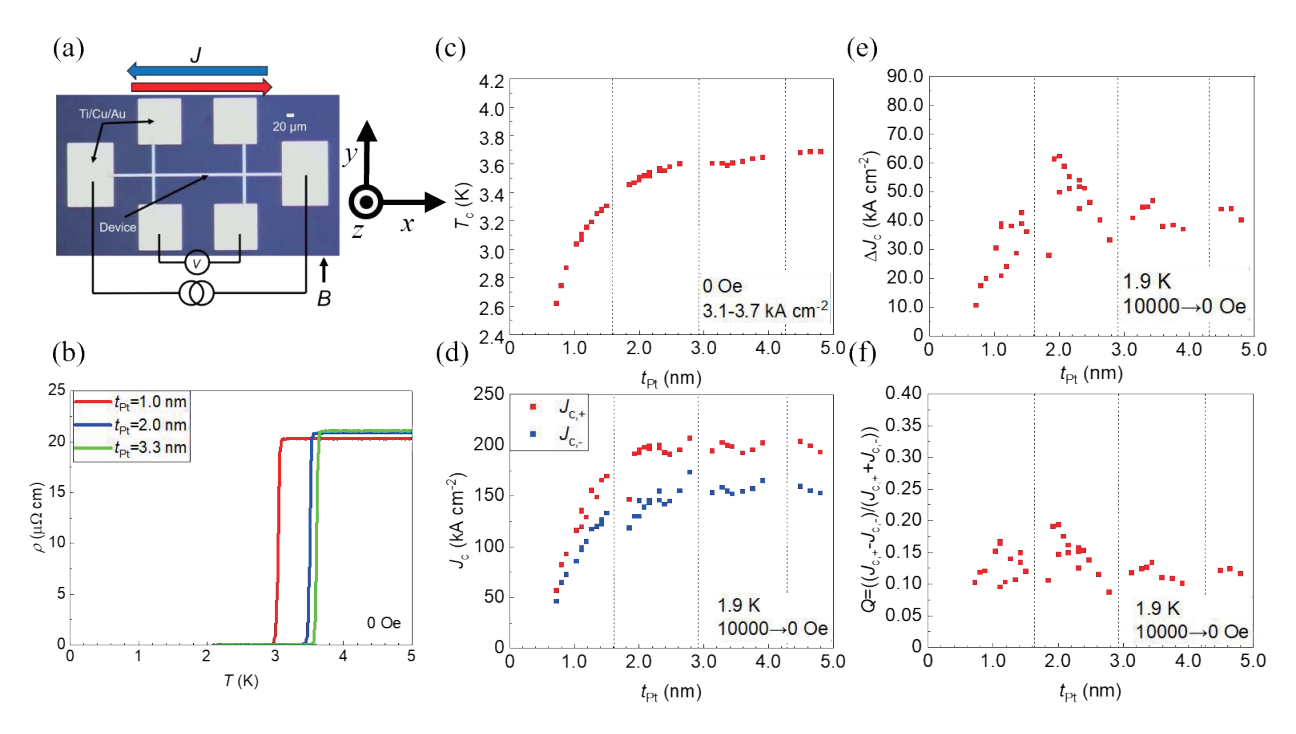


Fig. 2 (a) Schematic of SDE measurement. Polar axis of superlattice is along z-axis and perpendicular to both external magnetic field (B) and electrical current  $(\mathcal{J})$ . (b) Temperature dependence of electrical resistivity  $(\rho)$  at  $t_{\text{Pt}} = 1.0$  nm, 2.0 nm, and 3.3 nm. Temperature was swept from 5 K to 1.9 K. (c)  $T_c$  dependence on  $t_{\text{Pt}}$ .  $T_c$  is defined as temperature at which resistivity drops to half of its value above transition. (d)  $t_{\text{Pt}}$  dependence of  $J_c$  at zero magnetic field, and critical current density in positive  $(J_{c,+})$  and negative  $(J_{c,-})$  directions after magnetic field is changed from 10000 Oe to 0 Oe at 1.9 K. (e)  $t_{\text{Pt}}$  dependence of non-reciprocal component of critical current density  $\Delta J_c$  at zero magnetic field. (f)  $t_{\text{Pt}}$  dependence of Q value  $((J_{c,+} - J_{c,-}))/(J_{c,+} + J_{c,-}))$ .

impurities and then to 300 °C during deposition. Next, devices were fabricated into a Hall bar shape with a width of 10  $\mu m$  by photolithography and argon milling. The  $t_{\rm Pt}$  at the bottom side of Fe on each device varies from 0.7 nm to 5 nm in steps of approximately 0.1 nm. Figure 1(b) shows the results of X-ray  $2\theta l\theta$  diffraction measurements. The multiple broad peaks near MgO (200) and (400) peaks can be attributed to (110) and (220) peaks originating from bcc Nb and Ta. This result is consistent with previous studies [21].

#### 2.2 Electrical Measurement

Figure 2(a) shows schematic of SDE measurement and voltage was measured by four-terminal measurement. Figure 2(b) shows temperature dependence of electrical resistivity  $(\rho)$  for 1.0 nm, 2.0 nm, and 3.3 nm devices.  $\rho$  was measured by applying a current density of 3.1-3.7 kA cm<sup>-2</sup> depending on  $t_{\rm Pt}$  and sweeping temperature downward. In all devices, superconducting transitions were observed at around 3-3.5 K and zero resistivity was achieved.

Figure 2(c) shows  $t_{\text{Pt}}$  dependence of superconducting transition temperature  $T_{\text{c}}$ .  $T_{\text{c}}$  is defined as temperature at which resistivity drops to half of its value above transition. The dashed lines in the figures indicate breaks in four MgO substrates.  $T_{\text{c}}$  increased with

increasing  $t_{Pt}$  and saturated at about 3 nm.

Figure 2(d) shows tet dependence of critical current density (J<sub>c</sub>) at zero magnetic field. Current density is the current divided by total cross-sectional area, including all constituent layers. In Jc measurement polar axis of superlattice is along zaxis and perpendicular to both external magnetic field (B) and electrical current (1). Here, an external magnetic field of 10000 Oe was first applied in  $B \parallel y$  direction to saturate Fe magnetization, and then field was returned to zero. Next, a current was swept from 0 kA cm<sup>-2</sup> along x-axis, which is perpendicular to  $B_{\rm c}$  in positive and negative directions respectively.  $J_{\rm c}$ is defined as the current density at which resistivity increases to half of its value above transition.  $J_c$ increased with increasing  $t_{Pt}$  and saturated at around 3 nm, which is the same trend as  $T_c$ . These  $T_c$  and  $J_c$  results can be caused by the increased stability of superconductor due to the attenuation of exchange interaction from ferromagnetic Fe in the Pt region.

Figure 2 (e) shows  $t_{\text{Pt}}$  dependence of non-reciprocal critical current density ( $\Delta J_c = J_{c,+} - J_{c,-}$ ) at zero magnetic field.  $\Delta J_c$  showed a similar trend to  $J_c$ , saturating at about 3 nm. The continuation of increase in  $\Delta J_c$  until the  $t_{\text{Pt}}$  reaches about 3 nm can be attributed to the increase in  $J_c$ . The sign of  $\Delta J_c$  remains unchanged and did not become zero even in the region where  $J_c$  was saturated. This suggests that exchange interaction at bottom side of

Fe to Cooper pairs is completely suppressed at  $t_{\rm Pt} > 3$  nm. In such regions, exchange interaction through only the upper side Pt is responsible for SDE.

Figure 2 (f) shows  $t_{\text{Pt}}$  dependence of Q value (( $J_{c,+} \cdot J_{c,-}$ )/( $J_{c,+} + J_{c,-}$ )), which indicates efficiency of critical current. Q value remains around 0.1-0.2 regardless of  $t_{\text{Pt}}$ , showing no clear  $t_{\text{Pt}}$  dependence.

#### 3.Conclusion

We found that  $J_c$ ,  $T_c$ , and  $\Delta J_c$  increase in thin  $t_{\rm Pt}$  region and saturate by about 3 nm. This is considered to be due to increased stability of superconductor because of attenuation of exchange interaction from ferromagnetic Fe in the region of Pt.  $\Delta J_c$  remained finite even in the thick  $t_{\rm Pt}$  region, and there was no clear Pt thickness dependence in Q value.

Acknowledgements This work was partly supported by the JSPS KAKENHI grant Numbers JP20H05665, JP21K18145, JP24H00007 JP22H01936, JP24H02233, JP24K00584, JST PRESTO grant Numbers JPMJPR2358, MEXT Initiative to Establish Nextgeneration Novel Integrated Circuits Centers (X-NICS) Grant Number JPJ011438, and Collaborative Research Program of the Institute for Chemical Research, Kyoto University.

#### References

- G. L. J. A. Rikken, J. Fölling, P. Wyder: *Phys. Rev. Lett.*, 87, 236602 (2001).
- F. Ando, Y. Miyasaka, T. Li, J. Ishizuka, T. Arakawa, Y. Shiota, T. Moriyama, Y. Yanase, T. Ono: Nature, 584, 373 (2020)
- 3) Y. Miyasaka, R. Kawarazaki, H. Narita, F. Ando, Y. Ikeda, R. Hisatomi, A. Daido, Y. Shiota, T. Moriyama, Y. Yanase, T. Ono: Appl. Phys. Express., 14, 073003 (2021).
- R. Kawarazaki, H. Narita, Y. Miyasaka, Y. Ikeda, R. Hisatomi, A. Daido, Y. Shiota, T. Moriyama, Y. Yanase, A. V. Ognev, A. S. Samardak, T. Ono: Appl. Phys. Express., 15,

- 113001 (2022).
- R. Wakatsuki, Y. Saito, S. Hoshino, Y. M. Itahashi, T. Ideue, M. Ezawa, Y. Iwasa, N. Nagaosa: Sci. Adv., 3, e1602390 (2017).
- N. Touitou, P. Bernstein, J. F. Hamet, C. Simon, L. Méchin, J. P. Contour, E. Jacquet: Appl. Phys. Lett., 85, 1742 (2004).
- 7) Y. Hou, F. Nichele, H. Chi, A. Lodesani, Y. Wu, M. F. Ritter, D. Z. Haxell, M. Davydova, S. Ilić, O. Glezakou-Elbert, A. Varambally, F. S. Bergeret, A. Kamra, L. Fu, P. A. Lee, J. S. Moodera: *Phys. Rev. Lett.*, **131**, 027001 (2023).
- A. Sundaresh, J. I. Väyrynen, Y. Lyanda-Geller, L. P. Rokhinson: Nat. Commun., 14, 1628 (2023).
- A. Daido, Y. Ikeda, Y. Yanase: Phys. Rev. Lett., 128, 037001 (2022).
- J. J. He, Y. Tanaka, N. A. Nagaosa: New J. Phys., 24, 053014 (2022).
- 11) S. Ilić, F. S. Bergeret: Phys. Rev. Lett., 128, 177001(2022).
- 12) D. Suri, A. Kamra, T. N. G. Meier, M. Kronseder, W. Belzig, C. H. Back, C. Strunk: Appl. Phys. Lett., 121, 102601 (2022).
- 13) H. Wu, Y. Wang, Y. Xu, P. K. Sivakumar, C. Pasco, U. Filippozzi, S. S. Parkin, Y. J. Zeng, T. McQueen, M. N. Ali: Nature, 604, 653 (2022).
- 14) K. R. Jeon, J. K. Kim, J. Yoon, J. C. Jeon, H. Han, A. Cottet, T. Kontos, S. S. Parkin: *Nat. Mater.*, 21, 1008 (2022).
- 15) C. Baumgartner, L. Fuchs, A. Costa, S. Reinhardt, S. Gronin, G. C. Gardner, T. Lindemann, M. J. Manfra, P. E. F. Junior, D. Kochan, J. Fabian, N. Paradiso, C. Strunk: *Nat. Nanotechnol.*, 17, 39 (2022).
- 16) L. Bauriedl, C. Bäuml, L. Fuchs, C. Baumgartner, N. Paulik, J. M. Bauer, K. Q. Lin, J. M. Lupton, T. Taniguchi, K. Watanabe, C. Strunk: Nat. Commun., 13, 4266 (2022).
- M. Davydova, S. Prembabu, and L. Fu: Sci. Adv., 8, eabo0309 (2022)
- 18) T. Golod and V. M. Krasnov: Nat. Commun., 13, 3658 (2022).
- 19) B. Pal, A. Chakraborty, P. K. Sivakumar, M. Davydova, A. K. Gopi, A. K. Pandeya, J. A. Krieger, Y. Zhang, M. Date, S. Ju, N. Yuan, N. B. M. Schröter, L. Fu, and S. S. P. Parkin: Nat. Phys., 18, 1228 (2022).
- 20) H. Narita, J. Ishizuka, R. Kawarazaki, D. Kan, Y. Shiota, T. Moriyama, Y. Shimakawa, A. V. Ognev, A. S. Samardak, Y. Yanase, T. Ono: *Nat. Nanotechnol.*, 17, 823 (2022).
- 21) H. Narita, J. Ishizuka, D. Kan, Y. Shimakawa, Y. Yanase, and T. Ono: Adv. Mater., 35, 2304083 (2023).

Received May 19, 2025; Accepted Aug. 07, 2025

<Paper>

### Noise Reduction and Dynamic Range Enhancement of Pulse-Driven GMI Sensors via Optimized Anti-Aliasing Filtering

S. Idachi, and T. Uchiyama

Department of Electronics, Graduate School of Engineering, Nagoya University, Furo-cho, Chikusa-ku, Nagoya, Aichi 464-8603, Japan

This study proposes a method for enhancing the dynamic range of pulse-driven Giant Magneto-Impedance (GMI) sensors through optimized anti-aliasing filtering. Aliasing noise, identified as the primary limitation, is effectively suppressed using a low-pass filter with a carefully selected cutoff frequency that maintains the sensor's bandwidth. Introducing an anti-aliasing filter with  $f_{\rm C}=31.2$  MHz reduced circuit noise by approximately 58%, yielding a 6 dB improvement in dynamic range. Additional enhancement was achieved by replacing the buffer amplifier with a low-noise ADA4899, which further reduced the 10-Hz noise floor by 58%. Although amplifier noise was mitigated, residual noise from excitation pulses and sampling jitter remained. These results confirm that systematic noise analysis and filter optimization substantially improve GMI sensor performance, supporting their applicability to highly sensitive measurements such as biomagnetic field detection in the picotesla range.

Keywords: GMI sensor, off-diagonal, pulse driven, dynamic range, anti-aliasing filter

#### 1. Introduction

Giant magnetoimpedance (GMI) sensors exhibit magnetic-field sensitivities in the picotesla regime, enabling a wide range of applications such as electronic compasses, current monitoring, and biomagnetic diagnostics<sup>1)</sup>. Their ability to resolve picotesla-level signals has already been exploited for magnetocardiography and magnetoencephalography in prior studies<sup>2)-5)</sup>.

Conversely, while superconducting quantum interference devices (SQUIDs) and optically pumped (OPMs)magnetometers attain femtotesla-scale sensitivity, their intrinsically limited dynamic range and pronounced susceptibility to ambient fields—such as the ~50 μT geomagnetic backgroundnecessitate magnetic shielding, typically in magnetically shielded rooms. A technology capable of high-fidelity biomagnetic sensing without such infrastructure would therefore offer a more straightforward and potentially accurate alternative to electrocardiography (ECG) and electroencephalography (EEG)5).

This work investigates the dynamic-range constraints of picotesla-class GMI sensors and proposes strategies to extend them, thereby eliminating the need for magnetic shielding. We identify aliasing noise introduced by sample-and-hold (S/H) circuitry as the dominant limitation and demonstrate that an optimally engineered anti-aliasing filter (AAF) markedly enhances dynamic range.

Corresponding author: S. Idachi (e-mail: idachi.seiji.f1@s.mail.nagoya-u.ac.jp).

#### 2. Dedicated Sampling Circuit for GMI Sensor

#### 2.1 Off-Diagonal GMI Sensor

When an excitation current is applied to an amorphous alloy wire, the circumferential domain walls and internal magnetization translate and rotate under the azimuthal field generated by the current. Consequently, the circumferential permeability  $\mu_0$  varies with the external magnetic field  $H_{\rm ex}{}^{6}$ . This variation modulates the electromotive force  $V_{\rm C}$  induced in the surrounding pick-up coil, allowing the magnitude of  $H_{\rm ex}$  to be inferred from  $V_{\rm C}$  7. Such a configuration is termed an off-diagonal GMI sensor.

The induced voltage  $V_{\rm C}$  exhibits an off-diagonal dependence on the external field, as depicted in Fig. 11 of [7]. Because  $V_{\rm C}$  is phase-locked to excitation pulses, synchronous sampling at each pulse edge yields the linear transfer characteristic shown in Fig. 12 of [7]. With excitation pulses applied at several-hundred-kilohertz rates, the amorphous-wire GMI element functions as a magnetic sensor that delivers a linear response to external magnetic fields.

# 2.2 Dynamic Range Requirements and Bandwidth Reduction via S/H Circuitry

The amorphous wire used in this study ( $\phi30\mu m$ , Fe<sub>4.35</sub>Co<sub>88.15</sub>Si<sub>12.5</sub>B<sub>15</sub>, manufactured by UNITIKA) exhibits a measurement range of approximately 50  $\mu T$  while maintaining sensitivity to weak magnetic fields on the order of 10 pT. This corresponds to a required dynamic range (DR), calculated as:

DR = 
$$20 \log_{10} \left( \frac{5.0 \times 10^{-5}}{1.0 \times 10^{-11}} \right) \approx 133.98 \text{ dB}$$

The effective number of bits (ENOB) corresponding to this dynamic range is estimated by:

ENOB = 
$$\frac{DR - 1.76}{6.02} = \frac{133.98 - 1.76}{6.02} \approx 21.96 \text{ bit}$$

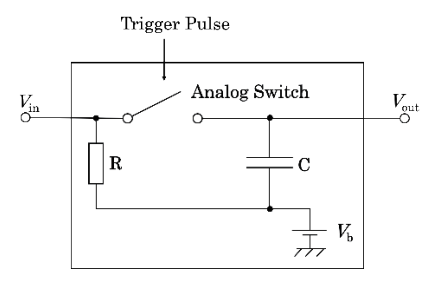


Fig. 1 Configuration of S/H Circuit

Thus, an analog-to-digital converter (ADC) with an ENOB of approximately 22 bits is required to faithfully digitize the sensor output.

However, the coil voltage  $V_{\rm C}$  output by the GMI sensor contains high-frequency components spanning several hundred kilohertz to several megahertz, as illustrated in Fig. 11 of [7]. Currently, no commercially available ADC simultaneously offers both the necessary bandwidth and high resolution to directly capture signals in this frequency range at a practical level.

To overcome this limitation, the present study uses a S/H circuit, illustrated in Fig. 1, which periodically samples the coil voltage  $V_{\rm C}$  by driving an analog switch with a trigger pulse synchronized to the excitation pulse. A bias voltage  $V_{\rm L}$  shifts the input  $V_{\rm In}$  so that it falls within the analog-switch operating range(0- $V_{\rm CC}$ ). This approach effectively reduces the signal bandwidth of the high-frequency  $V_{\rm C}$  component, enabling conversion into a signal format compatible with a high-resolution ADC of an approximately 22-bit class.

#### 3. Magnetic Feedback Method

# 3.1 Dynamic Range Extension through Magnetic Feedback Compensation

The S/H circuit depicted in Fig. 1 utilizes a high-speed negative-channel metal oxide semiconductor (nMOS) analog switch integrated circuit. However, the allowable input voltage range of typical nMOS switches is constrained between 0 V and  $V_{\rm CC}$ , making accurate sampling infeasible when the input signal exceeds this range.

The GMI sensor system used in this study exhibits an open-loop gain of approximately  $2.25\times10^5$  V/T. When operated within the limited voltage range permitted by the nMOS switch, the measurable magnetic field range is restricted to approximately 20  $\mu T$  (0.2 G). As a result, the sensor easily saturates under the influence of the Earth's geomagnetic field.

To address this limitation and expand the sensor's measurable range, it is essential to intentionally suppress the amplitude of the coil output voltage. Magnetic feedback provides an effective means to achieve this goal.

Magnetic feedback involves applying negative feedback to the GMI sensor's output voltage, whereby a current proportional to the output is fed back into the coil to generate a magnetic field that opposes the ambient magnetic field<sup>8)-10)</sup>. This counteracting magnetic field enables the sensor's dynamic range to be effectively

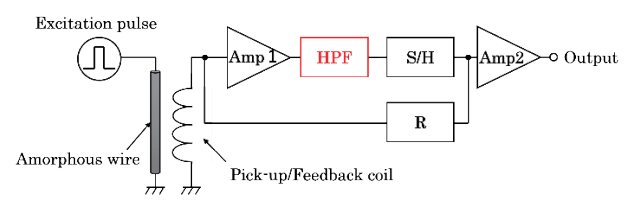


Fig. 2 Block Diagram of GMI Sensor Circuit

extended while ensuring that the coil output remains within the  $0~V-V_{\rm CC}$  operational window.

Theoretically, the degradation in sensitivity due to negative feedback is accompanied by a proportional suppression of noise, thereby allowing the dynamic range to be broadened without compromising the resolution or signal-to-noise ratio (SNR).

#### 3.2 Single Coil Feedback Method

Conventional magnetic feedback schemes typically necessitate an external, dedicated feedback coil to be affixed to the GMI sensor<sup>10)</sup>. In contrast, a single-coil feedback (SCF) approach—wherein the pickup coil simultaneously serves as the feedback coil—has been proposed<sup>11)</sup>.

This method streamlines the sensor head architecture and offers advantages in terms of miniaturization and scalability for mass production. In the SCF configuration, the output voltage  $V_{\rm out}$  of the GMI sensor is directly connected to the pickup coil, enabling the same coil to conduct feedback current and thereby realize magnetic feedback functionality.

To isolate the desired high-frequency electromotive component  $V_{\rm C}$  from undesired low-frequency feedback artifacts originating from  $V_{\rm out}$ , a high-pass filter (HPF) is introduced following the buffer amplifier stage. This configuration suppresses low-frequency currents—which are typically broadened by the limited bandwidth of the S/H circuit—while allowing only the high-frequency signal to propagate.

Through this architecture, the pickup coil fulfills both sensing and compensatory roles, enabling magnetic feedback operation within a remarkably compact and efficient GMI sensor system (Fig. 2).

#### 3.3 Limitations of Negative Feedback

In general, the introduction of negative feedback does not alter the signal-to-noise ratio (SNR), as it uniformly attenuates both the output sensitivity and the noise originating from the sensing element. Specifically, the output voltage under negative feedback is given by

$$V_{\text{out}} = \frac{\alpha}{1 + \alpha\beta} V_{\text{in}} \tag{1}$$

where  $\alpha$  denotes the open-loop gain and  $\beta$  represents the feedback factor. Although the output sensitivity is reduced by a factor of  $1 + \alpha \beta$ , the noise voltage induced by the GMI wire is simultaneously suppressed by the same factor. Accordingly, while the apparent sensitivity decreases as the system transitions from open-loop to closed-loop operation, the resolution—defined by the signal-to-noise ratio of the output voltage—remains

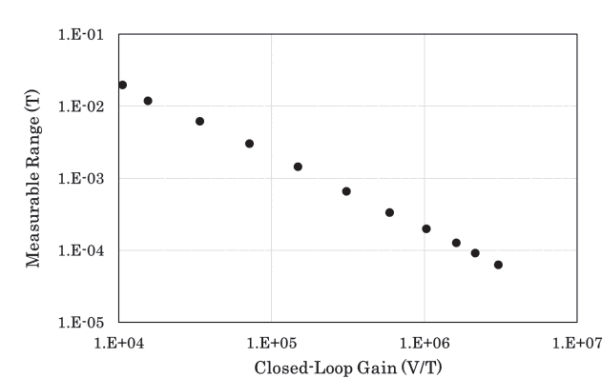


**Fig. 3** Relationship Between Closed-Loop Gain and Measurable Range

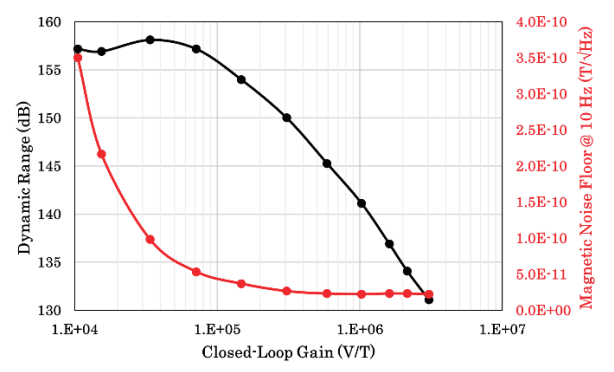


**Fig. 4** Dependence of Loop Gain, Dynamic Range, and Noise Floor at  $10~\mathrm{Hz}$ 

unchanged. Consequently, the resolution remains unchanged while the measurable range is effectively extended, leading to an enhancement in the dynamic range.

In practice, however, this idealized dynamic range enhancement is ultimately constrained by circuit-originated noise. While the noise associated with the wire diminishes in proportion to the reduction of  $V_{\rm C}$  through feedback, residual noise from circuit components—such as amplifiers and resistors—remains unaffected by the feedback loop. As a result, when the feedback strength surpasses a certain threshold, the dominant noise source shifts from the sensor element to the electronic circuitry.

Fig. 3 illustrates the inverse relationship between the closed-loop gain and the sensor's measurable range, confirming that increased feedback (i.e., reduced closed-loop gain) enables broader measurement capability. Fig. 4 presents the dependency of the loop gain, dynamic range, and the 10-Hz noise floor, further elucidating the trade-offs involved.

These findings indicate that to achieve further improvements in dynamic range, it is essential to mitigate the intrinsic circuit noise that remains outside the influence of negative feedback.

#### 4. Noise Analysis

The GMI sensor circuit utilized in this study is shown in Fig. 2. It comprises the following components:

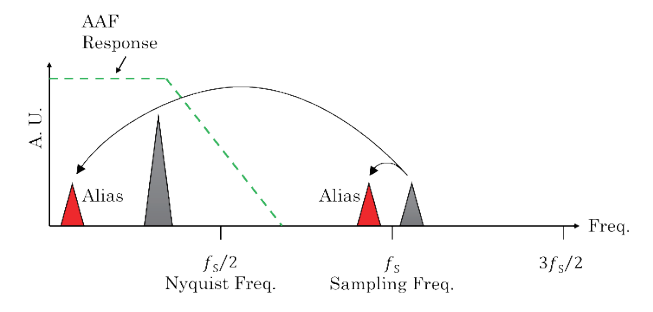


Fig. 5 Aliasing Effect in Frequency Domain Due to Sampling

- 1. Pulse generation circuit
- 2. Pulse shaping circuit
- 3. Unity-Gain buffer amplifier (Amp1)
- 4. High-pass filter (HPF) for single-coil feedback (SCF)
- 5. S/H circuit
- 6. Amplification stage (Amp2)

The cutoff frequency of the HPF was set to 80 kHz to selectively pass only the electromotive force induced by the GMI effect<sup>11)</sup>.

Among the noise sources in the circuit shown in Fig. 2, the dominant contribution is expected to originate from the buffer amplifier (Amp 1), which is placed immediately after the sensor head and therefore largely determines the overall noise performance. In this section, we evaluate the impact of the buffer amplifier's noise on the sensor system.

#### 4.1 Aliasing in Sampling Circuit

In the circuit shown in Fig. 2, an appropriate delay is introduced into the timing pulse to ensure that the S/H circuit captures and retains the peak value of the GMI output waveform. The S/H circuit adopts a configuration analogous to that of a conventional ADC sampling stage and periodically samples the coil voltage at a sampling frequency  $f_{\rm s}$ .

In general, sampling circuits are subject to aliasing, whereby signal components above the Nyquist frequency  $f_{\rm s}/2$  fold back and appear as lower-frequency artifacts (Fig. 5). This aliasing phenomenon causes high-frequency noise to be superimposed onto the baseband spectrum.

The aliasing noise voltage  $V_{\text{alias,rms}}$  is defined using the voltage noise spectral density  $S_n(f)$  as:

$$V_{\text{alias,rms}} = \sqrt{\int_{f_{\text{S}}/2}^{\infty} S_{\text{n}}(f)^2 df}$$
 (2)

#### 4.2 Aliasing Noise from Buffer Amplifier

The dominant noise source entering the S/H circuit is the input-referred noise of the buffer amplifier Amp1 (LT1818). LT1818 exhibits an input voltage noise density of approximately

$$e_{\rm n} = 6 \text{ nV}/\sqrt{\text{Hz}}$$

for frequencies above 3 kHz and has a gain-bandwidth product (GBW) of 200 MHz.

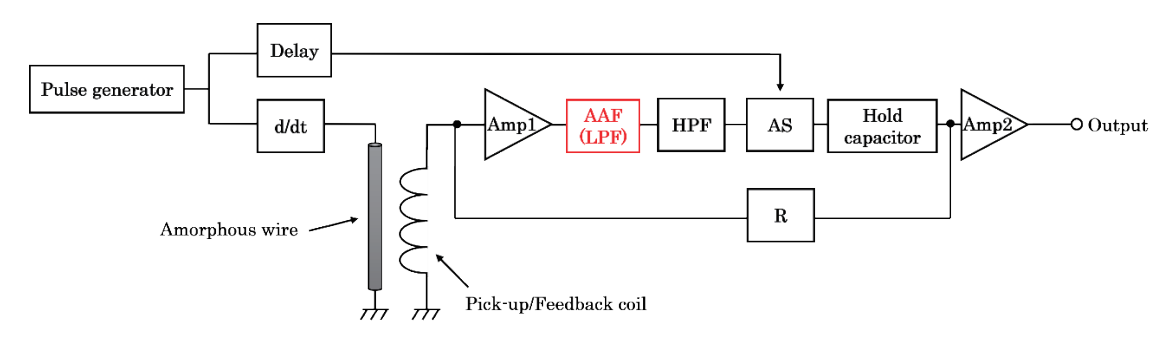


Fig. 6 Insertion of Anti-Aliasing Filter (AAF) in GMI Sensor circuit

Assuming a sampling frequency of  $f_s = 500 \text{ kHz}$ , the total aliasing noise voltage  $V_{alias,rms}$  can be calculated by integrating the white-noise spectrum density from the Nyquist frequency  $(f_s/2 = 250 \text{ kHz})$  up to the amplifier

$$V_{\text{alias,rms}} = \sqrt{\int_{250 \text{ kHz}}^{200 \text{ MHz}} (6 \text{ nV}/\sqrt{\text{Hz}})^2 df} = 84.8 \,\mu\text{V}_{\text{rms}}$$
 (3)

If this noise is assumed to be uniformly aliased into the Nyquist band  $[0, f_s/2]$ , the equivalent post-aliasing noise

density 
$$e_{\rm alias}$$
 is given by:  

$$e_{\rm alias} = \frac{V_{\rm alias,rms}}{\sqrt{f_{\rm s}/2}} = \frac{84.8 \ \mu V_{\rm rms}}{\sqrt{250 \ \rm kHz}} \approx 169.6 \ \rm nV/\sqrt{Hz} \qquad (4)$$

Thus, it is estimated that aliasing noise on the order of 170 nV/ $\sqrt{\text{Hz}}$  is superimposed across the entire frequency range below  $f_s/2$  in the S/H circuit.

#### 5. Anti-Aliasing Filter

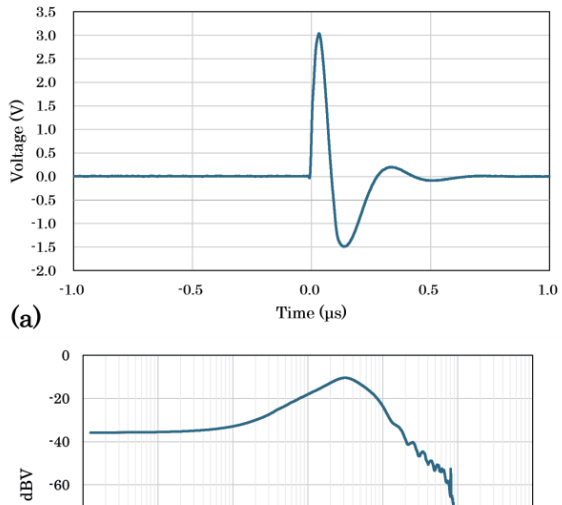
In the preceding section, the impact of buffer amplifier noise was discussed. This section presents a filter configuration designed to mitigate that impact and quantitatively evaluates its effectiveness.

#### 5.1 Aliasing in Sampling Circuit

To suppress aliasing noise introduced by the sampling circuitry of the GMI sensor, a low-pass filter is inserted prior to the S/H stage as an AAF, as illustrated in Fig. 6. Typically, an AAF functions by attenuating signal components above the Nyquist frequency  $(f_s/2)$  to prevent high-frequency noise from folding into the baseband during sampling.

Fig. 7(a) shows the electromotive waveform of the pickup coil (800 turns, 1 cm in length, inner diameter:  $\varphi$ 0.1 mm/outer:  $\varphi$ 0.72 mm, resistance: 6.8  $\Omega$ ), and Fig. 7(b) displays its corresponding FFT spectrum. The signal energy is broadly distributed from 200 kHz to 20 MHz, significantly exceeding the Nyquist frequency of  $f_s/2 =$ 250 kHz for a sampling frequency of  $f_s = 500 \text{ kHz}$ . Therefore, setting the cutoff frequency to  $f_c = f_s/2$ would attenuate a substantial portion of the signal of interest.

As a compromise to preserve the measurement bandwidth while minimizing aliasing, a first-order RC low-pass filter with a cutoff frequency of



-80 -100 -120 1.E+03 Freq. (Hz) (b)

Fig. 7 Electromotive Waveform of Pick-Up Coil, (b) FFT Spectrum of Pick-Up Coil Output

$$f_{\rm c} = 31.2 \, {\rm MHz}$$

was designed and implemented upstream of the highpass filter (HPF), as shown in Fig. 6.

#### 5.2 Effect of AAF on Aliasing Noise

After the insertion of the AAF, the aliasing noise

voltage 
$$V_{\rm alias,rms}$$
 is given by:  

$$V_{\rm alias,rms} = \sqrt{\int_{250~\rm kHz}^{31.2~\rm MHz} (6~\rm nV)^2~df} = 33.4~\mu V_{\rm rms} \qquad (5)$$

The corresponding equivalent noise density  $e_{alias}$  is:

$$e_{\text{alias}} = \frac{V_{\text{alias,rms}}}{\sqrt{250 \text{ kHz}}} = \frac{33.4 \text{ } \mu\text{V}_{\text{rms}}}{\sqrt{250 \text{ kHz}}} \approx 66.8 \text{ } \text{nV}/\sqrt{\text{Hz}}$$
 (6)

Theoretically, this indicates that the aliasing noise is reduced by approximately 60%.

#### 5.3 Effect of AAF on Aliasing Noise

Noise evaluation was conducted using the Ono Sokki FFT CF-2000 Analyzer under the following measurement conditions:

Frequency resolution:  $\Delta f = 0.15625 \text{ Hz}$ 

Window function: Hanning Data length: 16,384 points

Averaging time: 100s

#### 5.4 Results

Fig. 8 presents the circuit noise spectral density before and after the insertion of the AAF. Following AAF implementation, the noise floor at 10 Hz decreased from  $300 \text{ nV/}\sqrt{\text{Hz}}$  to  $120 \text{ nV/}\sqrt{\text{Hz}}$ , corresponding to a reduction of approximately 58%, which is in good agreement with the theoretical attenuation predicted by equations (5) and (6).

Assuming a 46-fold electronic gain-yielding a closedloop sensitivity of approximately  $3\times 10^5\,\text{V/T}$  -the voltage-noise densities correspond magnetic-noise densities of 46 pT/ $\sqrt{\text{Hz}}$  (without the AAF) and 18 pT/ $\sqrt{\rm Hz}$  (with the AAF) at 10 Hz. For comparison, the amorphous wire employed in this study exhibits an intrinsic magnetic noise of 23 pT/ $\sqrt{\text{Hz}}$  at the same frequency. Thus, in the absence of the AAF the circuit noise exceeds the wire noise and degrades the sensor's resolution, whereas with the AAF the circuit contribution falls below the intrinsic level, allowing the resolution to be maintained.

Because the noise floor is lowered without altering the signal transfer, insertion of the AAF permits the closedloop gain to be reduced further-and consequently the measurable range to be expanded—while still keeping the resolution limited primarily by the wire's intrinsic noise.

#### 5.5 Theoretical and Experimental Evaluation of AAF Noise Reduction

The noise reduction effect of the AAF was evaluated by comparing theoretical calculations with experimental measurements. As shown in equation (6), the aliasing noise voltage  $V_{\rm alias,rms}$  depends on the cutoff frequency fc of the AAF, from which the corresponding aliasing noise density  $e_{alias}$  can be derived.

The values of  $e_{alias}$  calculated under the conditions shown in Table 1, along with the experimentally measured circuit noise floor at 10 Hz, are plotted in Fig. 9. The slope of the regression line was found to be 1.06, with a coefficient of determination  $R^2 = 0.98$ , indicating a high degree of correlation.

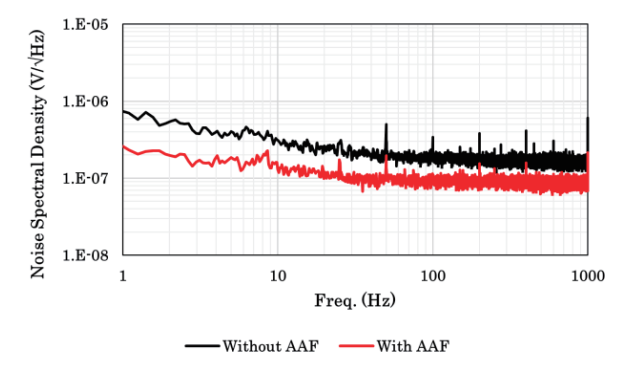


Fig. 8 Noise Spectral Density Without and With AAF

Table 1 RC Constants Corresponding to Frequencies

Cutoff Freq. $f_{\mathbb{C}}$ [MHz]	Resistor $[\Omega]$	Capacitor [pF]
159	10	100
72.3	20	100
31.2	51	100
7.23	220	100

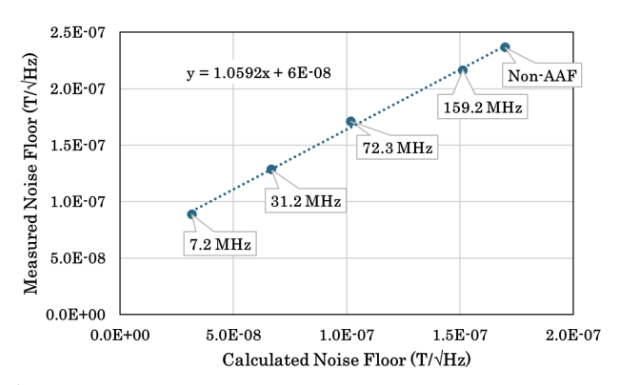


Fig. 9 Correlation Between Calculated and Measured Noise Densities

A slope close to unity confirms a proportional relationship between the aliasing noise density predicted by the theoretical expression in equation (6) and the measured noise floor. In other words, lowering the cutoff frequency results in a corresponding reduction in the noise floor, consistent with theoretical expectations, thereby quantitatively validating the effectiveness of the

These findings confirm that the designed AAF is highly effective in suppressing aliasing noise and enables a predictable reduction in the noise floor of the GMI sensor circuit.

#### 6. Verification of Dynamic Range Enhancement

#### 6.1 Effect of AAF on Loop Gain

Fig. 10 shows the open-loop gain of the system before and after insertion of the AAF. Without the AAF, the open-loop gain was 225,200 V/T. After the insertion of the AAF with a cutoff frequency of  $f_c = 31.2 \text{ MHz}$ , the gain slightly decreased to 204,600 V/T.

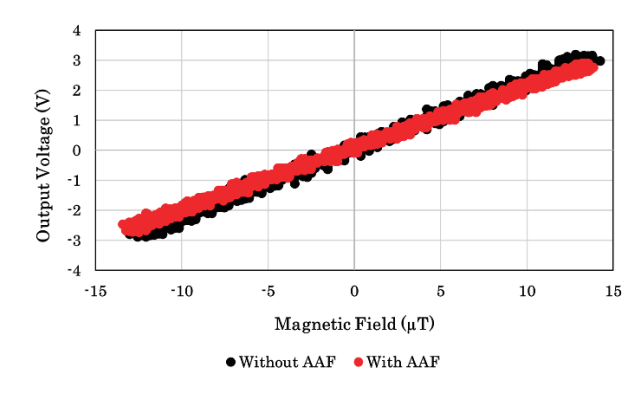


Fig. 10 Open-Loop Gain vs. Measurable Range Before and After AAF Insertion

This reduction is attributed to the attenuation of high-frequency components by the AAF, as illustrated in the FFT spectrum shown in Fig. 7(b).

#### 6.2 Effect of AAF on Noise Floor

Fig. 11 presents the magnetic noise spectral density in an open-loop configuration, both before and after insertion of the AAF. The noise floor around 10 Hz remains nearly identical in both cases, confirming that the signal-to-noise ratio (SNR) is maintained regardless of the presence of the AAF.

The observed differences at 60 Hz and the harmonics are attributed to fluctuations in the measurement environment.

#### 6.2.1 Effect of AAF on Measurable Range

Fig. 12 illustrates the relationship between the closed-loop gain and measurable range. The trend of increasing measurable range with decreasing gain remains consistent before and after AAF insertion, indicating that the AAF does not influence the sensor's measurable range.

# 6.2.2 Dynamic Range Improvement by AAF Implementation

Magnetic noise spectral densities were measured with and without the AAF, and the results are shown in Fig. 13. The plot presents both the spectral noise density at 10 Hz and the dynamic range calculated from the noise

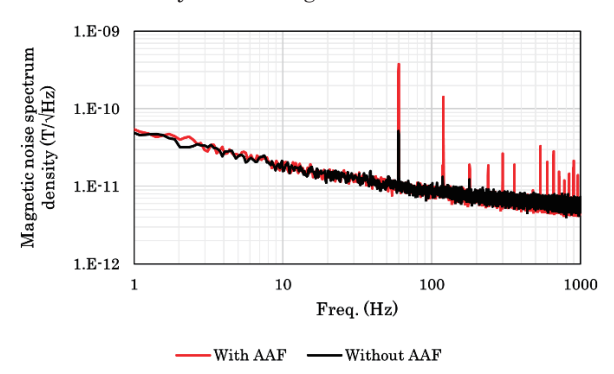
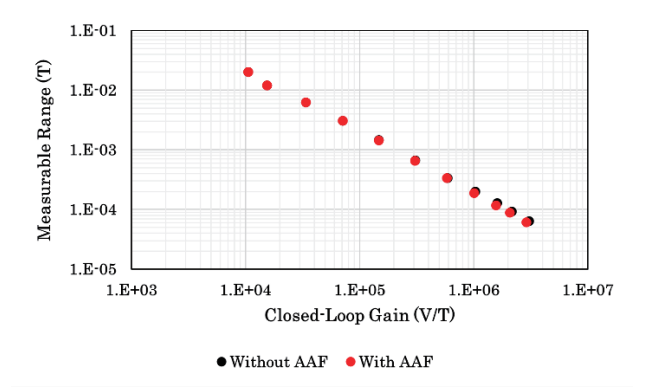


Fig. 11 Magnetic Noise Spectral Density With and Without AAF



**Fig. 12** Closed-Loop Gain vs. Measurable Range Before and After AAF Insertion

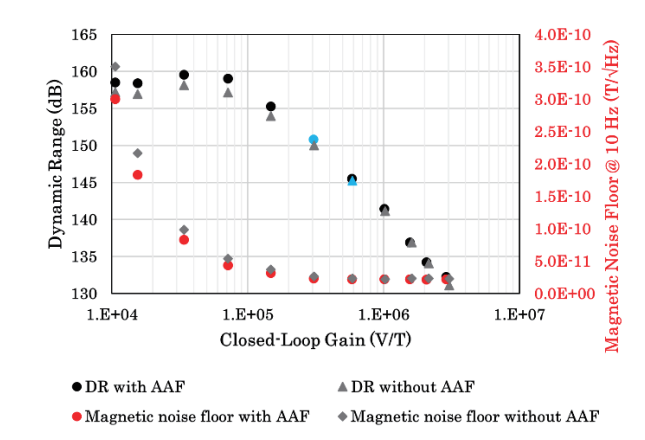


Fig. 13 Effect of AAF on Dynamic Range and Noise Floor at  $10~\mathrm{Hz}$ 

and measurable range values.

As shown in Fig. 13, a difference in dynamic range is observed for closed-loop gains below approximately  $3.0\times10^5$  V/T. This discrepancy arises from the AAF-induced noise reduction by approximately 60%, as confirmed in Section 3.2.2. At equivalent closed-loop gain levels, the dynamic range is reduced by up to 2 dB due to this noise suppression.

Furthermore, in the region where noise degradation does not occur, the dynamic range improved from 145 dB to 151 dB as a result of the AAF implementation. Without the AAF, the threshold for noise degradation—defined by a resolution of 9.1 pT at 10 Hz (corresponding to 23 pT/ $\sqrt{\text{Hz}} \times \sqrt{\Delta f}$ )—was observed at a closed-loop gain of approximately  $5.9 \times 10^5$  V/T, yielding a measurable range of 168 µT. In contrast, with the AAF inserted, this threshold shifted to a closed-loop gain of approximately  $3.1 \times 10^5$  V/T, resulting in an extended measurable range of 326 µT while maintaining the same resolution of 9.1 pT. This shift corresponds to an approximate 6 dB enhancement in dynamic range, attributed to the suppression of aliasing noise by the AAF. As shown in Fig. 13, the blue data points mark these thresholds and corroborate the 6 dB improvement.

#### 7. Further Noise Reduction

#### 7.1 Noise from Buffer Amplifier

As demonstrated in Chapter 6, aliasing noise remains the principal contributor to circuit noise, and the noise suppression effect of the AAF has already reached saturation. Since further lowering the AAF cutoff frequency  $f_{\rm c}$  would degrade the sensitivity and resolution of the GMI sensor, it is necessary to pursue strategies aimed at reducing the input-referred noise itself.

The conventional circuit used an LT1818 buffer amplifier, which offers a wide gain-bandwidth product (GBW  $\approx 400$  MHz) and low input-voltage noise density ( $e_{\rm n}\approx 6$  nV/ $\sqrt{\rm Hz}$  over the 3 kHz–200 MHz range). In this section, we evaluate the effect of replacing it with an ADA4899, a higher-performance amplifier with lower

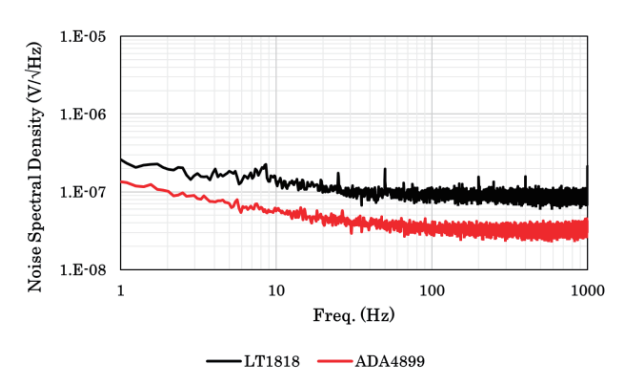


**Fig. 14** Comparison of Magnetic Noise Spectral Density Using LT1818 and ADA4899

input-voltage noise density ( $e_n \approx 1 \text{ nV}/\sqrt{\text{Hz}}$  over the 100 kHz-600 MHz range, GBW  $\approx 600 \text{ MHz}$ ).

Assuming the same AAF configuration as in Fig. 6 with  $f_{\rm c}=31.2$  MHz , the resulting aliasing noise voltage  $V_{\rm alias,rms}$  becomes:

$$V_{\text{alias,rms}} = \sqrt{\int_{250 \text{ kHz}}^{31.2 \text{ MHz}} 1 \text{ nV } df} = 5.56 \,\mu\text{V}_{\text{rms}}$$
 (7)

The corresponding equivalent aliasing noise density is:

$$e_{\text{alias}} = \frac{V_{\text{alias,rms}}}{\sqrt{f_{\text{s}}/2}} = \frac{5.56 \,\mu\text{V}_{\text{rms}}}{\sqrt{250 \,\text{kHz}}} \approx 11.1 \,\text{nV/}\sqrt{\text{Hz}} \qquad (8)$$

Theoretically, this represents a reduction in aliasing noise to approximately one-sixth of its original level. Theoretically, the aliasing noise is reduced by approximately 84%, falling from  $66.8~\text{nV}/\sqrt{\text{Hz}}$  to  $11.1~\text{nV}/\sqrt{\text{Hz}}$ —that is, to roughly one-sixth of its original

level.

Fig. 14 compares the experimentally measured magnetic noise spectral densities for the circuits using LT1818 and ADA4899. At 10 Hz, the noise floor decreased from 130 nV/ $\sqrt{\rm Hz}$  to 55 nV/ $\sqrt{\rm Hz}$ , representing an approximate 58% reduction (nearly one-half). Assuming a 46-fold circuit gain and adjusting the feedback so that the closed-loop sensitivity is  $1.6 \times 10^5 \, \rm V/T$ , the circuit noise corresponds to 37 pT/ $\sqrt{\rm Hz}$  before AAF insertion and 16 pT/ $\sqrt{\rm Hz}$  after the filter. Compared with the LT1818 configuration, this result shows that the minimum resolvable field is preserved even at the lower closed-loop gain, thereby extending the sensor's measurable range.

Although this is less than the theoretically expected 84% reduction, the limited improvement is likely because, after replacing the buffer amplifier with the ADA4899, it was no longer the dominant noise source—thereby allowing other noise contributors in the circuit to become more prominent.

#### 8. Remaining Noise Sources

Even after replacing the buffer amplifier, several potential contributors to the residual noise floor remain:

Ringing induced by excitation pulses in the amorphous wire

- Jitter and ringing associated with the trigger pulse for the S/H circuit
- Inrush current within the S/H circuit

Quantifying the contributions of these factors is expected to facilitate further enhancement of the dynamic range.

#### 9. Conclusion

In this study, the primary noise sources in the GMI sensor circuit were systematically analyzed, revealing that aliasing noise originating from the S/H circuit is the principal factor limiting the dynamic range. By introducing an AAF with a cutoff frequency of  $f_{\rm C}=31.2\,{\rm MHz}$ , designed to suppress aliasing components while preserving the bandwidth of the GMI signal, circuit noise was reduced by approximately 58% without compromising the magnetic noise floor, resulting in a 6 dB improvement in practical dynamic range.

Furthermore, replacing the buffer amplifier from the LT1818 to the low-noise ADA4899 (input-referred noise: 1 nV/ $\sqrt{\rm Hz}$ ) led to an additional noise floor reduction of approximately 58% around 10 Hz, yielding further enhancement in circuit noise performance. However, following the amplifier replacement, the buffer amplifier was no longer the dominant noise source; instead, residual noise components such as ringing from excitation pulses and jitter or ringing in the S/H trigger signals became more pronounced.

Future work will focus on the quantitative evaluation and mitigation of these remaining noise sources. Such optimizations are expected to further extend the dynamic range of the GMI sensor, contributing to its application in highly sensitive biomagnetic measurements, where picotesla-level resolution is required.

#### References

- 1) K. Mohri and Y. Honkura: Sens. Lett., 5, 267 (2007).
- K. Mohri, F. B. Humphrey, L. V. Panina, Y. Honkura, J. Yamasaki and T. Uchiyama: *Phys. Status Solidi a*, 206, 601 (2009).
- 3) J. Ma and T. Uchiyama: *IEEE Trans. Magn.*, **54**, 1 (2018).
- T. Uchiyama and J. Ma: J. Magn. Magn. Mater., 514, 167148 (2020).
- C. Han, M. Xu, J. Tang, Y. Liu and Z. Zhou: Virtual Real. Intell. Hardw., 4, 38 (2022).
- L. V. Panina, H. Katoh, K. Mohri and K. Kawashima: IEEE Trans. Magn., 29, 2524 (1993).
- S. Sandacci, D. Makhnovskiy, L. Panina, K. Mohri and Y. Honkura: *IEEE Trans. Magn.*, 40, 3505 (2004).
- D. Zhang, Z. Pan, H. Zhou and W. Zhang: Sens. Actuators A: Phys., 249, 225 (2016).
- S. Gudoshnikov, N. Usov, A. Nozdrin, M. Ipatov, A. Zhukov and V. Zhukova: *Phys. Status Solidi a*, 211, 980 (2014).
- T. Takiya and T. Uchiyama: *IEEE Trans. Magn.*, **53**, 1 (2017).
- 11) S. Idachi and T. Uchiyama: J. Magn., 29, 253 (2024).

Received May 7, 2025; Revised Jun. 27. 2025; Accepted Jul. 23. 2025

<Paper>

# Design and Analysis of Outer-Rotor PM Motor with Segmented rotor-shape for Utilizing Reluctance Torque

S. Sakurai, Y. Yoshida, and K. Tajima

Akita University, 1-1, Tegata, Gakuten-matchi, Akita, 010-8502, Japan

Recently, the market scale of a drone has grown significantly. To utilize a drone more, the operating time needs to be extended. So, a drone motor should be lightweight and high power. However, the almost drone motor has a Surface permanent magnet, and improving torque is difficult because the outer-rotor has a low-degree design. Increasing torque, the Segment PM is adapted to the drone motor. It can use a reluctance torque with an outer-rotor type. However, the ratio of the reluctance torque is low and it is not enough from a result of the previous paper. So, improvement of the reluctance torque is desired. This paper presents a novel drone motor applied to Segment PM and investigated a ratio of reluctance torque by finite element method (FEM).

Keywords: PM motor, Segment PM, Reluctance torque, Drone

#### 1. Introduction

Recently, drones are expected to be developed for many applications, and it is expected to solve social issues and promote economic development. The Japan drone service market is estimated to expand significantly from 82.8 billion yen in FY2020 to 436 billion yen in FY2025. So, the drone business will grow in the future.

However, an operating time of a typical industrial drone is as short as about 40 minutes. Improving the operating time is strongly desired for convenience. On the other hand, the drone has limited payloads because it loads a luggage and battery. Therefore, a motor should be lightweight and high power.

The drone motor is almost applied to a surface permanent magnet (SPM) motor and outer-rotor type because it has high power and productivity. Further, higher poles and slots are adapted for increasing the torque and low vibration. However, improving the torque of the drone motor is difficult because the rotor iron of outer-rotor is very thin. Therefore, it has lower degree design than the inner-rotor. Further, the drone motor uses a lot of rare earth magnets, and rare earth has resource problems. To improve output, the Halbach array is researched<sup>1)</sup>. It can be improved magnetic flux and motor torque. However, increasing output is limited because a magnet arrangement is also limited.

In order to improve the output in another way, a permanent magnet (PM) motor with segmented rotor-type (Segment PM) is proposed. This structure can utilize a reluctance torque using a small motor size and concentrated windings. Further, Segment PM will suitable for drone motor because it needs high current and low torque ripple by fluctional slot. So, a drone motor will be improved.

This paper presents a novel drone motor adapted to Segment PM and investigated a ratio of reluctance torque by finite element method (FEM).

Corresponding author: S. Sakurai (e-mail: sakurai@gipc.akita-u.ac.jp).

#### 2. Characteristic of Segment PM motor<sup>2)</sup>

Fig. 1 shows a schematic diagram of Segment PM motor. Table 1 indicates the specifications of Segment PM. The rotor and magnet are divided, and it can use a reluctance torque with magnet one because it has saliency.

Fig. 2 indicates the characteristics of the Segment PM. Fig.2 (a) shows the torque characteristics. It indicates that the Segment PM can use the reluctance torque with the magnet torque. Fig.2 (b) denotes the eddy current loss in magnet at 30000 rpm. It is significantly low because the armature flux flows into the rotor iron and does not flow into magnets. From these results, the Segment PM can use the reluctance torque, and it can improve the output by reluctance torque.

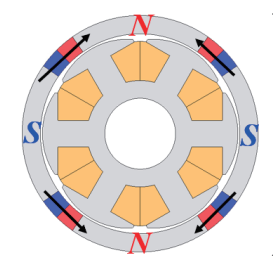
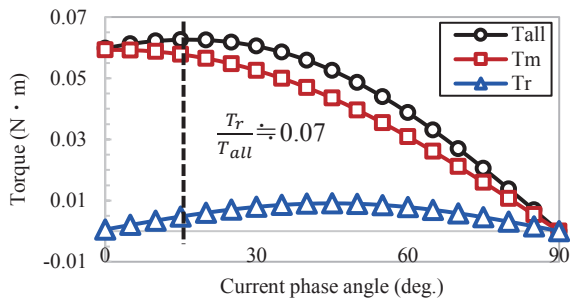


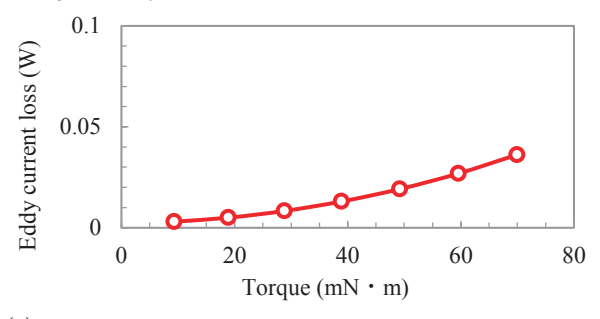
Fig. 1 Schematic diagram of Segment PM motor

**Table 1** Specifications of both PM motor.

Motor diameter	40 mm
Stack length	20 mm
Rated speed	30000 rpm
Rated torque	60 mN⋅m
Target torque ripple	10 % or less
Winding method	Concentrated winding
Material of iron core	0.1 mm silicon sheet
Material of magnet	Sintered Nd-Fe-B



(a) Current phase angle vs. torque characteristics at 6 A/mm<sup>2</sup>.



(b) Torque vs. eddy current loss in magnets at 30000 rpm

Fig. 2 Characteristics of the Segment PM motor

#### 3. Investigation about suitable for drone motors

#### 3.1 Issues in previous research motor.

From the previous paper, Segment PM can used for reluctance torque. However, the ratio of reluctance torque is low. Increasing the reluctance torque, a motor parameter should be improved.

The magnet and reluctance torque can be calculated from (1), (2)

$$T_m = P_n \Psi I_q \tag{1}$$
  

$$T_r = P_n (L_d - L_q) I_d I_q \tag{2}$$

 $T_m$  is the magnet torque, and  $T_r$  is the reluctance torque.  $P_n$  is the magnet pole pears.  $\Psi$  is the magnet flux.  $I_q$  is the q-axis current and,  $I_d$  is the d-axis current.  $L_q$  is the q-axis inductance and,  $L_d$  is the d-axis inductance. From equation (2), a reluctance torque can be improved by the difference between  $L_d$  and  $L_q$  or by increasing  $I_d$  and  $I_q$ . Usually, the difference between  $L_d$  and  $L_q$  can be increased by the design of the flux barrier to the rotor. However, the rotor length of outer-rotor is very thin. If the motor size is 200 mm or more, the flux barrier can be designed on the outer-rotor<sup>3)-5)</sup>. However, it is difficult for a small size outer-rotor motor. The rotor of the Segment PM is also thin. So, the design of the flux barrier is difficult. Therefore, small size outer-rotor motor is focused on the stator shape and current for improvement inductance.

One of the improvements by the stator design, shortening airgap can be increased  $L_d$  and  $L_q$ . Fig. 3 shows the airgap structure of Segment PM. In the previous paper, the unequal gap is used for low torque ripple. On the other hand, the equal gap can be increased magnet torque and reluctance one because the armature

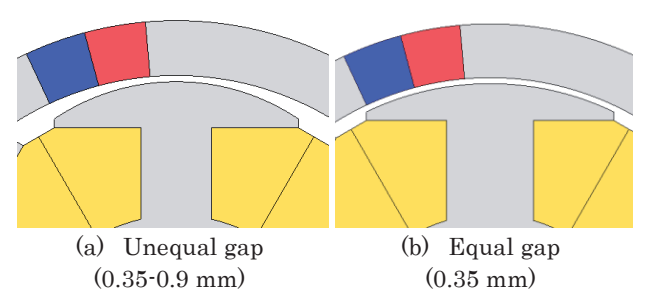


Fig. 3 Construction of air gap

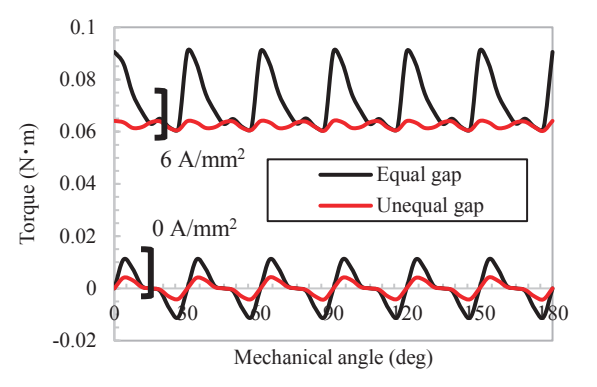


Fig. 4 Comparison of torque waveform

flux can be increased and  $L_{\rm q}$  is also improved. However, the torque ripple is significantly increased. Fig. 4 denotes a comparison of torque waveform. The value of the peakto-peak of the unequal gap is 0.004 N·m and the ripple ratio is about 6.1 %. On the other hand, the one of equal gap is 0.029 N·m and 41.4 %. Therefore, the equal gap will generate bigger noise and vibration. So, a low torque ripple should be required by an equal gap.

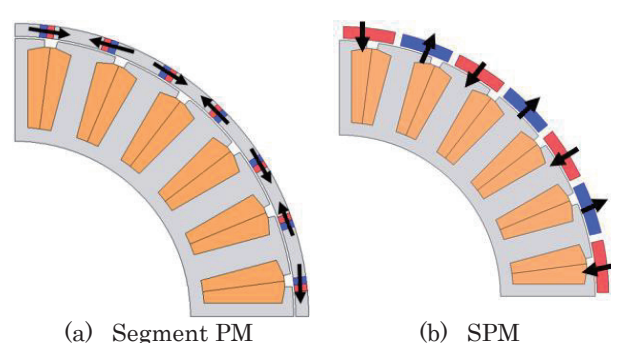
In order to realize it, the Segment PM is applied to a drone motor because it has low torque ripple by a fractional slot.

#### 3.2 Design and Calculation of Segment PM drone motor.

Fig. 5 shows a schematic diagram of the initial design Segment PM drone motor. Table 4 denotes the specifications of the design motors. These motors are designed based on drone motors for pesticide application. The diameter is 84.3 mm. The stack length is 12 mm. The target speed and torque are set to be 2500 rpm and 1.0 N·m, respectively. The number of poles is 28 and the slots is 24. To compare the utilization of a reluctance torque, the motor parameter that  $L_d$ ,  $L_q$ ,  $\Psi_a$  is calculated when the current density is  $7 \, \text{A/mm}^2$ .

Fig. 6 denotes a comparison of inductance. The d and q-axis inductance of SPM is almost the same, but one of Segment PM is different. The saliency rate of Segment PM is about 1.5. From these results, Segment PM will be used reluctance torque.

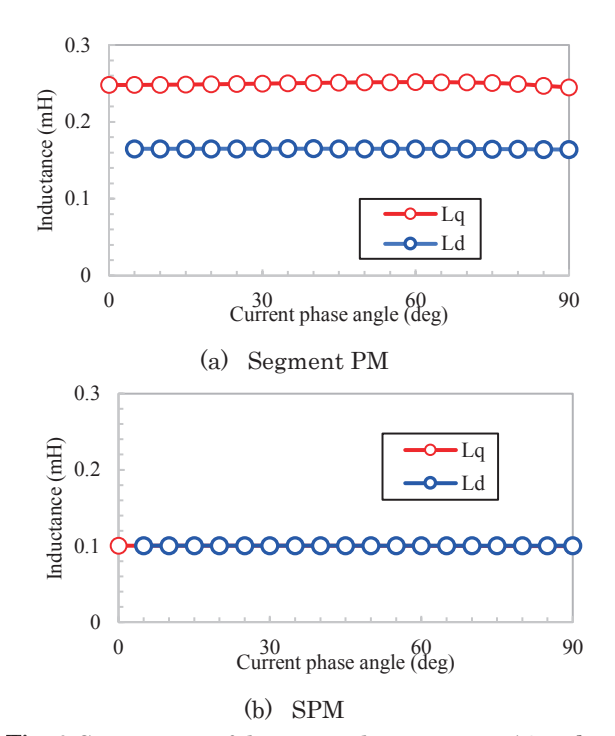
Fig. 7 indicates a comparison of magnet flux. The flux of Segment PM is slightly bigger than SPM. The reason is that the rotor iron is done as backyoke. So, the Segment PM has high magnet flux by low amount of



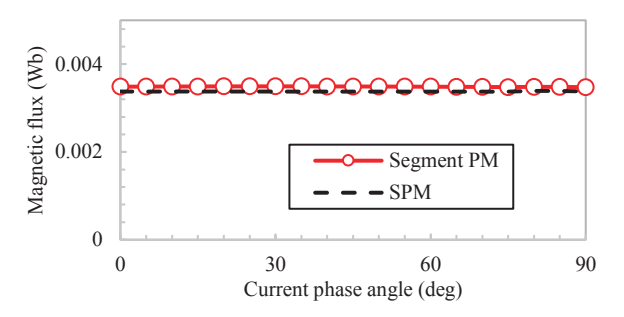
**Fig. 5** Schematic diagram of initial design drone motor. (1/4 model)

Table 2 Specifications of both PM motors.

Table = Specifications of South First Motors.			
Motor diameter	84.3 mm		
Stack length	12 mm		
Rated speed	$2500~\mathrm{rpm}$		
Rated torque	1.0 N·m		
Poles / Slots	28 / 24		
Coil turns	10 turns		
Coil cross section	40 %		
factor	40 %		
Winding method	Concentrated winding		
C	$7~\mathrm{A/mm^2}$		
Current density	$(7.82~\mathrm{A_{rms}})$		
Material of iron core	0.2 mm silicon sheet		
Material of magnet	Sintered Nd-Fe-B		
Amount of moonet	$1277.8\ mm^3$ (Segment PM)		
Amount of magnet	$5004.4~\mathrm{mm^3}$ (SPM)		



**Fig. 6** Comparison of d,q-axis inductance at 7 A/mm<sup>2</sup> (Initial design drone motor)



**Fig. 7** Comparison of magnetic flux. (Initial design drone motor)

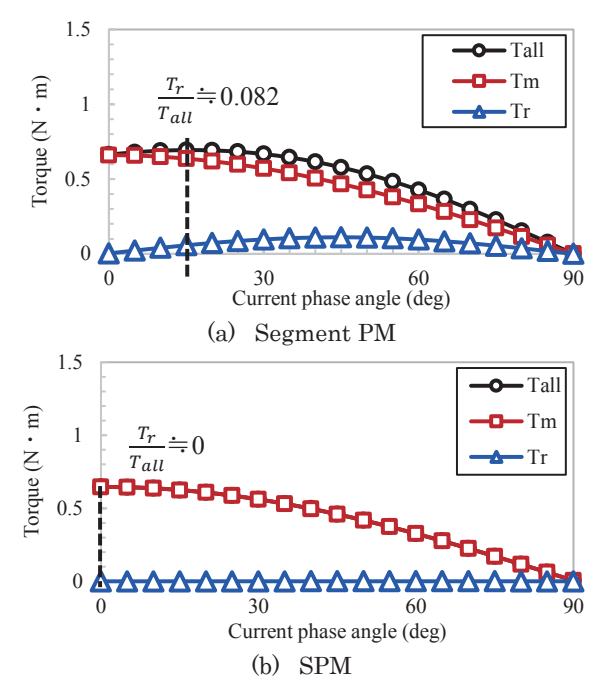


**Fig. 8** Comparison of torque characteristics. (Initial design drone motor)

magnets.

Fig. 8 shows torque characteristics. The max magnet torque of Segment PM is about  $0.66~\rm N\cdot m$ , and one of SPM is  $0.65~\rm N\cdot m$ . The magnet torque is almost the same because the magnet flux is also the same. Further, the max reluctance torque of Segment PM is about  $0.11~\rm N\cdot m$ , and one of the SPM is almost zero. Segment PM has the difference between d and q-axis inductance, so it can use the reluctance torque. Finally, the max total torque of Segment PM is about  $0.69~\rm N\cdot m$  at  $15~\rm deg$ , and one of SPM is about  $0.64~\rm 0.69~\rm N\cdot m$  at  $0~\rm deg$ . From these results, the Segment PM has a higher output than SPM because it has the same magnet flux and larger inductance. However, the ratio of reluctance torque is about  $8.2~\rm \%$ . The reason why it is low is that the armature flux is decreased by many magnets pole.

Fig. 9 shows the comparison of torque waveform. From this waveform, the cogging torque is almost the same. Further, the value of peak-to-peak of the SPM is 0.038 N·m, and one of the Segment PM is 0.050 N·m. The

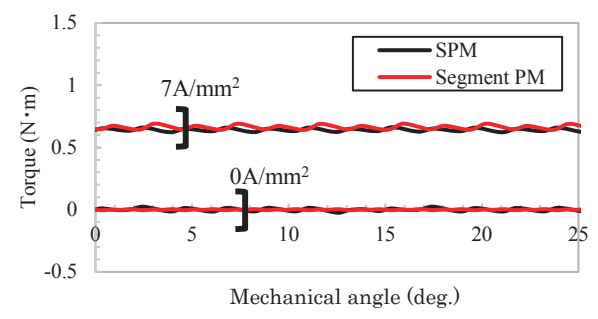


Fig. 9 Comparison of torque waveform (Initial design drone motor)

ripple rate of the SPM is 6.0 %, and one of the Segment PM is 7.5 %.

From these results, the Segment PM has higher torque, and the noise and vibration will be the same because the torque ripple is almost the same. However, the max total torque is not achieved to the rated torque. So, improving torque is required.

#### 4. Improving reluctance torque of Segment PM

#### 4.1 Estimated the current for rated torque

From the above results, the drone motor that adapted Segment PM has higher torque than SPM. However, it is not enough torque. The Segment PM can use reluctance torque, and it has the same magnet torque. Therefore, Segment PM will be obtained by utilizing reluctance torque more. In this chapter, the improvement of torque is done by redesign.

Usually, the outer-rotor motor has low design flexibility because the rotor iron is thin. The rotor iron of Segment PM is also thin. Thus, improvement of  $L_{\rm d}$  and  $L_{\rm q}$  is difficult by design flux barrier. From equations (1) and (2), the magnet torque and the reluctance torque can increase by a bigger current, and it is easy. So, Segment PM is redesigned for high current.

First, each torque is estimated from the motor parameter, and the current is determined. Table 3 shows the estimated max torque. The max  $T_{\rm m}$  and  $T_{\rm r}$  are obtained from calculated  $L_{\rm d}$ ,  $L_{\rm q}$ , and  $\Psi$ . After that,  $T_{\rm all}$  is estimated from max  $T_{\rm m}$  and  $T_{\rm r}$ .  $T_{\rm all}$  can be obtained the rated torque when  $I_{\rm rms}$  is 12.5 to 15.0 A. Therefore, this current value is set to targe current. In order to restrict the current density to  $7{\rm A/mm^2}$ , the stator coil cross-section and coil diameter should be increased.

#### 4.2 Calculation of redesigned Segment PM drone motor

Fig. 10 shows a schematic diagram of the redesigned PM motor. Fig. 11 shows a schematic diagram of motor design parameters, and Table 4 denotes a different design parameter. In order to increase current at 7 A/mm², the coil window cross section is expanded and the motor design parameter is adjusted. The stator inner diameter, backyoke, and pole width are made smaller

Further, the rotor thickness is increased because the production of small magnet is very difficult. The value is determined from the prototyped motor in the previous

Table 3 Estimated each max torque

$I_{ m rms}\left({ m A}_{ m rms} ight)$	$T_{\rm all}\left(\mathbf{N}\cdot\mathbf{m}\right)$	$T_{\rm m}\left(\mathbf{N}\cdot\mathbf{m}\right)$	$T_{\rm r}({ m N}\cdot{ m m})$
5.0	0.35	0.35	0.030
7.5	0.53	0.52	0.067
10.0	0.73	0.69	0.119
12.5	0.93	0.86	0.186
15.0	1.15	1.04	0.268
17.5	1.38	1.21	0.365

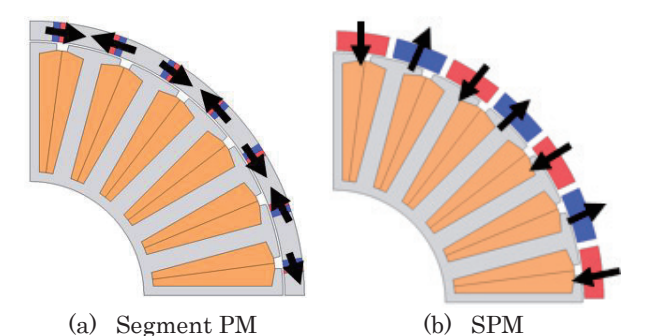


Fig. 10 Schematic diagram of redesigned drone PM motors.(1/4 model)

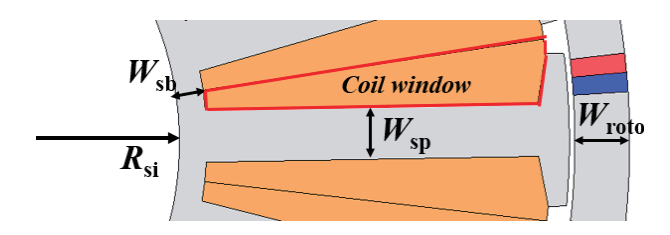


Fig. 11 Schematic diagram of motor design parameter

paper. Therefore, the value of the current RMS is slightly lower than the designed parameter in Table.2. The redesigned Segment PM and SPM are calculated and compared to investigate whether reluctance torque can be utilized.

Fig. 12 indicates the d, q-axis inductance. The inductance of SPM is the same, but the Segment PM one is different. Further, the inductance of Segment PM is lower than before design motor. The reason is that the current is increased but the armature flux is little increased. Fig. 13 shows a comparison of magnetic flux density. This is calculated when magnet is removed. The magnetic flux density of redesign motor is about 1.45 T at stator pole, and before design motor is 0.86T. Therefore, the redesign motor is slightly saturated and inductance is decreased.

Fig. 14 shows the comparison of magnetic flux. The magnetic flux is larger than the above result because the amount of magnet is increased.

Fig. 15 denotes the comparison of torque characteristics. The max total toque of the Segment PM is  $1.29~\rm N\cdot m$  at  $25~\rm deg$ . Further, the magnet one is  $1.1~\rm N\cdot m$ , and the reluctance one is  $0.18~\rm N\cdot m$  at  $25~\rm deg$ . So, the redesigned motor can be achieved target torque. Further, the ratio of reluctance torque is about  $13~\rm \%$ . On the other

Table 4. Different design parameters.

	Before	After
$egin{array}{ll}  ext{Stator} &  ext{inner} \  ext{diameter} \left( R_{ ext{si}}  ight) \end{array}$	25.2 mm	17.5 mm
Stator backyoke width ( $W_{ m sb}$ )	2.0 mm	1.5 mm
Stator pole width $(W_{ m sp})$	3.8 mm	2.8 mm
Rotor thickness ( $W_{ m rotor}$ )	1.85 mm	3.0 mm
Coil window cross section	27.9 mm²/Slot	42.3 mm²/Slot
C	$7\mathrm{A/mm^2}$	$7\mathrm{A/mm^2}$
Current density	$(7.82\mathrm{A_{rms}})$	$(11.8\mathrm{A_{rms}})$
	$1277.8\;\mathrm{mm^3}$	$2043.3~\mathrm{mm^3}$
Amount of	(Segment PM)	(Segment PM)
magnet	$5004.4~\mathrm{mm^3}$	$8002.4~\mathrm{mm^3}$
	(SPM)	(SPM)

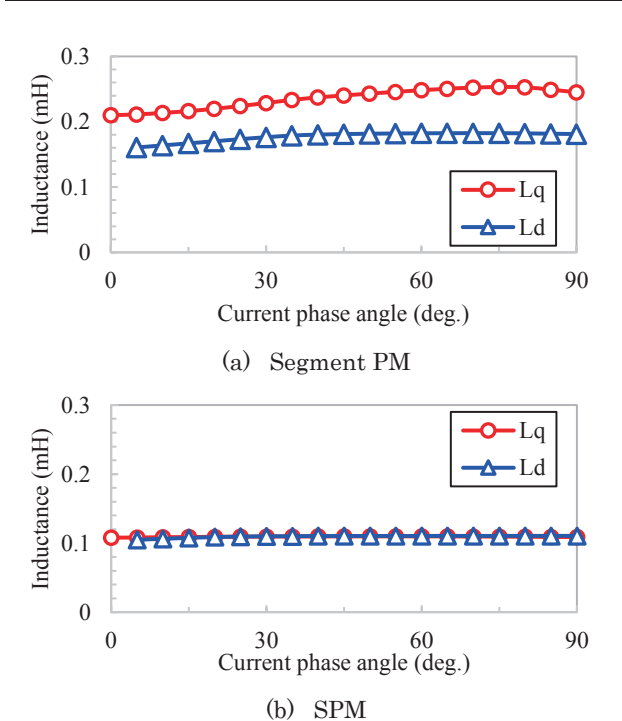
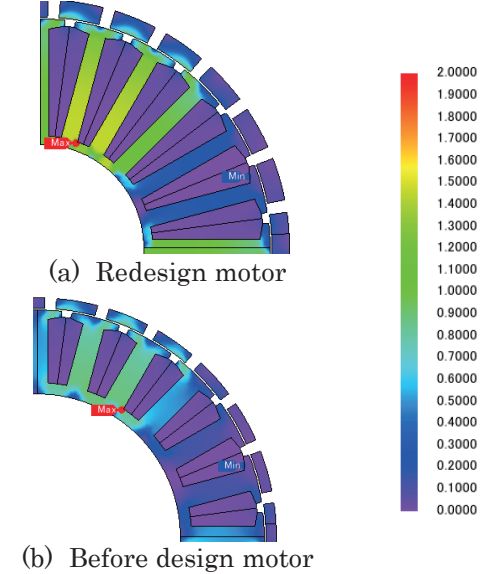


Fig. 12 Comparison of d,q-axis inductance (7 A/mm<sup>2</sup>)

hand, the reluctance torque of SPM is almost zero because the d, q-axis inductance is the same. So, the output torque is mostly magnet torque. The max total torque is about 1.22 N·m. From this result, the reluctance torque can be used effectively by Segment PM. However, the ratio of reluctance torque is not increased as much as expected.



**Fig. 13** Comparison of magnetic flux density that generated by armature flux only.

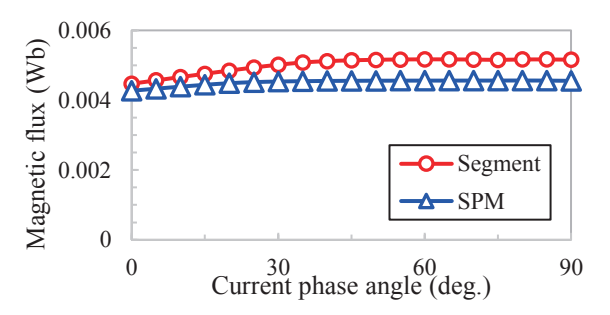
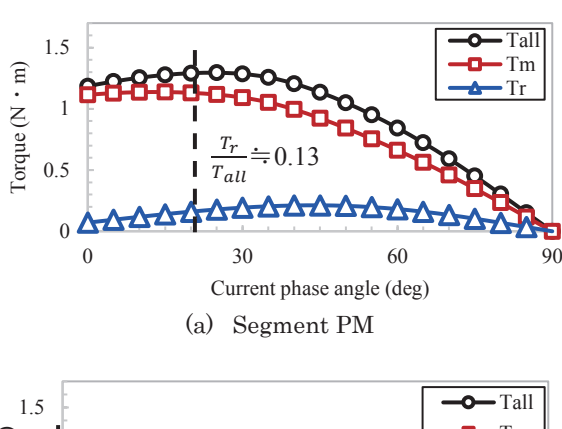


Fig. 14 Comparison of magnetic flux



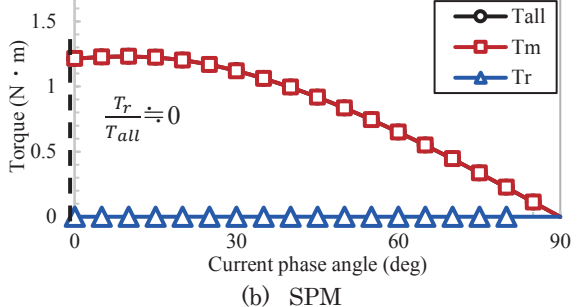


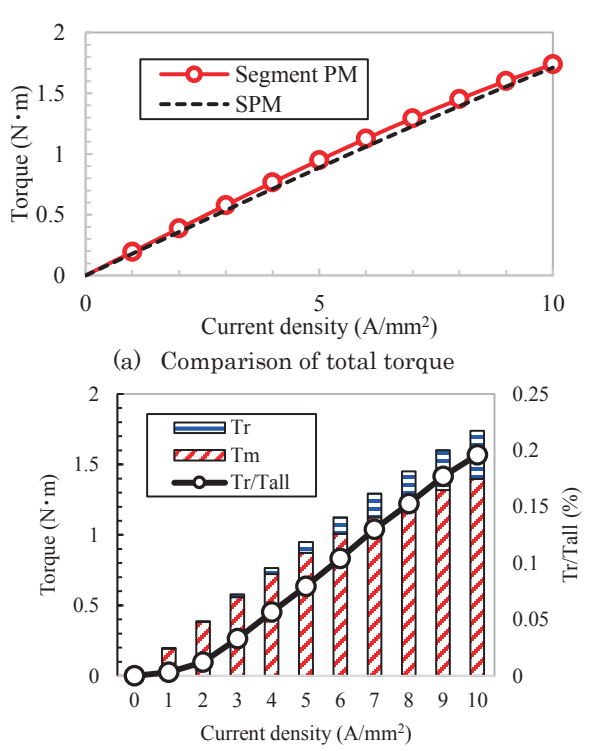
Fig. 15 Comparison of torque characteristics (7 A/mm<sup>2</sup>)

#### 4.3 Comparison of each torque characteristic

The torque characteristics of redesign motor is calculated. Fig. 16(a) shows the current density versus torque characteristics. Segment PM has higher torque because the magnetic flux bigger than SPM and it uses the reluctance torque. Fig. 16(b) indicates the ratio of reluctance torque of the Segment PM. Each torque is plotted when the total torque is max. The ratio of reluctance torque is increased along with the current density. Further, the ratio can be reached about 20% at 10 A/mm<sup>2</sup>.

Fig. 17 denotes the torque waveform. The cogging torque (0 A/mm²) is almost same, but the torque ripple (7 A/mm²) of Segment PM is bigger because the magnetic flux density is increased by bigger current. The value of peak-to-peak of Segment PM is about 0.15 N·m and ripple ratio is 11.7%. Further, the one of SPM is about 0.06 N·m and ripple ratio is 5.14%. The ripple ratio of Segment PM is increased about 2 times, but it is similar to 10 %. Further, a noise that generated by this motor will be low because the motor speed is also low.

From the results, the ratio of reluctance torque can be improved by increasing current. At the 10 A/mm<sup>2</sup>, it can achieve about 20%. However, the inductance is decreased because the stator pole is slightly saturated.



(b) Ratio of reluctance torque (Segment PM)

Fig. 16 Current density versus torque characteristics

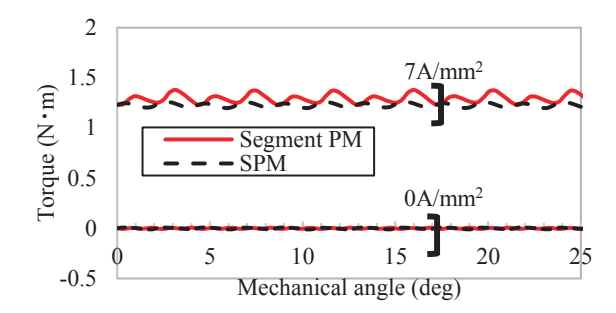


**Fig. 17** Comparison of torque waveform (Redesign drone motor)

#### 5. Conclusions

This paper presented a novel improving a reluctance torque of outer-rotor-type Segment PM motor, and investigation about applying to a drone motor.

First, the Segment PM is adapted to drone motor, and it is compared with SPM. Improving reluctance torque of the motor that was calculated in previous paper is difficult because the torque ripple is significantly increased. Therefore, the Segment PM is applying to drone motor because it has low torque ripple. So, the Segment PM is calculated and compared with SPM. As the results, the Segment PM has same magnetic flux and magnet torque. Further, the reluctance torque of SPM is zero, but the one of Segment PM can be used. The torque ripple is almost same.

After that, the current of Segment PM is increased and it is redesigned. The reluctance torque can be used and ratio is about 13% at 7 A/mm². Further, it can reach about 20% at 10A/mm². The torque ripple is also enough low at operated load. So, the Segment PM can utilize the reluctance torque by drone motor than previous motor application.

In future work, we will do the prototype test and compare it with calculation.

**Acknowledgements** This work was supported by JSPS KAKENHI Grant Number JP23K19110.

#### References

- Y.Park, H.Kim, H.Jang, S.Ham, J.Lee, D.Jung: *IEEE Trans. Appl. Supercond.*, 30, 4 (2020).
- S.Sakurai, Y.Uchiyama, K.Nakamura: International Power Electronics Conference, Himeji, 2022.
- M.Z.Islam, S.Choi, M.E.Elbuluk, S.S.R.Bonthu, A.Arafat, J.Baek: *Energies 2021*
- 4) A.Bozkurt, A.F.Baba, Y.Oner: Energies 2021
- D.Yu, X.Huang, Y.Fang, X.Zhang, :IEEE International Conference on Applied Superconductivity and Electromagnetic Devices, Tianjin, 2018.

Received Apr. 29, 2025; Revised Jun. 22, 2025; Accepted Jul. 23, 2025

J. Magn. Soc. Jpn., 49, 110-114 (2025)

<Paper>

### Optimization of magnet angles for three-dimensional position control with three permanent magnets

H. Sakuma, S. Sawada\*, and T. Azuma

School of Engineering, Utsunomiya Univ., 7-1-2 Yoto, Utsunomiya 321-8585, Japan \*Graduate School of Regional Development and Creativity, Utsunomiya Univ., 7-1-2 Yoto, Utsunomiya 321-8585, Japan

In the three-dimensional position control of a small permanent magnet using three base magnets, an advanced control method that incorporates feedforward and feedback control is required to extend the control range and increase speed. Feedforward control requires knowledge of the angles of the base magnets, such that when the controlled magnet is placed in a certain position, the force acting on it is zero. In this study, the covariance matrix adaptation evolution strategy is used to determine the angles of the three magnets at which the force acting on the controlled magnet is zero. As a result of the optimization, it was confirmed that, to lift the controlled magnet upward, the three magnets should be turned in the positive direction (N-pole facing outward), and to move the stable point of the controlled magnet away from a certain base magnet, the magnet should be turned in the negative direction. A comparison of the optimization results with the experimental results showed that the rotation directions of the three magnets matched, but the rotation angles were smaller in the experiment. One possible reason is the inclination of the controlled magnet.

Keywords: three-dimensional control, permanent magnet, evolutionary algorithm, covariance matrix adaptation evolution strategy, finite element method

#### 1. Introduction

The position control technology of magnetic materials using magnetic fields is expected to be applied to medical fields such as drug delivery and capsule endoscopy, as well as in industrial fields such as non-contact transport and magnetic bearings. This technique is mainly divided into gradient pulling and helical or sperm-like propulsion techniques<sup>1)</sup>. Gradient pulling utilizes the translational force exerted by magnetic moments in a magnetic-field gradient. Although a controlled magnetic material has a simple structure, it is difficult to move it in an arbitrary direction without successfully creating a magnetic field. Although there are few reports on 3D position control, there are examples of using eight electromagnets<sup>2)</sup> and eight permanent magnets<sup>3)</sup>.

Recently, a technique to control the position of a tiny permanent magnet in three dimensions using only three permanent magnets has been reported4). As shown in Fig. 1(a), the magnetic field was controlled by rotating radially magnetized neodymium magnets (hereafter referred to as base magnets) with stepper motors. The ultimate goal is to achieve magnetic levitation in air, but at present, owing to the slow speed of control, the robot is held in a highly viscous medium to slow its movement. The position of the controlled magnet was monitored using two orthogonally positioned cameras. The translational force acting on the controlled magnet was determined using Eq. (1).

$$\mathbf{F} = \nabla(\mathbf{m} \cdot \mathbf{B}) \tag{1}$$

, where m is the magnetic moment of the controlled

Corresponding author: H. Sakuma (e-mail: hsakuma@cc.utsunomiya-u.ac.jp).

magnet and  $\boldsymbol{B}$  is the magnetic flux density. The Z position was controlled by rotating the three base magnets in unison. For the XY position control, magnet coordinates were introduced, which correlated the XY positions with the angles of the three base magnets<sup>4)</sup>. This operating principle was incorporated into a simple feedback control system. It consisted of only one set of feedback gains and position dependency was not incorporated. However, the

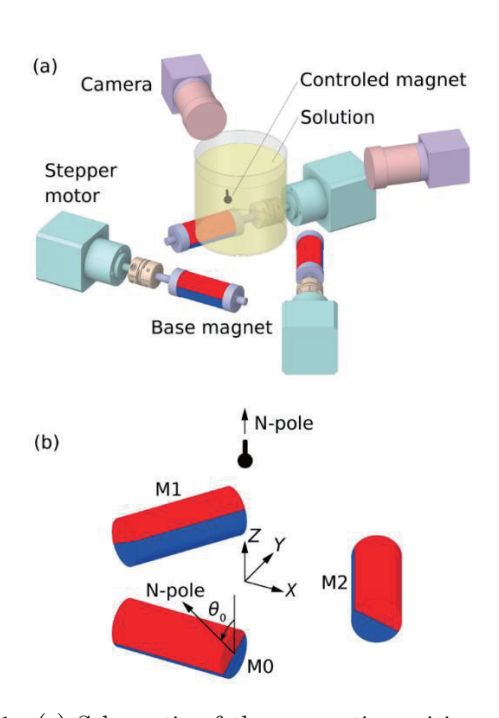


**Fig. 1** (a) Schematic of the magnetic position control system and (b) numbers and angles of the base magnets and the coordinates of the controlled magnet.

angles of the base magnets at which the controlled magnet is most stable may depend on its position. They correspond to the converged values of the base magnet angles when holding the controlled magnet stationary at that position. This information enables feedforward control, which is expected to improve the controllability and expand the controllable range. In practice, as indicated by Earnshaw's theorem<sup>5)</sup>, this system is unstable; therefore, it is necessary to adopt a two-degree-of-freedom control<sup>6)</sup> that combines feedforward control and feedback control.

Feedforward control requires knowledge of the angles of the base magnets, such that when the controlled magnet is placed at a certain position, the force acting on it is zero. Once the angles of the base magnets are determined, the magnetic field distribution around them can be easily obtained using the finite element method (FEM). Conversely, it is difficult to determine the angles of the base magnets that produce the desired magnetic field or force acting on the controlled magnet. Such problems can be solved using evolutionary algorithms, which are optimization methods that mimic biological evolution. The covariance matrix adaptation evolution strategy (CMA-ES)7) is an evolutionary algorithm that uses a covariance matrix to determine the direction of evolution, allowing efficient optimization of noisy functions. In addition, the number of parameters to be set is small compared with other evolutionary algorithms, such as genetic algorithms, and optimization is performed almost automatically. In this study, CMA-ES was used to determine the angles of the base magnets at which the force acting on the controlled magnet was zero.

#### 2. Methods

The base magnets were radially magnetized cylindrical neodymium magnets (diameter: 20 mm, length: 50 mm). The three base magnets (M0-M2) were placed in the center of the sides of an equilateral triangle with a side length of 180 mm. As shown in Fig. 1 (b), the base magnet angle  $(\theta_0 - \theta_2)$  was set to zero when the N-pole faces the +Z direction, and the outward rotation was positive. The controlled magnet was an axially magnetized cylindrical ferrite magnet (diameter: 3 mm, length: 3 mm). The magnetic moment, measured using a vibrating sample magnetometer, was 5.9×10-3 A·m<sup>2</sup>. It was buried in a plastic sphere of 3-mm radius; a plastic rod of 6-mm length was attached to the sphere to detect the direction. As shown in Fig. 1 (b), the position of the controlled magnet is defined by the center of the equilateral triangle of the base magnet as the origin. The controlled magnet was immersed in polyvinyl alcohol and borax aqueous solution to impede movement. The mass of the magnetic object was 220 mg (gravity was 2.2 mN), and the buoyancy due to the solution was estimated to be 1.3 mN based on Archimedes' principle.

A three-dimensional FEM simulator was used to obtain the forces acting on a controlled magnet placed at a certain position at a certain base magnet angle. The

standard mesh size was 0.5 mm in a 6 mm cube area centered on the position of the controlled magnet, and 2 mm elsewhere. The internal magnetic flux density of the base magnets was set to  $1.4~\rm T^{8)}$ . The controlled magnet was assumed to have a magnetic moment (without volume) pointing in the +Z direction, and the magnetic force was calculated using Eq. (1). With the operating principle used in this study, it was not possible to independently control position and orientation. There was only a slight change in orientation accompanying the change in the position. For information on the influence of changes in orientation on position control, refer to Ref. 4. The field gradient was calculated using the change in the magnetic field at points located 1 mm from the point of interest.

The base magnet angles at which the absolute value of the force acting on the controlled magnet was minimized were obtained using CMA-ES. CMA-ES was implemented using DEAP, an evolutionary computation library for Python<sup>9)</sup>. One set of base magnet angles was considered as an individual. The recommended value of Eq. (2) was used for the number of individuals in one generation<sup>7)</sup>.

$$\lambda = 4 + floor(3 \times \log N) \tag{2}$$

, where N denotes the size of the problem. In the case of optimizing three magnet angles, N is three. The magnetic field distribution was calculated using FEM from the magnet angles of each individual. Among the  $\lambda$  individuals,  $\mu$  individuals with a small objective function in Eq. (3) were selected.

$$f = |F_{X}| + |F_{Y}| + |F_{Z} - mg + F_{b}|$$
 (3)

, where  $F_X$ ,  $F_Y$ , and  $F_Z$  are the magnetic forces in the X, Y, and Z directions, respectively, mg is gravity, and  $F_b$  is buoyancy.  $\mu$  was determined by Eq.  $(4)^{7}$ .

$$\mu = \text{floor}(\lambda/2).$$
 (4)

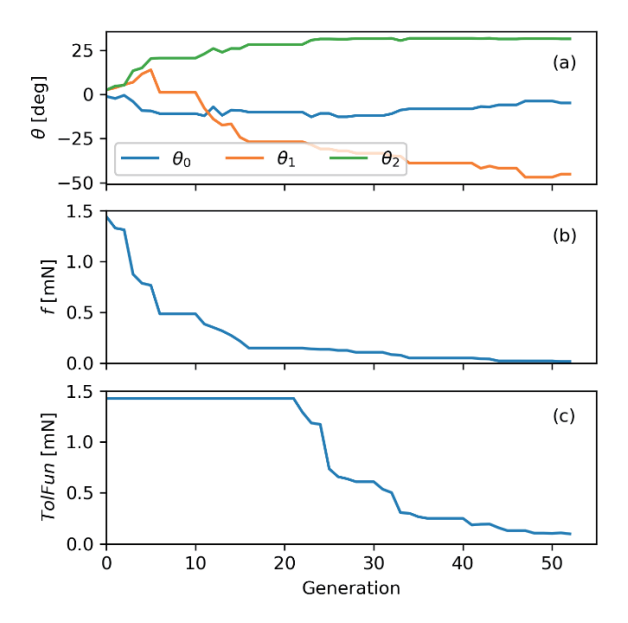


**Fig. 2** Optimization process for X=15 mm, Y=0 mm, and Z=55 mm. (a) Angles of base magnets, (b) objective function, and (c) *TolFun*.

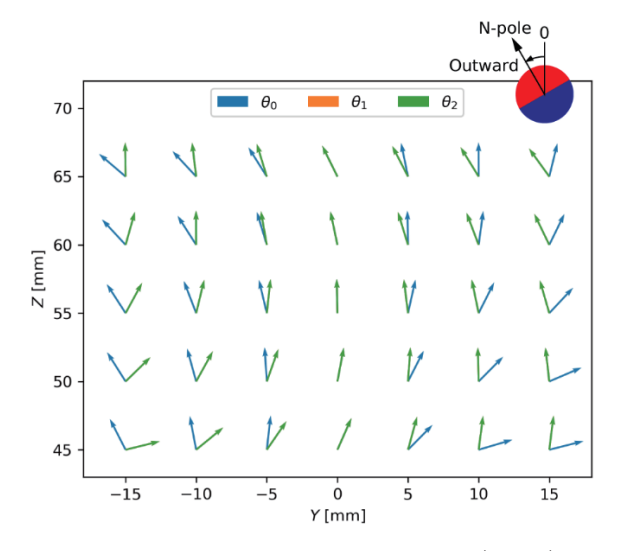


**Fig. 3** Optimization results for YZ plane (X = 0). The inset shows the definitions of angles  $\theta_0 - \theta_2$ .

The default values of CMA-ES and DEAP were used to set the update. The calculation was terminated when the following two conditions were met<sup>8)</sup>. The number of generations exceeds *TolFunIter*<sup>10)</sup> in Eq. (5).

$$TolFunIter = 10 + ceil(30 \times N/\lambda)$$
 (5)

When finding the difference between the maximum and minimum values in the list of minimum values of the objective function in the most recent *TolFunIter* generations, the difference (*TolFun*<sup>10)</sup>) is smaller than 0.1 mN. Figure 2 shows an example of the optimization process. Starting from zero, the angles of the base magnets moved to those where the objective function was the smallest. *TolFun* dropped below 0.1 mN in the 53rd generation, when the changes in the base magnet angle and objective function were sufficiently small, indicating

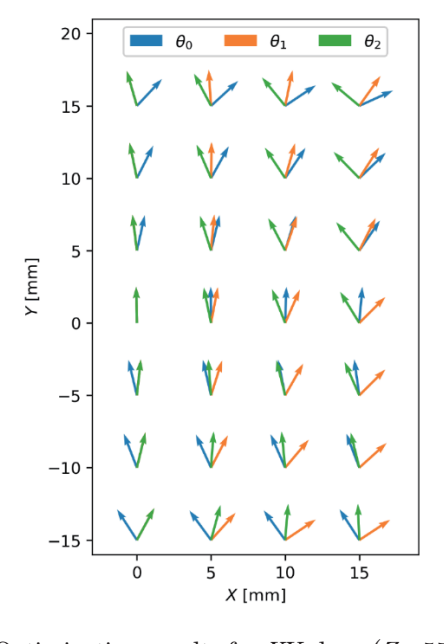


**Fig. 4** Optimization results for XY plane (Z = 55 mm).

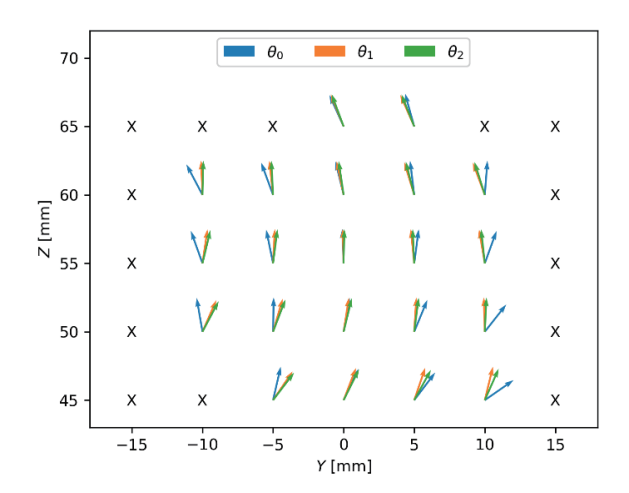


**Fig. 5** Experimental results for YZ plane (X = 0). The points indicated with "X" are those at which the controlled magnet could not be held stably.

that the optimization had converged.

#### 3. Optimization results

As this problem is multimodal and there are many extreme values, the answer is not univocally determined 11). For feedforward control, the angle of the base magnet should change continuously with respect to the changes in position; therefore, it is necessary to induce such a solution. To achieve this, constraints were imposed, and initial values were devised. For X = Y = 0,  $\theta_0 - \theta_2$  must be equal by symmetry. Therefore, the optimization was performed by imposing the constraint  $\theta_0 = \theta_1 = \theta_2$ . The initial values were set as  $\theta_0 = \theta_1 = \theta_2 = 0$ . Figure 3 shows the optimization results for the base magnet angle when the controlled magnet is in the YZ

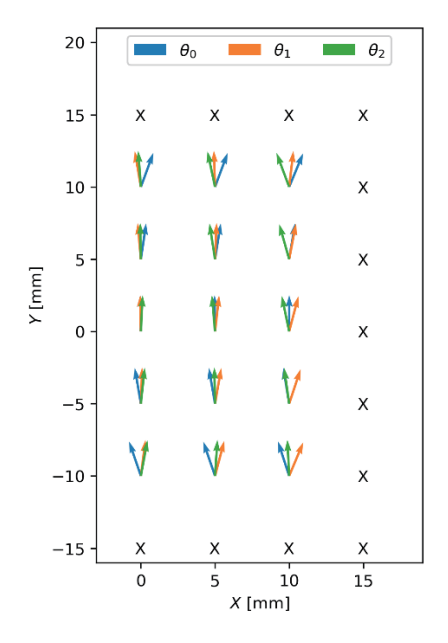


**Fig. 6** Experimental results for XY plane (Z = 55 mm).

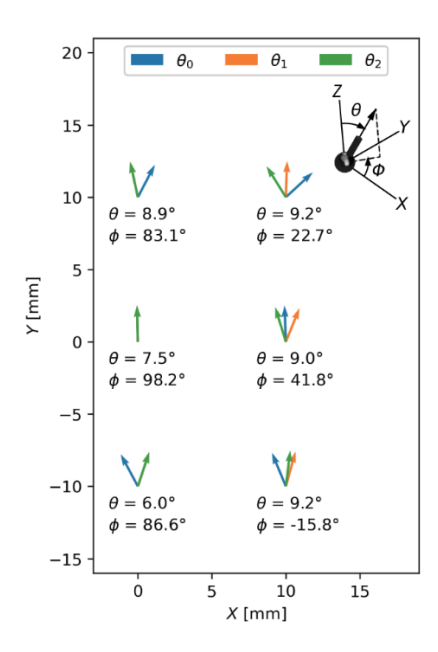


Fig. 7 Inclination of the controlled magnet acquired in the experiment and optimization results based on the inclination. The inset shows the definitions of inclination angles.

plane (X=0). The arrows represent the angles of the three base magnets; upward is  $0^{\circ}$ , and counterclockwise is positive. To lift the controlled magnet upward, the three base magnets must be turned to the positive side. From symmetry,  $\theta_1 = \theta_2$  in the YZ plane. Therefore, for  $Y \neq 0$ , this constraint was imposed for the optimization. To move the stable point of the controlled magnet in the +Y direction,  $\theta_0$  must be turned in the negative direction, and  $\theta_1$  and  $\theta_2$  must be turned in the positive direction. Note that to generate a magnetic force in the +Y direction, it is necessary to turn  $\theta_0$  in the positive direction and  $\theta_1$  and  $\theta_2$  in the negative direction, which is the opposite relationship to the stable point<sup>4</sup>.

Subsequently, the XY planes were considered. From symmetry, +X and -X are the same; therefore, the minus side is omitted. Figure 4 shows the optimization results for the base magnet angle in the XY plane (Z = 55 mm). For X = 0, the values should be the same as those in Fig. 3, and the optimization is omitted. For some XY points with  $X \neq 0$ , the magnet angles fell into false extremes. In this case,  $\theta_0$ – $\theta_2$  should have different values and the constraints cannot be used. Therefore, the angles for X=0 and identical Y values were used as initial values. The trend is the same as that in the YZ plane, and it can be seen that to set the stable position in the +X direction,  $\theta_1$ should be turned in the negative direction and  $\theta_2$  in the positive direction. As described above, the optimization results fully support the control principle reported in Ref. 4.

#### 4. Comparison with experiments

The optimization results were compared with the

experimental results. The controlled magnet was stabilized using feedback control at each position. Figures 5 and 6 show the readings of the angles at that time. Control became difficult when the absolute values of X and Y were large or when Z was approximately 10 mm away from 55 mm. In Figs. 5 and 6, the points indicated with "X" are those at which the controlled magnet could not be held stably. The angles of the base magnets at each point were approximately consistent with the optimization results. However, the change in angle was smaller in the experiment with respect to X=Y=0 and Z=55 mm, where  $\theta_0-\theta_2$  was almost zero. This difference in angles increased as the position moved away from X = Y = 0 and Z = 55 mm. One possible cause for this difference is the tilt of the controlled magnet, which can be measured from camera images. The angle between the Z-axis and the magnetic moment of the controlled magnet (S-pole to N-pole) is defined as  $\theta$ . The angle between the X-axis and the projection of the magnetic moment onto the XY plane is defined as  $\phi$ . The inclination angles of the controlled magnet at typical 6 points on the XY plane are shown in Fig. 7. The results of optimization with CMA-ES under the assumption of the inclination of the controlled magnet are also shown in the figure. Compared with the optimization results assuming zero inclination (Fig. 4) and the experimental results (Fig. 6), they are close to the experimental results for X = 10 mm, while they are close to the optimization results for X=0. Hence, the inclination of the controlled magnet may be a factor in the difference between the optimization and experimental results. However, it is also necessary to consider other factors, such as the different magnetic flux densities of the base magnet and controlled magnet.

#### 5. Summary

The angle of the base magnet, such that the controlled magnet was stable at each position, was optimized using CMA-ES. The optimization results fully support the control principles reported in the literature. The optimization results generally agreed with the experimental results; however, the angle variation tended to be larger than the experimental values. The optimization results can be used for feedforward control in the future

**Acknowledgements** This work was supported by JSPS KAKENHI (grant numbers 21K12662 and 25K07644). The VSM measurement was performed at the Center for Instrumental Analysis, Utsunomiya University.

#### References

- L. Yang and L. Zhang: Annu. Rev. Control Robot. Auton. Syst. 4, 509 (2021).
- M. P. Kummer, J. J. Abbott, B. E. Kratochvil, R. Borer, A. Sengul and B. J. Nelson: *IEEE Trans. Robot.* 26, 1006 (2010).
- 3) P. Ryan and E. Diller: IEEE Trans. Robot. 33, 1398 (2017).
- 4) H. Sakuma: Sci. Rep. 13, 18052 (2023).
- 5) S. Earnshaw: Trans. Camb. Phil. Soc. 7, 97 (1842).
- 6) K. J. Åström and R. M. Murray: Feedback Systems: An

- Introduction for Scientists and Engineers (Princeton Univ. Pr., Princeton, 2021).
- 7) N. Hansen and A. Ostermeier: Evol. Comput. 9, 159 (2001).
- 8) H. Sakuma: J. Magn. Magn. Mater. **566**, 170315 (2023).
- 9) F.-A. Fortin, F.-M. De Rainville, M.-A. Gardner, M. Parizeau, and C. Gagné: *J. Mach. Learn. Res.* **13**, 2171 (2012).
- 10) N. Hansen: Proc. the 11th Annual Conference on Genetic and Evolutionary Computation, ed. by G. Raidl, Montreal, 2009,
- inria-00382093 (Association for Computing Machinery, New York, 2009).
- 11) H. Sakuma and T. Nakagawara: <br/> J. Magn. Magn. Mater.  $\bf 527,$  167752 (2021).

Received Jun. 03, 2025; Revised Jul. 09, 2025; Accepted Aug. 07, 2025

J. Magn. Soc. Jpn., 49, 115-120 (2025)

<Paper>

# Estimating magnetometer position and orientation at extended distance from the calibration coil array in a magnetically shielded room

T. Fukui\*, T. Shibuya\*\*, and Y. Adachi\*, \*\*\*

\*Graduate School of Engineering, Kanazawa Institute of Technology, 7-1 Ohgigaoka, Nonoichi, Ishikawa 921-8501, Japan \*\*Advanced Products Development Center, TDK Corporation, 2-15-7 Higashiowada, Ichikawa, Chiba 272-8558, Japan

We investigate methods for estimating the positions, orientations, and sensitivities of magnetic sensors using multiple coils with known properties, a process we refer to as calibration measurement. In conventional calibration conducted inside a magnetically shielded room (MSR), a systematic estimation error was observed when the distance between the sensors and the coils was increased. This error was caused by demagnetizing fields resulting from the high permeability of shielding materials used in the walls, floor, or ceiling of the MSR. In this study, we propose a new calibration approach that incorporates an approximate model of the demagnetizing field induced by such materials. The effectiveness of the proposed method was validated through two types of model experiments: a simplified setup and a practical setup. The results demonstrated that, even when the sensors and coils were placed farther apart from each other within the MSR, the proposed method effectively reduced the systematic estimation error by accounting for the influence of the demagnetizing field.

Keywords: calibration, biomagnetic measurement, soft magnetic materials, demagnetizing field, magnetic sensors.

#### 1. Introduction

Biomagnetic measurement is a noninvasive technique for detecting extremely weak magnetic fields in the fT to pT range, which are generated by electrical activity associated with physiological functions of the human body. Visualization of the functions of the brain, heart, nerves, muscles, and other related organs, achieved by estimating the internal current distribution from detected biomagnetic fields, is expected to contribute to the diagnosis of various diseases<sup>1)</sup>.

Traditionally, superconducting quantum interference devices (SQUIDs) have been the primary sensors used in biomagnetic measurements due to their extremely high resolution, capable of detecting magnetic fields as small as a few fT, and have supported numerous fundamental and clinical studies. However, their reliance on liquid helium cooling increases the cost of installation and operation. In recent years, room-temperature magnetic sensors such as optically pumped magnetometers (OPMs) and magnetoresistive (MR) sensors have attracted increasing attention as flexible alternatives for biomagnetic measurements<sup>2)-5)</sup>.

To accurately estimate the internal current distribution, it is essential to have precise information about the position, orientation, and sensitivity of the magnetic sensors used for measurement. In biomagnetic measurements, it is common to arrange an array of several tens to over a hundred magnetic sensors near the target region to measure the magnetic field distribution. However, if the sensor information is inaccurate, the estimated current distribution may be unreliable.

Methods for estimating the position, orientation, and sensitivity of magnetic sensors based on reference magnetic fields generated by multiple predetermined coils were proposed and referred to as calibration measurements<sup>6),7)</sup>. The calibration is carried out through the following steps. First, reference magnetic fields are generated using multiple coils whose position, orientation, diameter, and current are known. These fields are then detected by magnetic sensors whose position, orientation, and sensitivity are unknown. Next, theoretical magnetic fields are calculated using the Biot-Savart law, based on assumed sensor parameters and known coil parameters. These computed fields are compared with the actual sensor outputs. This process is repeated, typically up to tens of thousands of times, to identify the combination of sensor parameters that minimizes the difference between the theoretical and measured values.

We are investigating calibration methods for various SQUID- and MR sensor-based biomagnetic measurements, and reported that calibrated sensor arrays improve the reliability of magnetic source localization<sup>8),9)</sup>. More recently, studies of parameter estimation for OPMs using reference magnetic fields have also been reported<sup>10)</sup>.

However, calibration can be affected by distortion of the reference magnetic field, reducing estimation accuracy. To suppress environmental noise, these measurements are typically conducted inside a magnetically shielded room (MSR), which is constructed using high-permeability soft magnetic materials. When reference magnetic fields are generated inside the MSR, demagnetizing fields are induced and can distort the magnetic field distribution around the sensors. This effect becomes more pronounced as the distance between sensors and coils increases, since the reference field generated by the coils weakens while the relative influence of the demagnetizing field on the sensors becomes stronger. Consequently, this can cause

Corresponding author: T. Fukui (e-mail: t.fukui.ac25@gmail.com).

<sup>\*\*\*</sup> Applied Electronics Laboratory, Kanazawa Institute of Technology, 3 Amaike, Kanazawa, Ishikawa 920-1331, Japan

systematic errors in the estimation results. To mitigate this, sensors and coils have traditionally been placed as close together as possible during calibration. Nonetheless, maintaining a certain distance during calibration is being required for a more flexible system.

To incorporate the effects of demagnetizing fields into calibration, it is essential to model the demagnetizing field distribution induced by soft magnetic materials. However, conventional analytical modeling based on demagnetizing factors is limited to typical shapes such as ellipsoids and has difficulty computing demagnetizing fields induced by non-uniform magnetic fields<sup>11)</sup>. In contrast, numerical methods such as the finite element method (FEM) are not limited by such restrictions, but their high computational cost makes them unsuitable for calibration, which requires magnetic field calculations to be repeated tens of thousands of times.

In this study, we propose a new calibration method that incorporates the influence of demagnetizing fields induced by an MSR. We first describe how these effects can be incorporated into the calibration process, and then present an approximate model of the demagnetizing field distribution suitable for calibration. This model satisfies two main requirements: flexibility in designing the shape of magnetic materials and low computational cost for repeated field calculations. To evaluate the effectiveness of the proposed method, we conducted two experiments. The first validated the feasibility of the model under idealized conditions, while the second demonstrated its practical performance under settings that simulate actual biomagnetic measurements. These results show that the proposed method can reduce estimation errors caused by demagnetizing field effects, even when the sensor-coil distance is increased within an MSR.

#### 2. Materials and Methods

#### 2.1 Sensor calibration using multiple calibration coils

We computed the reference magnetic fields from multiple predetermined coils and numerically searched for the sensor parameters that best explain the measured sensor outputs. The coil-generated fields were first calculated assuming a uniform air medium<sup>12)</sup>, and the demagnetizing field was subsequently added. This procedure aimed to account for the influence of demagnetizing fields, which can affect sensor outputs when magnetic materials are present in the calibration setup.

The schema of the calibration setup is shown in Figure 1. In this model, a uniaxial scalar magnetic sensor was assumed. The position and orientation of the i-th sensor were represented by five variables: position  $(x_i, y_i, z_i)$  and orientation  $(\theta_i, \varphi_i)$ . The sensor array consisted of  $N_s$  sensors, and unknown parameters of each sensor, for i = 1 to  $N_s$ , were estimated sequentially. Regarding the coils, their position, orientation, diameter, and current were set as known parameters. The coil array consisted of  $N_c$  coils, each of which was excited one after another. All positions were described relative to a reference origin fixed with respect to the array of coils.

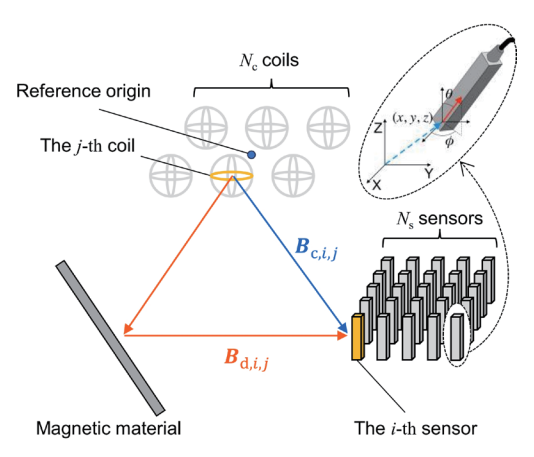


**Fig. 1** Model of calibration with magnetic material and sensor parameters: position and orientation.

The theoretical magnetic field at the *i*-th sensor position due to the *j*-th coil was defined as  $\boldsymbol{B}_{\operatorname{cal},i,j}$ , and the measured sensor output voltage was denoted by  $V_{\operatorname{meas},i,j}$ . Conventionally, the coil-generated field applied to the sensor  $\boldsymbol{B}_{\operatorname{c},i,j}$  is only considered so that  $\boldsymbol{B}_{\operatorname{cal},i,j} = \boldsymbol{B}_{\operatorname{c},i,j}$ . In contrast, this study introduces an additional term  $\boldsymbol{B}_{\operatorname{d},i,j}$ , denoting the demagnetizing field induced by magnetic materials and affecting the *i*-th sensor. The theoretical field was modeled as:

$$B_{\text{cal}, i, j} = B_{c, i, j} + B_{d, i, j}.$$
 (1)

The way to calculate  $\boldsymbol{B}_{\mathrm{d},i,j}$  is described in Section 2.2.

Here, an evaluation function  $E_i$  for the i-th sensor was calculated as follows:

$$E_{i} = 1 - \frac{(B_{\text{cal}, i} \cdot V_{\text{meas, i}})^{2}}{|B_{\text{cal}, i}|^{2} |V_{\text{meas, i}}|^{2}} , \qquad (2)$$

where  $V_{\text{meas}, i} = [V_{\text{meas}, i, 1}, ..., V_{\text{meas}, i, Nc}]$  and  $B_{\text{cal}, i} = [B_{\text{cal}, i, 1}, ..., B_{\text{cal}, i, Nc}]$ , with each  $B_{\text{cal}, i, j}$  being the component of the vector field projected onto the sensor's orientation. When  $E_i$  is minimized, the theoretical magnetic field is considered to best explain the i-th sensor's measured output, i.e., the reference magnetic field. The parameter set used in the computation of  $B_{\text{cal}, i}$  that minimizes  $E_i$  is regarded as the optimal estimated parameters for the i-th sensor.

The sensor sensitivity  $g_i$  was excluded from the parameter search and was computed after optimization using the following expression:

$$g_i = \frac{\left|B_{\text{cal},i}\right|^2}{B_{\text{cal},i} \cdot V_{\text{meas},i}} \ . \tag{3}$$

As an indicator of the goodness of fit of the estimation results, the following index was introduced:  $gof_i = (1 - E_i) \times 100$  (%). A value closer to 100 indicates better agreement between the theoretical and measured values.

#### 2.2 Model of demagnetizing field using magnetic dipoles

A model using magnetic dipoles was introduced to simulate the demagnetizing field generated by magnetic materials. Here, the magnetic dipoles were virtually placed in space solely to reproduce the demagnetizing field. It should be noted that these dipoles do not represent actual magnetic domains formed within the magnetized material.

In this study, magnetic materials were assumed to be soft magnetic plates, such as the walls, floor, or ceiling of a typical MSR. For simplicity, only the demagnetizing field from a single plate was considered, assuming the floor to be the primary source of the demagnetizing field. The approximate position of the magnetic material affecting calibration was also assumed to be known.

Figure 2 schematically illustrates the proposed model based on magnetic dipoles, which was designed to simulate the demagnetizing field from magnetic materials in a simplified and computationally feasible manner. A magnetic dipole array was constructed by arranging dipoles in a square grid on the x-y plane at intervals of w, resulting in a total of  $N_p$  dipoles, each identified by an index k.

Two variables were treated as unknown parameters to be estimated through calibration measurements. The first is the distance  $d_i$  from the reference origin to the plane on which the magnetic dipole array is arranged. Here,  $d_i$  was estimated as the virtual distance to a magnetic dipole array that best reproduces the demagnetizing field term  $\mathbf{B}_{d_i,i,j}$  at the i-th sensor, induced by the j-th coil via the magnetic material. It should be noted that  $d_i$  does not represent the distance to the actual magnetic material plate.

The other unknown parameter to be estimated is the proportional constant  $a_i$ , which is used to compute the magnetic moment of each magnetic dipole. When the j-th calibration coil generates the magnetic field  $\mathbf{B}_{c,i,j}$ , it simultaneously produces a magnetic field  $\mathbf{B}_{p,j,k}$  at the location of the k-th magnetic dipole. The magnetic moment  $\mathbf{m}_{j,k}$  of the k-th dipole was assumed to be proportional to  $\mathbf{B}_{p,j,k}$ , and was expressed as follows:

$$\mathbf{m}_{j,\,k} = \alpha_i \, \mathbf{B}_{\mathsf{p},\,j,\,k},\tag{4}$$

where  $\alpha_i$  was assumed to be the same for all dipoles.

Based on the above assumptions, the demagnetizing field term  $\mathbf{B}_{d,i,j}$  was calculated as a sum of the magnetic fields generated by the  $N_p$  magnetic moments  $\mathbf{m}_{j,k}$ . First, the field  $\mathbf{B}_{p,j,k}$  was computed, and then the resulting magnetic moment  $\mathbf{m}_{j,k}$  was used to determine  $\mathbf{B}_{d,i,j}$  according to the following expression:

$$\boldsymbol{B}_{\mathrm{d},\,i,\,j} = \frac{-\mu_0}{4\pi} \sum_{k=1}^{N_\mathrm{p}} \frac{1}{|\boldsymbol{r}_{i,\,k}|^3} \left[ \boldsymbol{m}_{j,\,k} - \frac{3}{|\boldsymbol{r}_{i,\,k}|^2} (\boldsymbol{m}_{j,\,k} \cdot \boldsymbol{r}_{i,\,k}) \, \boldsymbol{r}_{i,\,k} \right], \tag{5}$$
 where  $\boldsymbol{r}_{i,\,k}$  is the position vector from the  $k$ -th magnetic dipole to the  $i$ -th sensor.

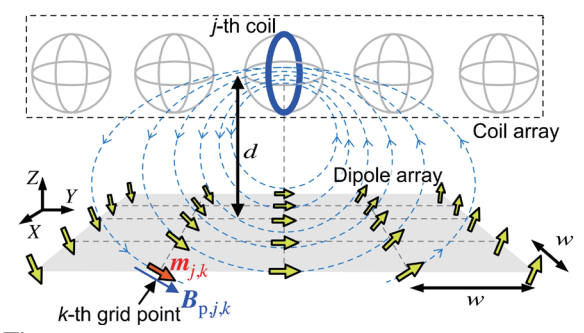


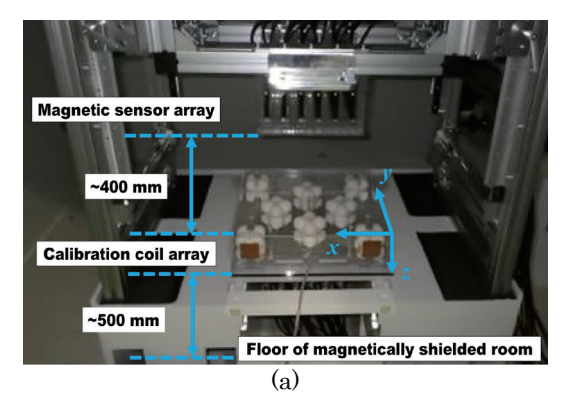
**Fig. 2** Schema of dipole array used for approximate simulation of the demagnetizing field.

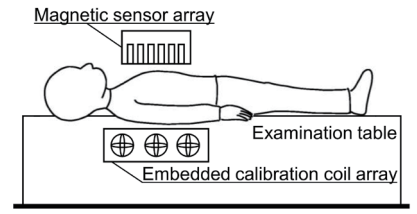
#### 2.3 Experimental setup

To validate the proposed calibration method, two experimental setups were examined. The first setup was designed under ideal conditions assumed in the proposed approach to verify its feasibility. In contrast, the second setup simulated actual bio-magnetic measurements, with Figure 3(a) showing the interior of the MSR used in the experiment.

Each experimental setup included a calibration coil array with multiple coil bobbins, a magnetic sensor array, and magnetic material. The coils were sequentially activated to generate a reference magnetic field, which induced a demagnetizing field from the magnetic material. The sensors were exposed to both fields and responded with voltage signals.

Figure 3(c) shows a CAD-based schematic 3D model of the coil bobbin. Eight bobbins, each containing three orthogonal coils, were used to construct the calibration coil array, in which all 24 coils were operated independently. Figure 3(d) shows the schematic diagram of the calibration coil array used in the experiment. The





Floor of magnetically shielded room
(b)

Origin 2.x

Fig. 3 Experimental setups: (a) Setup for Experiment 2 simulating a practical biomagnetic measurement, (b) conceptual image of a prospective magnetocardiograph system in which the sensor array and calibration coil array are integrated, (c) schematic model of a calibration coil bobbin, and (d) schematic diagram of the calibration coil array.

reference origin used for analysis was set at the center of the calibration coil array, as shown in the figure. To ensure high-precision generation of the reference magnetic field, the mechanical tolerance of the bobbins and their assembly was set to be  $\pm 0.1$  mm. Two experiments shared the same coil array structure.

The magnetic sensors were arranged at uniform intervals in a plane parallel to the *x-y* plane, with each sensor's sensitive axis oriented in the negative *z*-direction.

A tone-burst sinusoidal current with a frequency of 80 Hz and a duration of 300 ms was used as the reference signal input to the calibration coils. The current amplitude applied to each coil was set to 20 mA<sub>P-P</sub> in Experiment 1 and 5 mA<sub>P-P</sub> in Experiment 2. The magnetic field detected by the sensors corresponded to approximately 10 nT<sub>P-P</sub> in Experiment 1 and 500 pT<sub>P-P</sub> in Experiment 2.

The voltage signal  $V_{\text{meas},i,j}$  outputted from each magnetic sensor was obtained through the following procedure. In Experiment 1, data were digitally acquired at a sampling rate of 2 kHz, and in Experiment 2, at 1 kHz. For the improvement of signal-to-noise ratio, the same measurement sequence was repeated approximately 80 to 100 times, and the signal was averaged. A fast Fourier transform (FFT) was then performed on the averaged signal, and the 80 Hz component was extracted and defined as the value of  $V_{\text{meas},i,j}$ .

The size of the magnetic dipole array used for calculating the demagnetizing field was heuristically determined as w = 100 mm and  $N_{\rm p} = 25$  (= 5 × 5). The estimation of unknown parameters was carried out based on the measured voltage signals  $V_{{\rm meas},i,j}$  together with the analytically derived magnetic fields  $B_{{\rm c},i,j}$  and  $B_{{\rm d},i,j}$ .

The estimation accuracy of the calibration measurements was evaluated based on the estimated positions and orientations of the sensors. Instead of using absolute values, the evaluation focused on the deviations relative to reference positions and orientations. To this end, for each experiment, the estimated results were aligned to the reference by applying rotational transformations<sup>13)</sup>, and remaining differences were defined as estimation errors. The reference positions and orientations were obtained in advance for each experimental setup, based on an initial calibration measurement in which the sensors and coils were placed in close proximity—close enough that the influence of the demagnetizing field could be neglected.

To evaluate the spatial distribution of position errors, distribution maps were generated by projecting the estimated sensor positions onto the x-y and y-z planes. The magnitude of the position error at each sensor, denoted as  $\Delta p_i$ , was calculated based on the Euclidean distance between the estimated position and the reference position using the following equation:

$$\Delta p_i = \sqrt{(x_{r,i} - x_{e,i})^2 + (y_{r,i} - y_{e,i})^2 + (z_{r,i} - z_{e,i})^2} , \quad (6)$$

where  $(x_{r,i}, y_{r,i}, z_{r,i})$  and  $(x_{e,i}, y_{e,i}, z_{e,i})$  represent the reference and estimated positions of the *i*-th sensor,

respectively. The orientation error was evaluated using the angle  $\Psi_i$  between the reference and estimated orientations of each sensor, which was calculated as follows:

$$\Psi_{i} = \cos^{-1}\left(\sin(\theta_{r,i})\sin(\theta_{e,i})\cos(\varphi_{r,i} - \varphi_{e,i}) + \cos(\theta_{r,i})\cos(\theta_{e,i})\right). \tag{7}$$

Here,  $(\theta_{r,i}, \varphi_{r,i})$  and  $(\theta_{e,i}, \varphi_{e,i})$  represent the reference and estimated orientations of the *i*-th sensor, respectively.

In addition to the estimation accuracy of sensor positions and orientations, the overall goodness of fit  $(gof_i)$  of the calibration was also evaluated. The  $gof_i$  value indicates how well the theoretical magnetic fields, calculated based on the estimated parameters, agree with the measured sensor outputs. Furthermore, the estimated parameters related to the magnetic material,  $d_i$  and  $\alpha_i$ , were independently evaluated.

For comparison, these analyses were conducted with and without considering the demagnetizing field.

#### 2.3.1 Experiment 1: preliminary setup

This experiment was conducted as a preliminary study to validate the proposed calibration method. To simulate ideal conditions, only a single permalloy panel was used as the magnetic material. In addition, to eliminate the influence of other magnetic materials, the experiment was performed outside the MSR.

We employed MR sensors with relatively lower resolution than those typically used for biomagnetic measurement, since the measurements were conducted outside the MSR. The typical magnetic noise spectral density of the sensors was  $3.2 \text{ pT/}\sqrt{\text{Hz}}$  at 80 Hz.

The calibration coil array had dimensions of  $A=30\,\mathrm{mm}$ ,  $B=100\,\mathrm{mm}$ , and  $C=75\,\mathrm{mm}$  as shown in Figure 3(c) and (d), with each coil consisting of 10 turns. The magnetic sensor array, consisting of 25 (= 5 × 5) sensors, was arranged parallel to the *x-y* plane with a spacing of 40 mm between sensors. To enhance the influence of the demagnetizing field, the sensor array was placed 150 mm apart from the coil array along the *z*-direction. The permalloy panel was positioned approximately 80 mm apart from the coil array on the opposite side of the sensors. The thickness and dimensions of the panel were 1 mm and  $500\times500\,\mathrm{mm}$ , respectively.

#### 2.3.2 Experiment 2: practical setup

This experiment was conducted under conditions that simulated a magnetocardiograph system as shown in Figure 3(a) and (b). The measurements were conducted inside an MSR, where the floor was assumed to be the primary source of the demagnetizing field affecting the calibration, as it was closest to both the coils and the sensors.

The MR sensors used in this experiment were the same type as those used in previous studies on biomagnetic measurements<sup>4)</sup>. Their typical magnetic noise spectral density was  $0.46~\text{pT/}\sqrt{\text{Hz}}$  at 80 Hz, providing higher resolution than that in Experiment 1.

The calibration coil array had dimensions of A = 60 mm, B = 300 mm, and C = 180 mm as shown in Figure 3(c) and

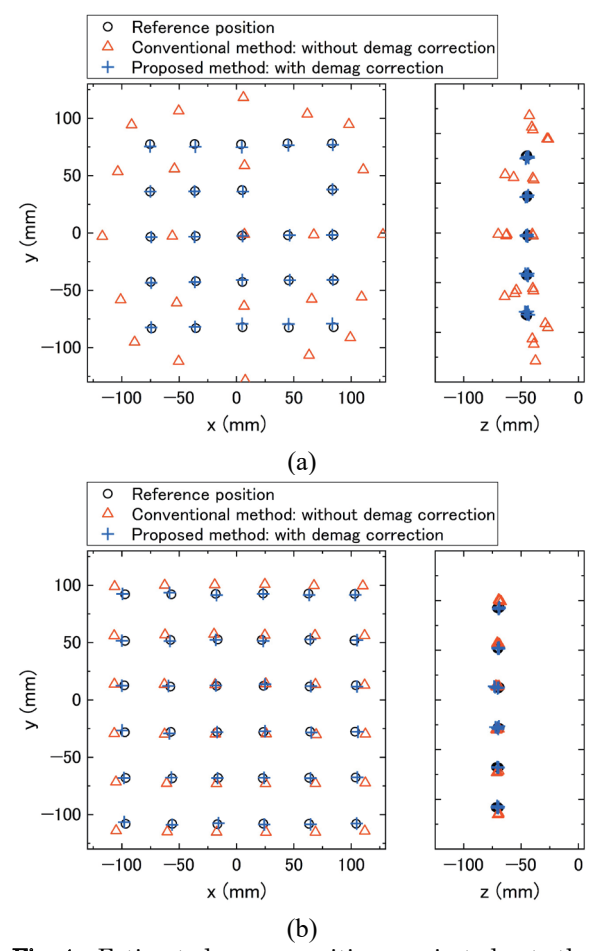


**Fig. 4** Estimated sensor positions projected onto the x-y and y-z planes:(a) Experiment 1, (b) Experiment 2.

(d), with each coil consisting of 10 turns. The magnetic sensor array, consisting of 36 (=6  $\times$  6) sensors, was arranged parallel to the *x-y* plane with a spacing of 40 mm between sensors. The entire sensor array was placed 400 mm above the coil array along the *z*-direction. As shown in Figure 3(b), this distance was chosen to simulate conditions where a subject would be positioned between the sensors and the coils. The distance from the coil array to the floor was set to approximately 500 mm, taking into account the height of the examination table.

#### 3. Results

The proposed method was evaluated in two experiments and compared with the conventional approach. Figure 4 shows the estimated sensor positions projected onto the *x-y* and *y-z* planes, obtained from Experiment 1 and Experiment 2. In Experiment 1, one of the magnetic sensors was excluded from the evaluation due to a malfunction.

In both experiments, the conventional method, which did not account for the demagnetizing field, resulted in systematic estimation errors. In the *x-y* plane, estimated sensor positions were shifted outward from the reference, especially near the edge of the array. On the other hand, the *z*-direction error distribution became more dispersed toward the center of the array in Experiment 1, whereas

**Table 1** Estimation error and GOF with conventional (Conv.) and proposed (Prop.) calibration methods.

	Experiment 1		Experiment 2	
	Conv. Prop.		Conv.	Prop.
$\overline{\Delta p} \pm \sigma \text{ (mm)}$	$31.5 \pm 6.1$	1.6 ± 0.9	$7.4 \pm 2.5$	1.7 ± 0.6
$\overline{\Psi}  \pm  \sigma   (\mathrm{deg})$	$39.0 \pm 13.3$	$1.2 \pm 0.6$	$\begin{array}{c} 2.7 \\ \pm \ 1.1 \end{array}$	$\begin{array}{c} 0.7 \\ \pm \ 0.3 \end{array}$
$\overline{\text{gof}} \pm \sigma$ (%)	$99.649 \pm 0.079$	$99.995 \\ \pm 0.002$	$99.969 \\ \pm 0.002$	$99.998 \\ \pm 0.001$

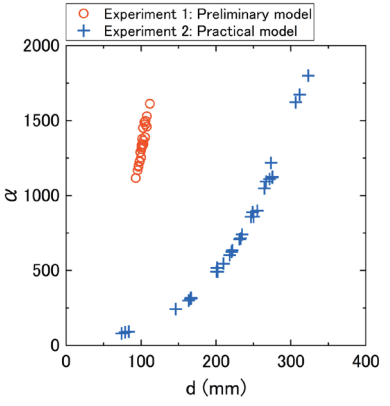


**Fig. 5** Scatter plot of estimated parameters d and  $\alpha$  for all sensors in Experiment 1 and Experiment 2.

no noticeable spread of errors in the z-direction was observed in Experiment 2.

In comparison, the proposed method, which accounts for the demagnetizing field, effectively reduced these systematic errors. As shown in the figures, the estimated positions, denoted by blue crosses, aligned more closely with the reference positions shown as black circles.

Quantitative results are summarized in Table 1. The average position error was reduced by about 30 mm in Experiment 1 and 5.7 mm in Experiment 2. Orientation errors improved by approximately 38 degrees and 2 degrees, respectively. The goodness-of-fit index (gof<sub>i</sub>) also improved: by two orders of magnitude in Experiment 1 and one order in Experiment 2.

Figure 5 shows a scatter plot of estimated d and  $\alpha$  values for all sensors. As seen in the figure, the estimated d values exhibited a wide distribution, especially in Experiment 2, where they ranged from 80 to 350 mm. In both experiments, a tendency was observed in which larger d values were associated with larger  $\alpha$  values.

#### 4. Discussion

The effectiveness of the proposed calibration method, which accounts for the influence of the demagnetizing field, was evaluated through two experiments. The results demonstrated that incorporating the effect of the demagnetizing field significantly reduced the systematic errors observed in conventional methods. Furthermore,

the proposed method was shown to be effective under conditions that simulate actual biomagnetic measurement environments.

Experiment 1 was intentionally designed such that the distance between the magnetic material and the sensor was shorter than in Experiment 2, leading to a greater influence of the demagnetizing field in Experiment 1. Nevertheless, the residual estimation errors of the proposed calibration method were approximately equal in both experiments. This is because the experimental conditions were designed to be comparable except for the influence of the demagnetizing field.

In this study, the dimensions of the dipole array were set to  $400~\mathrm{mm} \times 400~\mathrm{mm}$  because it was assumed that when performing calibration inside an MSR, the effect of the demagnetizing field could be sufficiently accounted for by considering only the floor area beneath the coil array. The observed reduction in estimation errors supports the validity of this assumption.

The demagnetizing field approximation model based on magnetic dipoles proposed in this study is applicable to magnetic materials arranged in a planar form, such as the floor of an MSR. Furthermore, the validity of the model was confirmed through experiments, and it was shown to contribute to the reduction of estimation errors. It also has sufficiently low computational cost to be incorporated into calibration.

On the other hand, several issues remain with the proposed method, as it assumes that only a single plate of magnetic material influences the calibration. Under the conditions of calibration conducted inside the MSR, only the effect from the floor was considered. While this assumption was valid for the experimental setup used in this study, depending on the arrangement of the sensor array and calibration coil array in the MSR, it can be necessary to consider the influence of demagnetizing fields from multiple plates, such as walls. Furthermore, if the magnetic material has a shape that does not conform to the assumptions of the model, such as spherical or cylindrical geometries instead of a flat panel, the estimation accuracy can degrade. Therefore, extending the magnetic dipole array model to account for multiple plates or non-planar magnetic material geometries is an important direction for future work.

The interpretation of the parameters d and  $\alpha$ , which were introduced in the proposed model, remains an issue for future investigation. In the model, d was defined as the distance from a reference origin to the virtual plane where the magnetic dipole array was placed, and it did not directly represent the actual distance to the magnetic material plate. However, the estimated d showed a significant discrepancy from the actual distance especially in Experiment 2. The parameters d and  $\alpha$  are important factors in reproducing the effect of the demagnetizing field, and a detailed investigation of their relationship is required to further clarify their physical significance.

Finally, we considered the potential influence of eddy

currents, which distort the reference magnetic field. As a preliminary investigation, we varied the frequency of the reference magnetic field from 40 Hz to 320 Hz for calibration and observed no significant frequency-dependent change within this range in the estimation results. Therefore, eddy currents were not taken into account in the present experiments. However, for higher frequency sensor applications, the influence of eddy currents becomes non-negligible and should be taken into account in future studies.

#### 5. Conclusion

We proposed a calibration method that modeled the influence of the demagnetizing field induced by magnetic materials and incorporates it into the calibration measurements. The validity of the proposed method was evaluated through two types of experiments. The results demonstrated that even under conditions where the sensors and coils were separated inside a magnetically shielded room, the proposed method could effectively reduce the systematic estimation errors by taking the demagnetizing field into account.

**Acknowledgements** This work was partially supported by TDK Corporation. We would also like to thank OHTAMA CO.,LTD for providing permalloy panels.

#### References

- 1) R. L. Fagaly: Rev. Sci. Instrum., 77, 101101 (2006).
- E. Boto, N. Holmes, J. Leggett, G. Roberts, V. Shah, S. S. Meyer, L. D. Muñoz, K. J. Mullinger, T. M. Tierney, S. Bestmann, G. R. Barnes, R. Bowtell, and M. J. Brookes: Nature, 555, 657 (2018).
- Y. Shirai, K. Hirao, T. Shibuya, S. Okawa, Y. Hasegawa, Y. Adachi, K. Sekihara, and S. Kawabata: *Int. Heart. J.*, 60, 50 (2019).
- T. Tatsuoka, S. Kawabata, J. Hashimoto, Y. Hoshino, K. Sekihara, T. Shibuya, Y. Adachi, and A. Okawa: Sensor Actuat. A-Phys., 374, 115456 (2024).
- A. Kanno, N. Nakasato, M. Oogane, K. Fujiwara, T. Nakano, T. Arimoto, H. Matsuzaki, and Y. Ando: Sci. Rep. 12, 6106 (2022).
- 6) M. Higuchi, H. Kado, K. Chinone, N. Kasai, and Y. Ishibashi: *IEICE Trans.*, **J73-A**, 1167 (1990) (in Japanese).
- T. Yoshida, M. Higuchi, T. Komuro, and H. Kado: Proc. 16th Annu. Int. Conf. IEEE Eng. Adv., New Opportunities Biomed. Eng., 171 (1994).
- 8) Y. Adachi, D. Oyama, Y. Terazono, T. Hayashi, T. Shibuya, and S. Kawabata: *IEEE Trans. Magn.*, **55**, 5000506 (2019).
- Y. Adachi, D. Oyama, M. Higuchi, and G. Uehara: *IEEE Trans. Instrum. Meas.*, 72, 4004210 (2023).
- 10) R. M. Hill, G. R. Rivero, A. J. Tyler, H. Schofield, C. Doyle, J. Osborne, D. Bobela, L. Rier, J. Gibson, Z. Tanner, E. Boto, R. Bowtell, M. J. Brookes, V. Shah, and N. Holmes: arXiv, 2410.08718 (2024).
- K. Ohta: Jikikogaku No Kiso I, p. 35 (Kyoritsu shuppan, Tokyo, 1973) (in Japanese).
- L. D. Landau, E. M. Lifshitz, and L. P. Pitaevskii, Landau and Lifshitz Course of Theoretical Physics, vol. 8. (Pergamon, Izmir Province, Turkey, 1960).
- 13) J. H. Challis: J. Biomech., 28, 733 (1995).

Received Jun. 02, 2025; Accepted Sep. 03, 2025

#### **Erratum**

"Domain Wall Displacement Modulation GMR Sensors with Closed-Loop Current-Field Feedback" K. Komuro, D. Oshima, T. Kato

Journal of the Magnetics Society of Japan 2024, Volume 48, Issue 2, Pages 34-39 https://doi.org/10.3379/msjmag.2403R004

The original article has an error in the equation (3) in section 4.4.

Before:

$$H_{\text{eff}} = H_{ext} - FV_{\text{out}} = \frac{1}{1 + \frac{K_{\text{H} \to \text{V}} \cdot G_{\text{IA}} \cdot G_{OA}}{F}} H_{\text{ext}} = \eta H_{\text{ext}}$$

After correction:

$$H_{\text{eff}} = H_{ext} - FV_{\text{out}} = \frac{1}{1 + K_{\text{H} \to \text{V}} \cdot G_{\text{IA}} \cdot G_{OA} \cdot F} H_{\text{ext}} = \eta H_{\text{ext}}$$

Together with the correction, Fig. 11 and the value of F in the discussion of  $\eta$  for the Open-1 mode have been slightly modified. Since the definition of  $\eta$  was corrected, Fig. 11 was also updated from Fig. (a) to Fig. (b) as shown below. However, the observed trends of increasing non-linearity with respect to  $\eta$  remain identical to those before the correction, and the overall discussion in the paper is not changed by this correction.

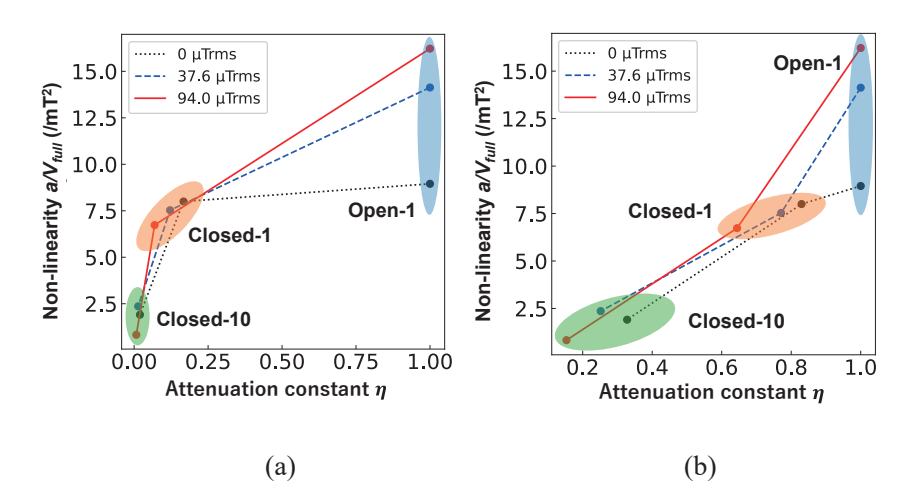


Fig. (a) Original Fig. 11 and (b) updated Fig. 11. Due to the correction in the definition of  $\eta$ , the values of horizontal axis in Fig. (b) are different from those in Fig. (a). However, the increasing trend in non-linearity with respect to  $\eta$  remains unchanged by the correction.

These errors have been corrected in the following PDF and online versions of J-STAGE.

J. Magn. Soc. Jpn., 49, E7-E13 (2025)

<Paper>

### Domain Wall Displacement Modulation GMR Sensors with Closed-loop Current-field Feedback

K. Komuro\*, D. Oshima\*, and T. Kato\*, \*\*

\*Department of Electronics, Graduate School of Engineering, Nagoya University, Furo-cho, Chikusa-ku, Nagoya, 464-8603, Japan

\*\* Institute of Materials and Systems for Sustainability, Nagoya University, Furo-cho, Chikusa-ku, Nagoya, 464-8603, Japan

A novel type of giant magneto-resistance (GMR) sensor utilizing domain wall displacement (DWD) modulation and a closed-loop current-field feedback technique was investigated. In this paper, a Ni<sub>80</sub>Fe<sub>20</sub> free layer was used for the GMR sensor since the uniaxial anisotropy of Ni<sub>80</sub>Fe<sub>20</sub> is smaller than that of the  $(Co_{90}Fe_{10})_{92}B_8$  used in the previous study, resulting in a larger wall displacement with a smaller field. When the domain wall was modulated by a modulation field  $H_{mod} = 94 \,\mu T_{rms}$ , the sensitivity of the sensor increased to 2.6 mV/ $\mu$ T in open-loop mode compared with a sensitivity of 0.98 mV/ $\mu$ T for the sensor without  $H_{mod}$ . Moreover, a significant improvement in the linearity of the output was obtained by operating the DWD GMR sensor in closed-loop mode, and the sensitivity was also increased up to 4.2 mV/ $\mu$ T. The improvement in linearity is considered to be due to the suppression of the displacement of the average position of the domain walls by the current-field feedback. The noise floor of the output of the DWD GMR sensor under closed-loop operation was estimated to be 300 pT/Hz<sup>1/2</sup> at 10 Hz.

Keywords: magnetic sensors, domain wall displacement modulation, current field feedback, GMR

#### 1. Introduction

Magneto-resistance (MR) sensors have been widely used in many applications, since they are simple two-terminal resistance devices and are easily micro-fabricated by low cost lithography techniques. Major applications of the MR sensors are hard-disk-drive (HDD) heads<sup>1)-3)</sup>, linearrotary position encoders4),5), and recently they are reported to be applied to bio-magnetic sensors<sup>6),7)</sup> and automotive current monitors8) by improving their sensitivity and linearity, respectively. In order to improve the sensitivity of the MR sensors, tunnel magneto-resistance (TMR) sensors magnetoresistance (MR) ratio over 100% are typically utilized. For example, sub-pT field9 detection using TMR sensor was reported for the applications to magnetocardiography (MCG)10) and magneto-encephalography  $(MEG)^{11)}$  at room temperature. However, the TMR sensors consist of magnetic tunnel junctions (MTJ) and basically have a large resistance, resulting in the larger shot noise than that of a giant magnetoresistance (GMR) sensors 12). The GMR sensors have a small resistance due to their metallic nature and high signal-to-noise (S/N) ratio at low frequencies. Moreover, the fabrication process of GMR sensors is simple compared to TMR sensors, which is an apparent advantage in terms of industrial applications. Recently, several studies on GMR sensors report to detect magnetic field as small as pT. For example, an antiphase modulation bridge detection technique utilizing GMR elements with symmetric response was reported in Ref. 13. This technique reduces 1/f noise significantly which mainly dominates the noise spectrum of GMR elements at

Corresponding author: T. Kato (e-mail: kato.takeshi.i6@f.mail.nagoya-u.ac.jp).

frequency f < 100 kHz. We have also studied the antiphase modulation GMR sensors and reported that the non-linearity due to the hysteresis in the free layers and the temperature drift are significantly improved<sup>14)</sup> by introducing a closed-loop current-field feedback technique<sup>15)</sup>. However, the sensor output was insufficient to detect pT-level field.

One of the ways to improve the sensor output is to use magnetic flux concentrators (MFC) to amplify the magnetic field applied to the GMR elements<sup>16)</sup>. For instance, Kikitsu et al. reported the detectivity of 13 pT/Hz<sup>1/2</sup> at 100 Hz in antiphase modulation GMR sensors by using MFCs<sup>17)</sup>. Moreover, Tatsuoka et al. utilized the GMR sensors with MFCs as well as the compensating coils wounded around the MFCs, and high detectivity and wide dynamic range were reported<sup>18)</sup>. Another way is to detect the field along the easy axis of GMR sensors since the magnetic susceptibility along the easy axis is much higher than that along the hard axis. Conventional MR sensors detect the fields along the hard axis due to the small hysteresis. We have previously reported domain wall displacing (DWD) GMR sensors to detect the fields along the easy axis, which results in several-times increase of the sensor output and enables to detect nT level magnetic fields<sup>19)-21)</sup>. Liao et al. and Huang et al. also reported that DWD modulation effectively reduces the hysteresis and increases the sensitivity compared to no modulation<sup>22), 23)</sup>. However, because DWD involves the motion of the domain walls, the sensor output still has small hysteresis and contains Barkhausen noise.

In this study, we introduced the closed-loop current-field feedback technique to DWD modulation GMR sensors to solve these issues. Here, we discuss the basic operation and performance of the closed-loop DWD modulation GMR sensor, and report the detectivity of the present closed-loop DWD modulation GMR sensor. MFC

is expected to be applied to the present sensor for further improvement of the detectivity which will be studied in future work.

#### 2. Operating principle

#### 2.1 Domain wall modulation

Figures 1 and 2 show the circuit diagram of DWD GMR sensor and the schematic of a GMR sensor with an Al wire to apply modulation and feedback fields, respectively. As shown in Fig. 1, a GMR element was connected to the bridge circuit and the modulation field  $H_{\text{mod}}$  was applied along the easy axis by flowing the current through the Al wire placed upon the GMR element (see Fig. 2). Here we assume the stripe domains in the free layers as shown in the illustration of Fig. 3 due to the energy balance between induced anisotropy of the free layer and the shape anisotropy of the GMR wire. The DWD modulation field  $H_{\text{mod}}$  at the frequency  $f_{\text{mod}}$  of 100 kHz modulates the position of the domain walls as in Fig. 3. f<sub>mod</sub> is much higher than the frequency of detecting fields  $H_{\text{ext}}$ . Since the domain walls are oscillated by  $H_{\text{mod}}$ , the center positions of the domain wall shift sensitively to  $H_{\text{ext}}$  which is smaller than the wall coercivity. This technique is considered to be effective to reduce the wellknown Barkhausen effect<sup>20)</sup> and enhance sensitivities<sup>22), 23)</sup>.

The bridge circuit output is proportional to the ratio of the parallel and antiparallel domain areas to the

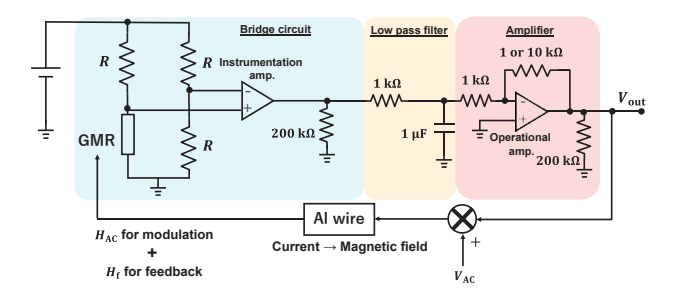


**Fig. 1** Circuit diagram of the proposed GMR sensor using domain wall displacement (DWD) modulation with closed-loop current-field feedback.

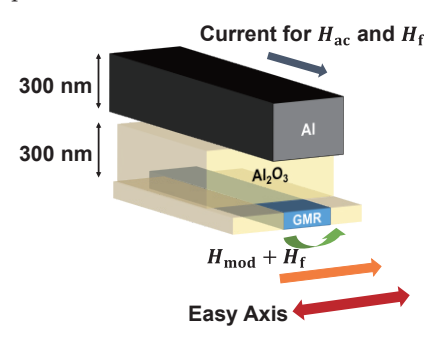


**Fig. 2** Schematic of GMR sensor device with GMR element and Al wire. Easy axis of GMR element is parallel to wire width direction. Modulation field  $H_{\rm mod}$  and feedback field  $H_{\rm f}$  are produced by current flowing through Al wire.

reference layer of the GMR element. Both  $H_{\rm mod}$  and  $H_{\rm ext}$  components appear in the instrumentation amplifier (IA) output, since both fields affect the domain area, and  $H_{\rm mod}$  component was filtered by the low pass filter (LPF).

#### 2.2 Current field feedback

The output  $V_{\text{out}}$  in Fig. 1 is used to flow the current in Al wire shown in Fig. 2 to produce the feedback field  $H_{\text{f}}$  which cancels  $H_{\text{ext}}$ . Therefore, the relation between  $V_{\text{out}}$  and  $H_{\text{ext}}$  is expressed as following equation:

$$V_{\text{out}} = \frac{1}{\frac{1}{K_{\text{H}} \rightarrow \text{V} \cdot G_{\text{IA}} \cdot G_{\text{OA}}} + F} H_{\text{ext}}, \tag{1}$$

where  $K_{\rm H \to V}$  is the conversion constant from field to voltage, and  $G_{\rm IA}$  and  $G_{\rm OA}$  are the gains of IA and the following operational amplifier (OA) (see Fig. 1). F stands for the feedback constant determined by the width of the Al wire and the resistance connected in series to

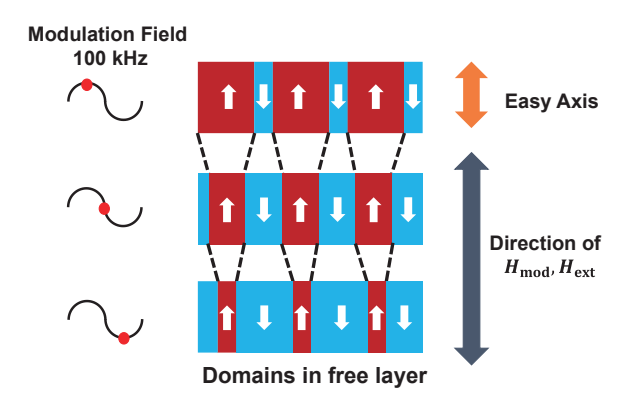


**Fig. 3** Illustration of domain wall displacement (DWD) modulation. Domain walls in free layer oscillate due to modulation field  $H_{\text{mod}}$  at frequency  $f_{\text{mod}}$  of 100 kHz.  $H_{\text{mod}}$  and detected field  $H_{\text{ext}}$  are applied along easy axis of free layer.

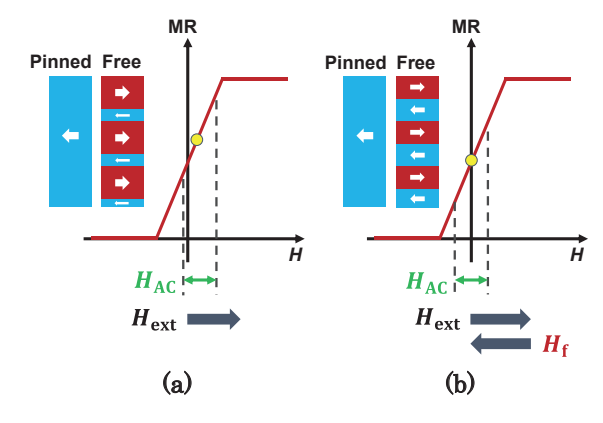


**Fig. 4** Illustrations of the operation point under (a) openmode and (b) closed-loop mode of DWD GMR element. Insets show the time averaged domain structure of the free and the pinned layers, where red and blue are domains parallel and antiparallel to the reference layer, respectively.

the Al wire. If  $1/(K_{\mathrm{H} \to \mathrm{V}} \cdot G_{\mathrm{IA}} \cdot G_{OA}) \ll F$ ,  $V_{\mathrm{out}}$  can be determined only by F. In other words, the feedback current can be adjusted by tuning the loop gain which is the product of  $G_{\mathrm{IA}}$  and  $G_{\mathrm{OA}}$ .

Figure 4 shows the schematic of the current-field feedback operation of the DWD GMR sensor. When no  $H_{\rm ext}$  is applied, the time average of the areal ratio of domains between antiparallel (red) and parallel (blue) to the pinned layer is assumed to be 1:1. If  $H_{\rm ext}$  is applied to the GMR element without the feedback circuit, which is referred to as "open mode", the center positions of the domain walls shift due to  $H_{\rm ext}$  (see Fig. 4 (a)). On the other hand, closed-loop current-field  $H_{\rm f}$  cancels  $H_{\rm ext}$  in the closed-loop mode (see Fig. 4 (b)), which suppresses the shift of domain walls under  $H_{\rm ext}$ .

#### 3. Experimental setup

#### 3.1 GMR stacks

GMR stacks were fabricated by 8-cathodes RF magnetron sputtering system. The stacks were substrate / Ta (5) / Nis<sub>0</sub>Fe<sub>20</sub> or  $(Co_{90}Fe_{10})_{92}B_8$  (10) / Cu (4) /  $Co_{90}Fe_{10}$  (3) / Mn<sub>80</sub>Ir<sub>20</sub> (8) / Ta (3) and substrate / Ta (5) /  $(Co_{90}Fe_{10})_{92}B_8$  (10) / Cu (2.2) /  $Co_{90}Fe_{10}$  (3) / Mn<sub>80</sub>Ir<sub>20</sub> (8) / Ta (3), where the numbers in parentheses indicate the thickness in nanometer. The latter is the same stack as studied in Ref. 19-21. The substrate was Si substrate with the 500 nm-thick thermally oxidized layer. During the deposition, the external field of 27mT was applied to induce the exchange bias in the reference layer and the uniaxial anisotropy in the free layer.

#### 3.2 Microfabrication

GMR stacks were microfabricated as shown in Fig. 2. First, the GMR films were structured with the size of 30  $\mu m \times 300~\mu m$  by maskless lithography followed by  $Ar^+$  ion milling.  $Ar^+$  ions were produced by the Kaufman-type  $Ar^+$  ion source and were incident on the sample with an angle of  $90^\circ$  from the surface. The incident ion energy was set at 700 eV. Then,  $Al_2O_3$  insulator with the thickness of 300 nm was deposited. Finally, Al wires with the size of  $60~\mu m \times 360~\mu m$  and the thickness of 300 nm were fabricated above the GMR elements using a lift-off technique.

After the microfabrication, the GMR sensors with  $Ni_{80}Fe_{20}$  free layer were annealed in vacuum at  $270^{\circ}C$  for 10 minutes under the field of 230 mT. The field was applied along the short axis of the GMR elements. The annealing temperature was set at  $270^{\circ}C$ , since the blocking temperature of the IrMn is  $270^{\circ}C$ , and Mn atoms start to diffuse into the adjacent layers above this temperature<sup>24), 25)</sup>. The GMR sensors with  $(Co_{90}Fe_{10})_{92}B_8$  free layer were not annealed, since the annealing would crystallize the free layer, which increases the coercivity.

#### 3.3 Measurement setup

The GMR sensor devices were connected in the bridge circuit as shown in Fig. 1 and placed into the measurement system with a pair of coils. The pair of coils

Table 1 Parameters of measurement circuit.

Parameter	Value
Voltage of bridge circuit: $V_{\rm B}$	3 V
Frequency of $H_{\text{mod}}$ : $f_{\text{mod}}$	$100~\mathrm{kHz}$
Gain of IA: $G_{IA}$	456
Cut off frequency of LPF	$159.2~\mathrm{Hz}$
Gain of OA: $G_{OA}$	1 (Open-1, Closed-1) 10 (Closed-10)

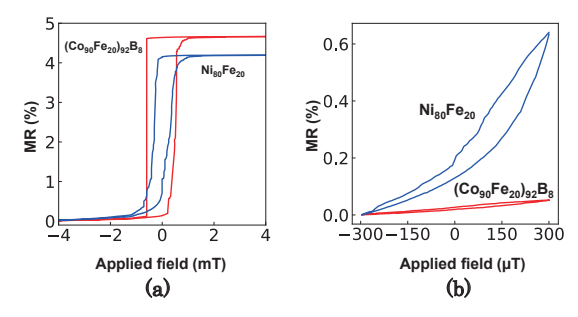


**Fig. 5** MR loops of GMR elements with Ni<sub>80</sub>Fe<sub>20</sub> (blue) and  $(Co_{90}Fe_{10})_{92}B_8$  (red) free layers with field sweep ranges of (a) -4 mT  $\le H_{\rm ext} \le 4$  mT and (b) -300  $\mu$ T  $\le H_{\rm ext} \le 300$   $\mu$ T.

produces  $H_{\rm ext}$ .  $H_{\rm ext}$  was used as an input of the DWD GMR sensor as well as to measure the MR loops of the GMR elements. Parameters of the circuit are indicated in Table 1. Hereafter, we call three types of the circuit modes as "Open-1", "Closed-1" and "Closed-10". "Open-1" indicates that the sensor is operated under open mode and the OA gain is  $G_{OA}=1$ , corresponding to the conventional DWD GMR sensors 19)-21). "Closed-1" and "Closed-10" indicate that the sensor is operated under closed-loop current-field feedback with the OA gains of  $G_{OA}=1$  and  $G_{OA}=10$ , respectively.

#### 4. Results and Discussions

#### 4.1 MR properties

Figure 5 shows the MR loops of GMR elements with Ni $_{80}$ Fe $_{20}$  and (Co $_{90}$ Fe $_{10}$ ) $_{92}B_8$  free layers with the field sweep ranges of (a) |  $H_{\rm ext}$ |  $\leq 4$  mT and (b) |  $H_{\rm ext}$ |  $\leq 300$   $\mu$ T. From Fig. 5 (a), MR ratio and coercivity of the GMR with Ni $_{80}$ Fe $_{20}$  are smaller than those with (Co $_{90}$ Fe $_{10}$ ) $_{92}B_8$ . The smaller MR ratio in GMR with Ni $_{80}$ Fe $_{20}$  is owing to the thicker spacer layer between the free and reference layers. On the other hand, for smaller sweep field of |  $H_{\rm ext}$ |  $\leq 300$   $\mu$ T shown in Fig.5 (b), the GMR with Ni $_{80}$ Fe $_{20}$  free layer exhibited large MR change over 0.6 % while the one with (Co $_{90}$ Fe $_{10}$ ) $_{92}B_8$  was only 0.05%. This is due to the large coercivity of (Co $_{90}$ Fe $_{10}$ ) $_{92}B_8$ , and thus, Ni $_{80}$ Fe $_{20}$  free layer is preferable to obtain higher output within the small field range.

#### 4.2 Domain wall modulation

Since a sinusoidal  $H_{\text{mod}}$  with the frequency of 100 kHz modulates the domain walls in the free layer, the modulated signal can be observed in the output of IA.

Figure 6 shows the IA output when  $H_{\rm mod}$  of  $94 \mu T_{\rm rms}$  at the frequency of 100 kHz was applied, where no  $H_{\rm ext}$  was applied. it was slightly distorted due to the hysteresis of the MR curves. The amplitude of the waveform was not varied drastically when the external field  $H_{\rm ext}$  in the range of  $\pm 100 \mu T$  was applied.

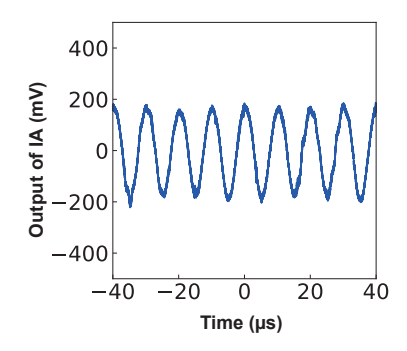
#### 4.2 $H_{\text{mod}}$ Dependence of sensitivity and non-linearity

Figure 7 shows  $H_{\rm ext}$ - $V_{\rm out}$  properties of the DWD GMR sensor with Nis<sub>0</sub>Fe<sub>20</sub> free layer under Open-1 mode, where  $H_{\rm mod}$  was (a) 0, (b) 37.6, and (c) 94.0  $\mu T_{\rm rms}$ . Blue solid curves indicate the measured data. The measured data were fitted with Rayleigh loops expressed as follows, since the output properties reflect the minor loop of Nis<sub>0</sub>Fe<sub>20</sub> free layer.

$$V_{\text{out}} = \begin{cases} -aH_{\text{ext}}^2 + bH_{\text{ext}} + c \\ aH_{\text{ext}}^2 + bH_{\text{ext}} - c \end{cases}$$
 (2)

The fitted Rayleigh loops are shown as the red dashed lines in the figure. For the fitting, b was first estimated from two loop ends, then a and c were estimated by the least square fit. In this paper, we define the non-linearity of sensor output as a normalized by the full scale of the sensor output  $V_{\rm full}$ , and the sensitivity of the sensor was defined as the absolute value of b.

Figure 8 show (a) sensitivity |b| and (b) non-linearity  $a/V_{\text{full}}$  of DWD GMR sensor with Ni<sub>80</sub>Fe<sub>20</sub> free layer as a function of  $H_{\text{mod}}$ . Both sensitivity and non-linearity



**Fig. 6** IA output waveform of DWD GMR sensor with Ni<sub>80</sub>Fe<sub>20</sub> free layer when  $H_{\rm mod}$  of 94 $\mu$ Trms at the frequency of 100 kHz and no external field  $H_{\rm ext}$  were applied.

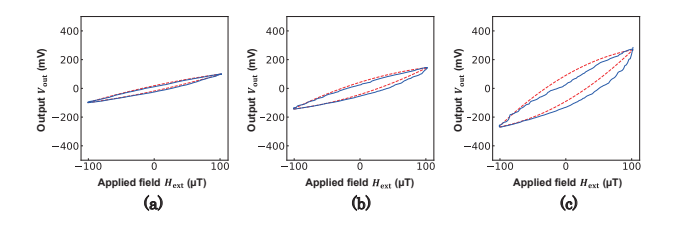


**Fig. 7**  $H_{\rm ext}$ - $V_{\rm out}$  properties of DWD GMR sensor with Nis<sub>0</sub>Fe<sub>20</sub> free layer under Open-1 mode applying (a)  $H_{mod}=0~\mu T_{\rm rms}$ , (b)  $H_{mod}=37.6~\mu T_{\rm rms}$ , (c)  $H_{mod}=94.0~\mu T_{\rm rms}$ . Solid blue curves indicate measured data, and red dashed curves are fitted data with Rayleigh loops expressed in Eq. (2).

increased with increasing  $H_{\rm mod}$  as discussed in Fig. 7. Dependence of sensitivity and non-linearity for Closed-1 and Closed-10 modes will be discussed later.

In order to discuss the reason of the increases of sensitivity and non-linearity with  $H_{\text{mod}}$ , domain structures of the free layer were observed with the Kerr microscope. For the measurement, we deposited the samples with a stack of substrate / NiFe (10) / SiN (40) and microfabricated in the same size as GMR elements of the sensor devices. Before the observation, the sample was magnetically saturated with a field of 6 Oe. Figure 9 shows the Kerr microscope images of Ni<sub>80</sub>Fe<sub>20</sub> rectangle at fields of (a) 0 Oe and (b) 1 Oe. At 0 Oe, the flux-closure domains were observed. The area of domains parallel to the external field was confirmed to increase at 1 Oe as shown in Fig. 9 (b), and flux-closure domain structure is partially collapsed by the large displacement of the domain walls. The domain structure was completely different from the stripe domains of (Co<sub>90</sub>Fe<sub>10</sub>)<sub>92</sub>B<sub>8</sub> thin films reported in Ref. 21 (see Fig. 9 (c)).

From the domain observations, we consider the reason of enhancement in the hysteresis of the output under the large modulation field (see Fig. 7) is due to the variation

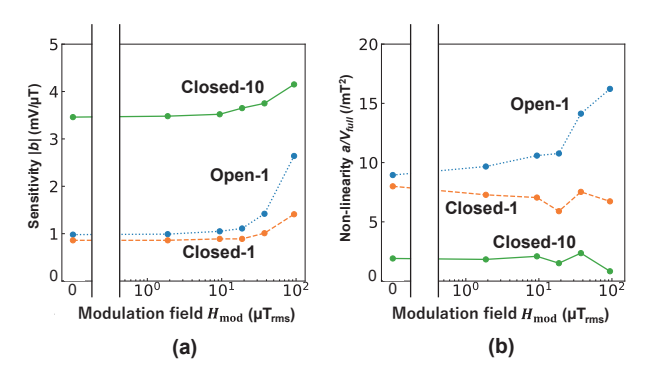


**Fig. 8** (a) Sensitivity and (b) non-linearity of DWD GMR sensor with  $Nis_0Fe_{20}$  free layer as function of  $H_{mod}$ . Blue circles are for Open-1 mode, orange circles are for Closed-1 mode, and green circles are for Closed-10 mode.

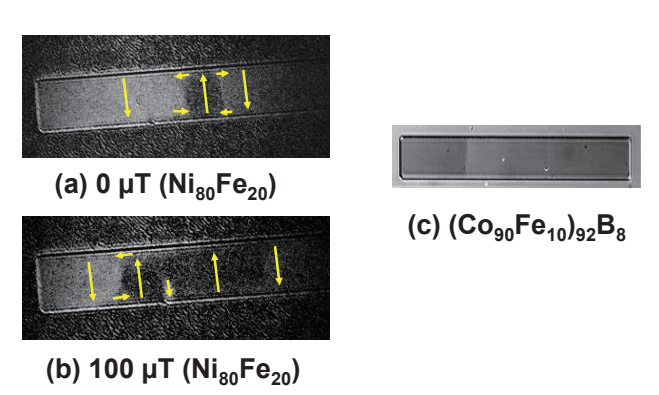


**Fig. 9** Kerr microscope images of  $Ni_{80}Fe_{20}$  element under external fields of (a) 0  $\mu T$  and (b) 100  $\mu T$ . (c) Domain structure of CoFeB is also shown as reference<sup>21)</sup>.

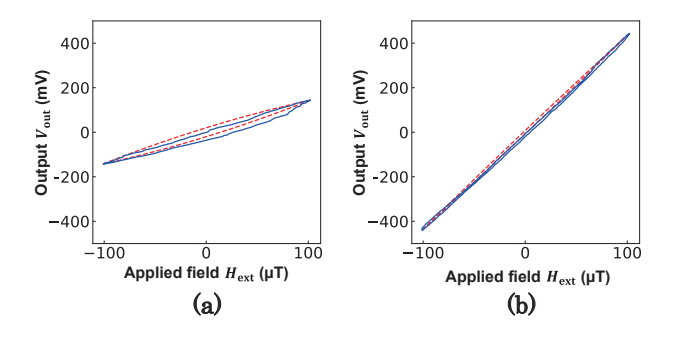


**Fig. 10**  $H_{\rm ext}$ - $V_{\rm out}$  properties of DWD GMR sensor with Ni<sub>80</sub>Fe<sub>20</sub> free layer under (a) Closed-1 and (b) Closed-10 modes. Solid blue curves indicate measured data, and dashed red curves are fitted with Rayleigh loops in Eq. (2).

of the domain structures under the fields. The increase of the sensitivity with  $H_{\rm mod}$  is considered to be due to the reduction of wall coercivity under  $H_{\rm mod}$  as discussed in the previous paper<sup>21)</sup>.

#### 4.3 Effect of feedback operation

Figure 10 shows  $H_{\rm ext}$ -  $V_{\rm out}$  profiles of DWD GMR sensor under (a) Closed-1 and (b) Closed-10 modes.  $H_{\rm mod}$  was fixed at 94.0  $\mu T_{\rm rms}$ . The normalized a was 6.73 mT<sup>-2</sup> for Closed-1, and 0.83 mT<sup>-2</sup> in Closed-10 mode. From these results, the non-linearity was confirmed to be drastically improved by applying a current-field feedback technique as well as the increase of gain  $G_{\rm OA}$ . Compared to the Open-1 mode as shown in Fig. 6 (c), 95% decrease of the non-linearity was confirmed in Closed-10 mode.

#### 4.4 Summary of sensitivity and non-linearity

Figures 8 (a) and (b) summarize the sensitivity and the non-linearity as a function of  $H_{\rm mod}$  under three operation modes, Open-1, Closed-1, and Closed-10. As shown in Fig. 8 (a), sensitivity increased with increasing  $H_{\rm mod}$  because of the reduction of wall coercivity by  $H_{\rm mod}$ . Moreover, the sensitivity for Closed-10 mode was much larger than that for Closed-1 mode. This is due to the increase of  $K_{\rm H\rightarrow V}\cdot G_{\rm IA}\cdot G_{OA}$  in equation (1).

As shown in Fig. 8 (b), non-linearity decreased in order of Open-1, Closed-1, Closed-10 at any  $H_{\rm mod}$ . Therefore, we can conclude that closed-loop feedback operation is effective to improve the linearity of the DWD GMR sensors.

In order to discuss the improvement of linearity, the effective field applied to the GMR elements were estimated in each mode. Effective input field  $H_{\rm eff}$  is expressed as follows:

$$H_{\text{eff}} = H_{ext} - FV_{\text{out}} = \frac{1}{1 + K_{\text{H} \to \text{V}} \cdot G_{\text{IA}} \cdot G_{OA} \cdot F} H_{\text{ext}}$$
 (3)  
=  $\eta H_{\text{ext}}$ 

Here,  $K_{H\to V}$  were calculated from |b| for Open-1 mode,

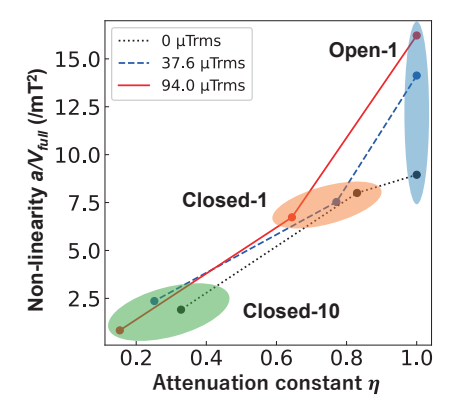


**Fig. 11** Relations of derived  $\eta$  and non-linearity (normalized a). Red circles are for  $H_{mod} = 94.0~\mu T_{rms}$ , blue circles are for  $H_{mod} = 37.6~\mu T_{rms}$ , and black circles are for  $H_{mod} = 0$ . Circuit modes are also indicated in figure.

and the relation between  $\eta$  and the normalized a were evaluated for every  $H_{\rm mod}$ . Note that  $\eta$  means the attenuation constant of the field applied to the GMR elements. The smaller  $\eta$  means the larger  $H_{\rm f}$  to cancel  $H_{\rm ext}$ . Figure 11 shows  $\eta$  dependence of the normalized aof DWD GMR sensors under different operation modes. Open-1 mode has  $\eta$  of 1 independent of  $H_{\text{mod}}$ , since F =0 in Eq. (3). According to the results, the normalized a decreased with decreasing  $\eta$ . The reduction of  $\eta$  will impedes the displacement of the average positions of the domain walls under DWD modulation, which is considered to be effective to reduce non-linearity of the sensor output. In Closed-10 mode, the displacement of the average position of the domain wall is negligibly small in the range of the total applied field  $\pm 100 \, \mu T$ . resulting in the significant improvement of output linearity.

#### 4.5 Noise spectrum

Noise spectrum of  $V_{\rm out}$  of DWD GMR sensor with NisoFe<sub>20</sub> free layer under Closed-10 mode was measured.  $H_{\rm mod}$  was 94.0  $\mu T_{\rm rms}$ . The whole sensor circuit was placed inside the NiFe magnetic shield box (Ohtama) with a shielding factor of 66 dB, and the terminal of  $V_{\rm out}$  was connected to the high pass filter with cut-off frequency of 0.1 Hz (NF Dual Programmable Filter 3624). The noise spectrum was measured by the FFT analyzer (ONOSOKKI FFT Analyzer CF-9200).

Figure 12 shows the FFT spectrum of  $V_{\rm out}$ , where the vertical axis was converted to the input referred magnetic field. From the spectrum, the noise floor at 10 Hz was estimated to be 300 pT/Hz<sup>1/2</sup> as shown in the red line in the figure. Further reduction of the noise floor is expected by applying MFC which will be studied in future work.

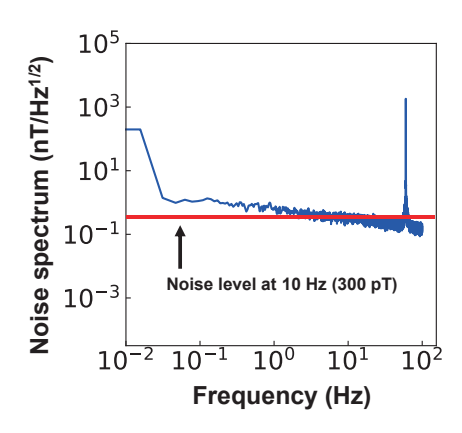


**Fig. 12** FFT spectrum of output of DWD GMR sensor under closed-loop operation with OA gain  $G_{OA}$  of 10.  $H_{mod}$  of 94  $\mu T_{rms}$  was applied during measurement, and no external field  $H_{ext}$  was applied.

#### 5. Conclusion

In this paper, the closed-loop current-field feedback operation was implemented to the DWD GMR sensors. Ni<sub>80</sub>Fe<sub>20</sub> were used for the free layer since the uniaxial anisotropy is smaller than that of (Co<sub>90</sub>Fe<sub>10</sub>)<sub>92</sub>B<sub>8</sub> used in the previous study, resulting in larger wall displacement in smaller applied field. By applying  $H_{mod}$  to DWD GMR sensor under open mode operation, the sensitivity was increased roughly twice compared to GMR sensor without  $H_{\text{mod}}$ . Hysteresis (non-linearity) of the output also increased with increasing  $H_{\text{mod}}$  due to the displacement of the average positions of the domain walls. However, the large hysteresis of DWD GMR sensor with Ni<sub>80</sub>Fe<sub>20</sub> free layer under open mode operation significantly reduced by applying closed-loop currentfield feedback operation. The feedback operation with large loop gain effectively impedes the displacement of the average positions of the domain walls, resulting in the reduction of non-linearity of  $V_{\rm out}$ . Finally, the noise floor of 300 pT/Hz1/2 was obtained for DWD GMR sensor under the closed-loop mode. Further increase of the sensitivity is expected by applying MFCs, and from these results, the proposed sensor was confirmed to be one of the potential candidates of high sensitivity GMR sensors.

Acknowledgments We would like to thank Prof. T. Uchiyama, Nagoya University for helping to measure the noise spectrum of the sensor output. This work is supported in part by JSPS KAKENHI Grant Number 20H02182. This work was also supported in part by the Project of Creation of Life Innovation Materials for Interdisciplinary and International Researcher Development of the Ministry of Education, Culture, Sports, Science and Technology (MEXT), Japan.

A part of this work was performed under the Research Program of "Dynamic Alliance for Open Innovation Bridging Human, Environment and Materials" in Network Joint Research Center for Materials and Devices. A part of this work was conducted at the Nextgeneration biomaterials Hub, Nagoya University, supported by Advanced Research Infrastructure for Materials and Nanotechnology in Japan of MEXT, Japan.

#### References

- R. Rottmayer and J.-G. Zhu: *IEEE Trans. Magn.*, 31, 2597 (1995).
- T. Miyazaki and N. Tezuka: J. Magn. Magn. Mater., 139, 231 (1995).
- 3) S. Mao: IEEE Trans. Magn., 42, 97 (2006)
- H. A. M. van den Berg et al.: J. Magn. Magn. Mater., 165, 524 (1997)
- C. Giebeler, D. J. Adelerhof, A. E. T. Kuiper, J. B. A. van Zon,
   D. Oelgeschläger, and G. Schulz: Sens. Actuators A Phys., 91, 16 (2001).
- 6) G. Li et al.: J. Appl. Phys., 93, 7557 (2003)
- M. Pannetier-Lecoeur, H. Polovy, N. Sergeeva-Chollet, G. Cannies, C. Fermon, and L. Parkkonen: *J. Phys. Conf. Ser.*, 303, 012054 (2011).
- 8) X. Liu, C. Zheng, C. Liu, and P. W. T. Pong: *IEEE Sens. J.*, **18**, 3098 (2018).
- 9) M. Oogane et al.: Appl. Phys. Express, 14, 123002 (2021).
- 10) K. Fujiwara et al.: Appl. Phys. Express, 11, 023001 (2018).
- 11) A. Kanno et al.: Sci. Rep., 12, 6106 (2022).
- 12) H. Weitensfelder, H. Brueckl, A. Satz and K. Pruegl: *Phys. Rev. Applied*, **10**, 054056 (2018).
- 13) S. Shirotori et.al.: IEEE Trans. Magn., 57, 4000305 (2021).
- 14) K. Komuro, D. Oshima and T. Kato: *IEEE Trans. Magn.*, **59**, 4000405 (2023).
- 15) G. A. Wang, S. Arai, T. Kato, and S. Iwata: J. Phys. D Appl. Phys., 44, 235003 (2011).
- N. Smith, F. Jeffers, J. Freeman: J. Appl. Phys., 15, 5082 (1991).
- 17) A. Kikitsu et. al.: Jpn. J. Appl. Phys. 62, SB1007 (2023).
- 18) T. Tatsuoka et. al., TechRxiv. Preprint (2023) https://doi.org/10.36227/techrxiv.22850834.v2.
- 19) G. A. Wang, S. Nakashima, S. Arai, T. Kato, and S. Iwata: J. Appl. Phys., 107, 09E709 (2010).
- 20) G. A. Wang, Y. Masuda, T. Kato, and S. Iwata: J. Phys. D Appl. Phys., 43, 455001 (2010).
- 21) G. A. Wang, Y. Masuda, T. Kato, and S. Iwata: J. Appl. Phys., 109, 07E523 (2011).
- 22) S.-H. Liao et. al.: IEEE Trans. Magn., 57, 4000204 (2021).
- 23) H. -S. Huang et. al.: IEEE Trans. Magn., 58, 4001004 (2022).
- 24) L. Wang et. al., IEEE Sens. J., 21, 27393 (2021).
- 25) H. Li, P. P. Freitas, Z. Wang, J. B. Sousa, P. Gogol, and J. Chapman: J. Appl. Phys., 89, 6904 (2001).

Received Oct. 26, 2023; Accepted Dec. 28, 2023

#### **Editorial Committee Members** • Paper Committee Members

T. Taniyama and S. Okamoto (Chairperson), D. Oyama, M. Ohtake, T. Nozaki, and H. Kikuchi (Secretary)

H. Aoki	M. Goto	T. Goto	S. Haku	T. Hasegawa	R. Hashimoto
M. Iwai	T. Kawaguchi	T. Kawai	K. Kobayashi	T. Kojima	H. Kura
S. Muroga	T. Narita	M. Sakakibara	Y. Sato	E. Shikoh	Y. Shiota
T. Shirokura	S. Sugahara	K. Suzuki	Y. Takamura	T. Takura	S. Tamaru
M. Toko	S. Yakata	S. Yamada	T. Yamazaki	A. Yao	T. Yoshida
37 37 1 1 1					

Y. Yoshida

N. Adachi	S. Ajia	F. Akagi	K. Bessho	A. Chikamatsu	M. Doi
T. Doi	T. Fukushima	Y. Hane	K. Hioki	S. Honda	S. Iihama
S. Isogami	N. Kikuchi	A. Kuwahata	T. Maki	K. Masuda	M. Naoe
K. Nawa	D. Oshima	S. Ota	R. Sakagami	S. Sakurai	Y. Sasaki
M. Sato	S. Seino	M. Sekino	T. Suetsuna	I. Tagawa	K. Tajima
M. Takezawa	T. Yamada	T. Yamazaki	S. Yoshimura		

#### Notice for Photocopying

The Magnetics Society of Japan authorized Japan Academic Association For Copyright Clearance (JAC) to license our reproduction rights, reuse rights and AI ML rights of copyrighted works.

If you wish to obtain permissions of these rights in the countries or regions outside Japan, please refer to the homepage of JAC (http://www.jaacc.org/en/) and confirm appropriate organizations to request permission.

However, if CC BY 4.0 license icon is indicated in the paper, the Magnetics Society of Japan allows anyone to reuse the papers published under the Creative Commons Attribution International License (CC BY 4.0).

Link to the Creative Commons license: http://creativecommons.org/licenses/by/4.0/  $\,$ 

Legal codes of CC BY 4.0: http://creativecommons.org/licenses/by/4.0/legalcode

#### 編集委員・論文委員

谷山智康(理事	事) 岡本 聡	(理事) 小山大介	↑ (幹事) 大竹	充 (幹事)	野崎友大 (幹事)	菊池弘昭(特	任幹事)	
青木英恵	岩井守生	川井哲郎	川口昂彦	藏 裕彰	小嶋隆幸	後藤太一	後 藤 穣	小林宏一郎
榊 原 満	佐藤佑樹	塩田陽一	仕幸英治	白倉孝典	菅原 聡	鈴木和也	高村陽太	田倉哲也
田丸慎吾	都 甲 大	成田正敬	白 伶士	橋本良介	長谷川崇	室 賀 翔	八尾惇	家 形 諭
山崎貴大	山田晋也	吉田 敬	吉田征弘					
阿加賽見	赤城文子	安達信泰	飯浜賢志	磯上慎二	大島大輝	大多哲史	菊地伸明	桑波田晃弘
坂上良介	櫻 井 将	佐々木悠太	佐藤光秀	末綱倫浩	清野智史	関野正樹	田河育也	竹澤昌晃
田島克文	近松 彰	土井達也	土井正晶	直江正幸	名和憲嗣	羽根吉紀	日置敬子	福島隆之
別所和宏	本多周大	槙 智仁	増田啓介	山崎 匠	山田豊和	吉村 哲		

#### 複写をされる方へ

当学会では、複写複製、転載複製及びAI利用に係る著作権を一般社団法人学術著作権協会に委託しています。 当該利用をご希望の方は、(社)学術著作権協会(https://www.jaacc.org/)が提供している許諾システムを通じてご申請下さい。

ただし、クリエイティブ・コモンズ [表示 4.0 国際] (CC BY 4.0)の表示が付されている論文を、そのライセンス条件の範囲内で再利用する場合には、本学会からの許諾を必要としません。

クリエイティブ・コモンズ・ライセンス http://creativecommons.org/licenses/by/4.0

リーガルコード http://creativecommons.org/licenses/by/4.0/legalcode.ja

#### Journal of the Magnetics Society of Japan

Vol. 49 No. 6 (通巻第342号) 2025年11月1日発行

Vol. 49 No. 6 Published Nov. 1, 2025

by the Magnetics Society of Japan

Tokyo YWCA building Rm207, 1–8–11 Kanda surugadai, Chiyoda-ku, Tokyo 101–0062 Tel. +81–3–5281–0106 Fax. +81–3–5281–0107

Printed by JPC Co., Ltd.

Sports Plaza building 401, 2–4–3, Shinkamata Ota-ku, Tokyo 144–0054 Advertising agency: Kagaku Gijutsu-sha

発行: (公社)日本磁気学会 101-0062 東京都千代田区神田駿河台 1-8-11 東京YWCA会館 207 号室 製作: ジェイピーシー 144-0054 東京都大田区新蒲田 2-4-3 スポーツプラザビル401 Tel. (03) 6715-7915 広告取扱い: 科学技術社 111-0052 東京都台東区柳橋 2-10-8 武田ビル4F Tel. (03) 5809-1132

| 111-0032 | 未来制日本区物間 2-10-0 | 民田 C / 41 | 161. (03)

Copyright © 2025 by the Magnetics Society of Japan